REACTIVE SCATTERING OF HALOGEN MOLECULES

Contents

ACKNOWLEDGMENTS

I wish to express my sincere thanks to Professor Y. T. Lee whose scientific acumen, irrepressible enthusiasm, and persistent encouragement were instrumental in making these four years scientifically productive and personally rewarding.

Thanks are also due to the many members of Professor Lee's research group with whom I have had the pleasure of being associated. I am especially grateful to Dr. D. J. Auerbach and Dr. M. J. Coggiola with whom I have enjoyed productive and stimulating collaborations.

I am deeply grateful to the late Professor Robert Platzman and his wife Eva whose encouragement and beneficence at the beginning of my graduate career were important in ensuring it successful conclusion.

The considerable efforts of Ms. Ann Weightman in typing the manuscript were obviously essential to its completion and are greatly appreciated.

The financial support of the National Science Foundation through a graduate fellowship is also appreciated.

Finally, I wish to thank my parents whose continuing support has been singularly important in all my endeavors.

This work was done with support from the U.S. Energy Research and Development Administration.

REACTIVE SCATTERING OF HALOGEN MOLECULES

James Joseph Valentini

Materials and Molecular Research Division
Lawrence Berkeley Laboratory

and

Department of Chemistry
University of California
Berkeley, California 94720

November 1976

ABSTRACT

We describe a study of the endoergic, bimolecular reactions of F_2 with I_2, ICl, and IBr in a crossed molecular beam experiment. The trihalogens IIF$_2$, ClIF$_2$, and BrIF$_2$ have been directly observed as the products of these reactions. At high collision energies a second reactive channel producing IF becomes important. Product angular and velocity distributions show that this IF does not result from a four-center exchange reaction. Measured threshold energies for the formation of IIF$_2$, ClIF$_2$, and BrIF$_2$ yield lower bounds to the stabilities of these molecules, with respect to the separated atoms, of 69, 81, and 96 kcal/mole, respectively. Analysis of product center-of-mass angular distributions indicates that a slightly non-linear approach is most effective in bringing about reaction to form the stable triatomic radical.

Also described is a crossed molecular beam study of the Cl + Br_2 → BrCl + Br reaction at collision energies from 6.8 to 17.1 kcal/mole. The results indicate that this reaction has the characteristics of an

exoergic reaction on an attractive potential energy surface with early energy release. Reagent translational energy is very efficiently channeled into product internal energy. At high collision energy the reaction appears to approach the spectator stripping limit.

A reliable, resistance heated graphite nozzle beam source which is capable of producing high intensity supersonic atomic and molecular beams of chlorine, bromine, and iodine, is also described. Using seeded halogen gas mixtures, beams with kinetic energies up to several eV with 10-15% FWHM velocity spread can be easily produced.

Finally, we describe a series of computer programs which can be used to carry out the requisite data analysis for crossed molecular beam reactive scattering experiments. These programs recover the reactive scattering center-of-mass flux distribution from the measured angular and velocity distributions of the products.

I. INTRODUCTION

The utility of the crossed molecular beam method for investigating the dynamics of chemical reactions has become well established in recent years. Recent reviews[1,2] and monographs[3] have discussed in detail the experimental techniques of this method and the large and ever increasing number of reactions which have been studied in this way. Two particularly advantageous features of crossed molecular beam experiments are the detection of the reaction products after a single reactive encounter, and the facility with which the initial translational energy of the reactants can be adjusted.

The first of these allows the measurement of the nascent product energy distribution in the absence of any collisional degradation. Either spectroscopic observation of product internal energy distributions, or velocity analysis of the products to obtain recoil translational energy distributions, coupled with the known thermodynamics of the reactions, endo- or exoergicities, can be exploited to yield detailed information about reaction energy disposal. Just as important, if not more so, is the fact that the detection of products under single collision conditions facilitates the observation of possible transient species, which although not always detectable in bulk kinetic experiments, obviously can be important in elucidating the dynamics and explaining macroscopic rate expressions of reactions.

The second favorable feature of crossed molecular beam experiments, the "tunability" of the initial reactant translational energy, is primarily achieved by the use of "seeded" supersonic nozzle beams.[4]

The use of such nozzle sources, which produce beams with hypothermal or hyperthermal energy with very narrow (10-15% FWHM) velocity distributions, allows detailed investigation of the energy dependence of elastic, inelastic, and reactive collisional processes.

In chapter II we describe the construction of a reliable, resistance heated nozzle beam source which is capable of producing high intensity supersonic atomic and molecular beams of chlorine, bromine, and iodine. The use of a high density graphite nozzle eliminates corrosion and allows operation up to 2100 K. Using seeded halogen gas mixtures, beams with kinetic energies up to several eV with 10-15% FWHM velocity spread can be easily produced.

The use of this beam source to study the $Cl + Br_2 \rightarrow BrCl + Br$ reaction is reported in chapter IV. The results indicate that this reaction has the characteristics of an exoergic reaction on an attractive potential energy surface with early energy release. Reagent translational energy is very efficiently channeled into product internal energy. Although the $Cl - Br_2$ interaction is attractive, the cross section for reaction is much smaller than the hard sphere value. A study of the reaction as a function of collision energy reveals that at relatively high collision energy, 15-20 kcal/mole, the reaction approaches the spectator stripping limit and is nearly a two body process, while at lower collision energy, ~7 kcal/mole, the reaction dynamics are considerably more complicated and definitely three body in character.

Chapter III describes a study of the reactions of F_2 with the halogen containing molecules I_2, ICl, and HI. The trihalogens IIF and ClIF, and the pseudo-trihalogen HIF have been directly observed as the products of these endoergic bimolecular reactions:

$$F_2 + XI \longrightarrow XIF + F.$$

At high collision energies a second reaction channel, producing IF, becomes important:

$$F_2 + XI \longrightarrow X + IF + F.$$

Product angular and velocity distributions show that this IF does not result from a four-center exchange reaction:

$$F_2 + XI \longrightarrow XF + IF.$$

Observed threshold energies for the formation of IIF, ClIF, and HIF yield lower bounds to the stabilities of these molecules, with respect to the separated atoms, of 69, 81, and 96 kcal/mole, respectively. Analysis of the product center-of-mass angular distributions indicates that a slightly non-linear approach is most effective in bringing about reaction to form the stable triatomic radicals. These studies reveal a potentially important mechanism for the $F_2 + I_2 \rightarrow 2IF$ gas phase reaction.

Finally, in chapter V, several computer programs are described which can be used to carry out the requisite data analysis for reactive scattering experiments. These programs facilitate the recovery of the reactive scattering doubly differential cross section in the center-of-mass coordinate system, the quantity of interest, from measured angular and velocity distributions of products.

A. References

1. J. M. Farrar and Y. T. Lee, Chemical Dynamics, in Annual Review of Physical Chemistry (Annual Reviews, Palo Alto, California, 1974), Vol. 25, p. 357.

2. J. L. Kinsey, Molecular Beam Reactions, in Chemical Kinetics, MTP Int. Rev. of Science (Butterworths, London, 1972), Vol. 9, p. 173.

3. M. A. D. Fluendy and K. P. Lawley, Chemical Applications of Molecular Beam Scattering (Chapman and Hall, London, 1973).

4. N. Abauf, J. B. Anderson, R. P. Andres, J. B. Fenn, and D. G. H. Marsden, Science, 155, 997 (1967).

5. This work was done with support from the U.S. Energy Research and Development Administration.

II. AN ATOMIC AND MOLECULAR HALOGEN NOZZLE BEAM SOURCE

A. Introduction

In a molecular beam source a gas, or the vapor of a solid or liquid, flows from a closed chamber or oven through a small orifice into an evacuated experimental chamber. Defining elements such as slits are used to restrict the size and divergence of the beam. One attempts in this way to produce a beam of atoms or molecules which is well defined spatially and in which collisions between particles in the beam are eliminated. By causing two such beams to intersect or cross at some arbitrary angle one can study collisional processes, elastic, inelastic, or reactive scattering, under single collision conditions.

Molecular beam sources can be characterized by a Knudsen number, K_n

$$K_n = \lambda_o/D, \tag{1}$$

where D is the diameter of the source orifice and λ_o is the mean free path of the gas or vapor in the source chamber.

$$\lambda_o = \frac{kT_o}{\sqrt{2}\sigma_{visc} P_o}. \tag{2}$$

P_o and T_o are the source pressure and temperature and σ_{visc} is the gas viscocity cross section. $K_n < 1$ characterizes the molecular effusion source, while for the nozzle source $K_n \ll 1$. In the molecular effusion source the particles do not undergo any collisions in passing through the orifice, while for a nozzle source the particles undergo many collisions in passing through the orifice. This is the basic difference

between the molecular effusion source and the nozzle beam source and is responsible for the radically different properties of the two sources.

The molecular effusion source, shown schematically in Figure 1 is easy to operate and simple to construct. Because the beam particles do not undergo collisions in passing through the orifice, the properties of a beam produced from such a source are easily understood in terms of the properties of the gas in the source chamber and the kinetic theory of gases. However, simplicity of operation and ease of construction are not the most important attributes of a molecular beam source. Of greater importance are the intensity, the angular divergence and the velocity distribution of the beam.

Intensity is obviously important in any experiment which employs a molecular beam source, and is particularly important in crossed beam experiments, where detected intensities of scattered products are extremely small. Crossed beam experiments also require small angular divergences and narrow velocity distributions in the beams. The important features of differential elastic scattering cross sections are velocity dependent.[1] Reactive scattering differential and total cross sections are often strongly energy (hence velocity) dependent, especially for endoergic reactions.[2] Moreover, the laboratory to center-of-mass transformation Jacobian which allows physically significant information to be derived from laboratory data is dependent on the velocities and intersection angle of the crossed beams. Large angular divergences and wide velocity distributions of the beams hence reduce the amount of

information which can be obtained from crossed beam collision experiments.

Judged by the important criteria of intensity, angular divergence and velocity distribution, the molecular effusion source is quite inferior to the nozzle source. For the effusion source the specific intensity, $I(v,\theta)$, easily calculated from gas kinetic theory,[3] is:

$$I(v,\theta) = n_o \cdot A_o \cdot v \cdot f(v) \cdot \cos\theta, \tag{3}$$

where n_o is the gas number density in the source, A_o is the area of the source orifice, and $f(v)$ is the Maxwell-Boltzmann velocity distribution function,

$$f(v) = v^2 \alpha^{-3} \pi^{-3/2} \exp(-v^2/\alpha^2), \tag{4}$$

where $\alpha^2 = 2kT/m$. By integrating over v at $\theta = 0$ the total intensity per steradian in the forward direction, I_f, is obtained:

$$I_f = \int_0^\infty I(v,0)dv = n_o A_o \bar{v}/4\pi, \tag{5}$$

where $\bar{v} = 2\alpha/\pi^{1/2}$ is the average velocity. As pointed out by Pauly and Toennies[4] the maximum forward intensity for a rectangular slit is independent of the slit width if the width is kept equal to the mean free path ($K_n = 1$). This maximum intensity is, within an order of magnitude, the same for all gases, and as shown by Pauly and Toennies, is 5×10^{16} particles/sr-sec. As will be shown later this intensity is two or three orders or magnitude less than that which can be produced by the nozzle source.

The directivity of the molecular effusion source is also quite poor. As can be seen from equation 3 the angular divergence is quite large, the angle, $\theta_{1/2}$, at which the beam intensity has fallen to $I_f/2$

is about one radian. Since the velocity distribution is Maxwellian the molecular effusion source is also poor for studying collisional processes in crossed beams for reasons outlined above. With the addition of a mechanical velocity selector the wide velocity distribution of the molecular effusion source can be used to advantage in the study of the velocity dependence of collisional processes. However, as will become evident later, the nozzle source can be effectively used to provide higher intensities at a wider range of velocities than the molecular effusion source - mechanical velocity selector combination.

The poor directivity of the molecular effusion source can be easily improved by employing a many channel source which has an array of small capillaries bunched closely together. The capillaries have a diameter D, which is much smaller than their length, l. At pressures such that $A_o \sim l$, the directivity, $\theta_{1/2}$, of a single channel is given by $\theta_{1/2} \sim D/l$. However, these pressures correspond to low flow rates, and at higher pressures the many channel array behaves like an effusion source, with a maximum beam intensity the same as that of a molecular effusion source of the same total orifice area.[5]

By employing a nozzle source to produce a supersonic molecular beam the limitations inherent in the molecular effusion source can be avoided, using a nozzle source which is almost as simple to construct and operate as the molecular effusion source. Figure 2 gives a schematic of a typical nozzle source. The beam, which is now a gas jet, is produced by expanding a gas from a region of high pressure (a few hundred torr) in the nozzle through a small orifice (a few thousandths of an inch in

diameter). The skimmer, a hollow truncated cone with an orifice a few hundreths of an inch in diameter, samples the expanded gas jet to produce the beam and deflects away the remaining gas. Because the total gas flow with a nozzle source is greater by one or two orders of magnitude than with a molecular effusion source, a second pumping chamber, the differential pumping chamber, is necessary when operating a nozzle source. As can be seen by comparing Figures 1 and 2, this arrangement makes the skimmer of the nozzle source analogous to the source orifice of the molecular effusion source.

The beam intensity on axis for a nozzle source is given by:[6]

$$I(v,0) = \frac{n_o A_s}{\pi^{3/2}} \left(\frac{v}{\alpha_o}\right)^3 [1 + \frac{\gamma-1}{2} M^2]^{3/2 - [1/(\gamma-1)]}$$

$$\times \exp-\left(\frac{v}{\alpha_o}[1 + \frac{\gamma-1}{2} M^2]^{1/2} - \frac{\gamma^{1/2} M}{\sqrt{2}}\right)^2 , \qquad (6)$$

where n_o, α_o are the gas number density and most probable velocity in the nozzle, A_s is the area of the skimmer orifice, γ is the ratio of specific heats, and M is the mach number, defined as

$$M^2 = (V_{\text{most probable}})^2/c^2, \qquad (7)$$

where c is the local speed of sound in the beam. By integrating equation 6 over v and dividing by equation 5 one obtains[4] an estimate of the intensity gain in the forward direction (relative to the molecular effusion source) which can be achieved with a nozzle source:

$$\frac{(I_f)\ \text{Nozzle}}{(I_f)\ \text{Molecular Effusion}} = \left(\frac{\gamma}{3}\right)^{3/2} M^2 \exp^{3/2} . \qquad (8)$$

Equation 8 was derived assuming $A_o = A_s$, that is that the molecular

effusion source orifice and nozzle source skimmer orifice have the same area and that the effusion source is operated at maximum intensity ($K_n = 1$). Typically M = 10 to 20, hence for a monatomic gas ($\gamma = 5/3$) this ratio is 180 to 740.

This result was derived assuming an ideal nozzle source expansion, neglecting interference between the gas jet and the skimmer and between the gas jet and the background gas. Interference of these types is always present to some degree and so equation 8 gives an estimate of the maximum intensity gain possible, nevertheless intensity gains approximately as large as predicted have been demonstrated in practice. Bier and Hagena[7] producing nozzle beams of nitrogen, argon, and helium observed intensities of 3.6×10^{18}, 1.8×10^{18}, and 4.1×10^{19} particles/sr-sec respectively, intensities 36 to 800 times greater than the maximum molecular effusion intensity (taken as 5×10^{16} particles/sec-sr as shown earlier). Skofronik[8] found similar intensities for nozzle beams of nitrogen, hydrogen, and helium, 4×10^{18} to 3×10^{19} particles/sr-sec, 80 to 600 times more intense than the molecular effusion source. Scoles and Torello,[9] using a liquid helium pumped nozzle source obtained a beam of argon of 4×10^{18} particles/sr-sec, 80 times more intense than a molecular effusion source. Camparque[10] has recently produced nozzle beams of various gases with intensities to 10^{21} particles/sr-sec.

Because of the nature of the expansion of the gas through the nozzle orifice significant reduction in the angular divergence and the width of the beam velocity distribution is effected. This reduction in the angular and velocity spread comes about because the supersonic

expansion is an isentropic process which converts the random thermal energy of the gas in the source into directed mass flow. The flow velocity, v, is hence related to the enthalpy of the gas:

$$1/2mv^2 = \int_T^{T_o} Cp\ dT. \qquad (9)$$

where m is the molecular weight, Cp the heat capacity, and T_o and T are the gas temperatures in the nozzle source and expanded beam respectively. T is typically very small, 2G K or less. This very large reduction in the temperature of the beam particles effects a reduction in the random velocity of the beam.

To a first appr. 'mation the velocity spread of the beam $\Delta v/v$ is just α/v, α being the most probable random velocity of the gas in the beam. α is related to the speed of sound, c, in the beam by:

$$c = \alpha(\gamma/2)^{1/2}. \qquad (10)$$

Hence from equation 10 and equation 7 the velocity spread can be expressed in terms the Mach number, M, by:

$$\frac{\Delta v}{v} \quad \frac{\alpha}{v} = \left(\frac{2}{\gamma}\right)^{1/2} \frac{1}{M}. \qquad (11)$$

Since α represents the most probable velocity transverse to the flow, α/v is also a measure of the beam divergence, $\theta_{1/2}$.

$$\theta_{1/2} \qquad \frac{\alpha}{v} = \left(\frac{2}{\gamma}\right)^{1/2} \frac{1}{M}. \qquad (12)$$

Since M is typically 10 to 20 the width of the velocity distribution and the angular divergence can be quite small.

Hyperthermal energy beams can easily be produced by expanding mixtures of gases from the nozzle source, the so-called "seeded" beam

technique.[11] Beam energies of several eV can be achieved in this way. In this respect the nozzle source is again far superior to the molecular effusion source, for which the mean kinetic energy is limited to about .5 eV. The nozzle source is also superior to charge exchange beam sources which produce high energy beams by charge exchange neutralization of accelerated ions, for which space charge effects limit intensities below about 10 eV. Unfortunately, this lower end of the hyperthermal energy range is the most interesting of all to chemists because it includes the dissociation energy of all chemical bonds and the activation energy of most chemical reactions.

The principle of operation of the seeded nozzle beam is quite simple. If one expands a light gas (H_2, He, Ne) which contains a few per cent heavy molecules or atoms (N_2, Cs, Cl_2) the heavy particles are dragged along at the mean stream velocity, v, which (analogous to equation 9) is given by:

$$1/2\bar{m}v^2 = \int_T^{T_o} \bar{C}p\,dT, \qquad (13)$$

where $\bar{m}$, $\bar{C}p$ are the concentration weighted molecular weight and heat capacity. The heavy molecules thus attain a kinetic energy higher than their original thermal energy by a factor of $m_H/\bar{m}$ m_H/m_L the ratio of the molecular weight of the heavy to light species.

This technique can also obviously be used to produce a decelerated beam by seeding a light species in a large amount of heavy diluent species. Such "anti-seeded" beams are necessary to produce hypothermal energy beams of species such as halogen atoms which can only be produced at high nozzle temperatures.

The seeding technique has been used to produce hyperthermal energy beams of up to 90 eV kinetic energy.[10] Such beams have been used in studies of collisional dissociation,[12,13] the energy dependence of reaction cross sections,[14-16] and rotational energy transfer.[17] However, the seeding technique has been almost exclusively limited to beams of molecular or stable atomic species. Until the development of the source described below and a similar one[18] for producing fluorine atoms, beams of halogen atoms had usually been produced by thermal dissociation in a molecular effusion source[19] or by low pressure electric discharge.[20,21] Electric discharge sources can only be used to produce low energy (less than .04 eV) halogen atom beams, while thermal dissociation sources are limited by the melting point of the containing material to about .3 eV. The other limitations of the molecular effusion source which have been discussed make it unsuitable for experiments we wished to carry out, such as high resolution elastic scattering of halogen atoms, energy dependence of halogen atom reaction cross sections, and the study of endoergic reactions of halogen atoms and molecules.

For these reasons we have constructed a nozzle source which can be used to produced beams of halogen atoms by thermal dissociation. The source employs a graphite nozzle which can be heated to temperatures above 2000 K to produce beams of chlorine, bromine, or iodine molecules or atoms seeded in rare gas diluents. Both hyperthermal and hypothermal energy beams have been produced for crossed beam studies of reactive collisions of chlorine molecules and atoms[22] and elastic scattering of chlorine atoms.[23]

B. Source Construction

The nozzle source shown partially sectioned in Figure 3, is resistively heated by low voltage, high current AC power (up to 7 volts rms and 450 amps). This low voltage, high current power is provided by winding 4/0 welding cable as the secondary around a toroidal primary coil. A rheostat controls the primary voltage (0-117 VAC), which is supplied by a line voltage regulator. Figure 4 is an enlarged and simplified axially sectioned view of the source showing the heating current path.

The outer graphite tube and nozzle are machined from a special high-density graphite.[24] The nozzle orifice (.079 mm) is hand drilled after final machining. The outer graphite tube (2.22 cm O.D., .32 cm wall) is screwed into the copper mounting block and a graphite nut is screwed onto the tube and tightened down against the copper mounting block to hold the outer graphite tube firmly in place. The nozzle itself (1.27 cm O.D., .32 cm wall) is supported at two points. At the front it fits snugly into the conical bore of the outer graphite tube. At the rear it is securely mounted in a two piece copper supporting block which is split along the axis of the nozzle. The two halves of the supporting block are tightened down on the two halves of a cylindrical graphite sleeve in which the nozzle can slide. This arrangement gives stable support to the nozzle while allowing axial movement due to thermal expansion of the nozzle upon heating. The nozzle supporting block is rigidly fixed to the copper mounting block by means of two screws which are electrically insulated from the mounting

block by mica washers and teflon sleeves. The supporting block and mounting block are separated by several thicknesses of mica sheet.

At its end the nozzle is attached to a .32 cm O.D. stainless steel gas feed line by means of an "O"-ring type fitting.[25] A thin copper plate is attached to the rear of this fitting, and two steel springs connecting the plate to the copper supporting block apply a small axial force to the nozzle. This spring loading keeps the nozzle firmly seated in the conical bore of the outer graphite tube, despite thermal expansion and contraction of the nozzle when repeatedly heated and cooled. The gas feed line is wound in a large radius helix to allow for the expansion and contraction of the nozzle.

The source must be extensively cooled due to the large power dissipation in the nozzle. Both the copper mounting block and nozzle supporting block are internally drilled with channels to allow passage of cooling water. The "O"-ring fitting is cooled through a copper block which clamps to the fitting, and which is internally drilled with cooling water channels. This cooling allows the "O"-ring temperature to be maintained at less than 425 K while the nozzle may be more than 2000 K.

The nozzle assembly is precisely mounted on the front plate of the source chamber (Fig. 5, L) so as to be accurately aligned with the skimmer which is also mounted on the front plate. Figure 5 shows the nozzle assembly mounted in the source chamber. The end plate of the source chamber has several feedthroughs for electrical power, cooling water, gas mixture, and thermocouples. The two pairs of copper tubes (.64 cm O.D.) which provide cooling water for the copper mounting

block and nozzle supporting block also carry the heating current for the nozzle. They are attached to external power cables via bus bars. Vacuum feedthroughs are made by drilling out "O"-ring fittings[25] to accomodate .64 cm O.D. copper tubes. These fittings are attached to lucite flanges which electrically insulate the copper tubes from the end plate. Because of the large radiative flux, the front of the source chamber is also cooled. For this purpose, water is passed through a .64 cm O.D. copper tube soldered to the front surface of the source chamber. Monel, stainless steel, and graphite skimmers of .51 to 1.02 mm orifice diameter have been used with the source. Visible deterioration of the metal skimmers occurs after extended use due to the high temperature and corrosive nature of the beam. The graphite skimmers have proved highly resistant to physical deterioration, especially at the skimmer lip. For the data reported here a stainless steel skimmer of .94 mm diameter was used, with a nozzle to skimmer distance of .57 cm.

C. Beam Characterization

Velocity distributions of seeded beams of halogen atoms and molecules produced by expansion from the graphite nozzle have been determined from time-of-flight velocity analysis. For this analysis the beam was gated on and off by a rotating (150 to 300 cps) aluminum disk of 17.78 cm diameter with eight slots of .165 cm width equally spaced around the periphery. The rotating disk was located at the entrace aperture (0.028 cm diameter) of an electron bombardment

ionizer/quadrupole mass spectrometer detector which has been described in detail elsewhere [26]. The flight path from the rotating wheel to the ionizer was 17.3 cm. A computer controlled 256 channel scaler was used to record the signal intensity as a function of flight time. The start pulse for the multichannel scaler was generated by an LED-phototransitor pair which was also gated on and off by the rotating aluminum disk, and which was located 90° around the wheel from the beam path. The channel width is variable, a width of 4 μsec was used for this analysis.

This arrangement gave an instrumental velocity (time) resolution of 7 to 15%, depending on flight time. This instrumental broadening is due to the width of the gating function and the ionizer length. The actual time-of-flight spectra were recovered[27] by deconvoluting the observed distribution, using the known ionizer geometry and geometrically correct gating function. Corrections to the flight times were made for the ion flight time in the detector and the 90° phase difference between the multichannel scaler start pulse and the gating of the beam. The time scale of the scaler was calibrated by recording the time-of-flight distributions of supersonic beams of pure rare gases expanded from the graphite nozzle at a known temperature (300 K), and comparing them with calculated spectra. The time-of-flight distributions were then converted to flux velocity distributions and the peak flux velocities determined. This procedure gave velocities which are accurate to between 1.5% and 7%, the largest uncertainty being that for the fastest beams of chlorine seeded in helium at the highest temperatures, about 1700 K.

Figure 6 shows the variation of the peak flux velocities for chlorine atoms, chlorine molecules, and diluent gas a function of nozzle temperature for various seeded mixtures. The accessible range of particle energies for this source using these seeded mixtures is quite large. For chlorine atoms energies as low as .10 eV and as high as 1.4 eV are possible. For chlorine molecules the energy range is even wider, from .02 to 2.2 eV. By contrast, an effusive graphite source would have an energy range of about .1 eV to .2 eV for chlorine atoms and .03 to .2 eV for molecules.

The light curve drawn for each seeded mixture gives the expected temperature dependence of the peak velocity assuming an ideal seeded beam expansion, i.e., one in which all species attain the same peak velocity. This expected temperature dependence of the peak velocity is only approximate, due to an uncertainty in the nozzle temperature which is discussed later. The curve is scaled at one temperature to the mole fraction weighted average of the diluent gas and chlorine molecule velocities. For $Cl_2|Ar$ the observed and ideal peak velocities are scaled at 300 K, for $Cl_2|Xe$ the scaling was done at 880 K, since the Xe velocity distribution at room temperature was not recorded. For dilute seeded mixtures such as these, the diluent peak velocities should follow very closely the curve even for a non-ideal expansion. Deviation from this behavior is evident in Figure 6 and is probably due to the uncertainty in the gas temperature in the nozzle. Despite non-ideal behavior, the observed velocities of the $Cl_2|Ar$ and $Cl_2|Xe$ mixtures roughly follow the peak velocities expected of an ideal expansion. A slight amount of "slippage" is evident, especially at higher temperatures,

where the particle number density in the beam may be too small to produce sufficient collisions to effect momentum and energy equilibration between seed and diluent species in the expansion. No curve of ideal velocity versus nozzle temperature is shown for the $Cl_2|He$ mixture, as the helium velocities were not measured and scaling of the curve is not possible. However, the slippage in this mixture is considerable. For a .98% Cl_2 in He seeded mixture the peak velocities expected in an ideal expansion are about 38×10^4 cm/sec at 1650 K, while the measured Cl_2 velocity is 24×10^4 cm/sec. Velocity slippage is expected to increase as the seed-diluent mass ratio deviates further from unity.

Since this slippage is due to insufficient seed-diluent collisions in the expansion an increase in nozzle pressure should lead to an increase in the peak velocity of the heavy species and a decrease in slippage. Such behavior has been observed with this nozzle as can be seen in Figure 7. Similar, though less pronounced behavior also has been observed for the $Cl_2|Ar$ and $Cl_2|Xe$ mixtures.

No points corresponding to chlorine atom peak velocities are shown for temperatures below about 1300 K where the $Cl|Cl_2$ ratio is less than 10. Although the chlorine atom velocity distributions were measured for all temperatures, the distributions are complicated by the contribution to the m/e 35 (Cl^+) signal from Cl_2^+ fragmentation in the detector ionizer. Using the measured Cl_2 fragmentation ratio ($Cl_2^+|Cl^+$) corrections to the chlorine atom velocity distribution can be made, but this has not been done. For temperatures above 1300 K

chlorine atoms are 10 to 1000 times more abundant than molecules, hence Cl_2^+ fractionation makes an insignificant contribution to the Cl^+ signal and need not be taken into account.

The narrow velocity distributions characteristic of supersonic nozzle sources are observed with this graphite nozzle. For 1% Cl_2 in Xe and 10% Cl_2 in Ar the Mach numbers measured range from 7 to 9 (12-16% FWHM). For 1% Cl_2|He the chlorine atom Mach numbers are also in this range, as are the high (> 1400 K) temperature chlorine molecule Mach numbers. However, Mach numbers as high as 25 are observed for chlorine molecules at lower temperatures.

The performance of the graphite nozzle as a source of bromine molecules and atoms has also been evaluated. Figure 8 shows the variation of peak velocities as a function of temperature for all species in a 6.3% Br_2 in Ar mixture. This mixture was generated by passing the argon diluent gas through a temperature controlled reservoir containing liquid bromine. The curve showing the temperature dependence of the peak velocity for an ideal expansion is scaled to the mole fraction weighted sum of the argon and bromine molecule peak velocities at 635 K. As for the chlorine seeded mixtures, velocity slippage is evident. Bromine atom and molecule energies of approximately .3 eV to .5 eV can be produced with this nozzle and seed gas mixture. Although velocity distributions for Br_2|Xe and Br_2|He mixtures were not measured, the expected range of bromine molecule (atom) energies available from this source, even allowing for slippage, is .04 eV to ~3.3 eV (.08 eV to -2.0 eV). The Mach numbers observed for bromine

molecules and atoms range from about 7 to 15, comparable to those for the chlorine seeded mixtures.

As can be seen in Figures 9 and 10 total dissociation of bromine molecules and nearly total dissociation of chlorine can be achieved with the graphite nozzle at halogen partial pressures which give intensities large enough to be useful for collision experiments. The atom:molecule ratios for 10.1% Cl_2 in Ar are naturally not as large as those shown for the .98% Cl_2 in He seeded mixture. However, nearly complete dissociation is also seen in the 10% mixture, the Cl:Cl_2 ratio being about 200 at 1600 K.

D. Determination of Nozzle Temperature

Figures 6 through 10 have abscissas giving the nozzle temperature, or more correctly, the temperature of the gas in the nozzle. That these two temperatures are not identical is a consequence of the dynamic nature of the heating of the nozzle and of the gas flow through the nozzle. For a resistively heated nozzle such as this one which must make good electrical, and hence thermal contact with a cooled surface, a large temperature gradient along the nozzle is inevitable. Radiative losses will of course considerably reduce this gradient. Such a gradient perforce makes the nozzle "temperature" ill-defined. Furthermore, since the flow velocity through the nozzle is quite large, about 6 cm/sec for this source, the gas temperature will be a complicated function of the nozzle temperature and temperature gradient.

For Figures 6 through 10 we have used a temperature scale based on the effective temperature of the gas in the nozzle. This temperature scale is determined from analysis of the measured time-of-flight distributions of beams of pure neon produced by expansion from the graphite nozzle at several different values of the heating power. The variation of this gas temperature with heating power is shown in Figure 11. For comparison the temperature of the nozzle was independently determined. These measurements were made by placing the nozzle source in a small vacuum chamber fitted with an observation window on the axis of the beam. The source was then operated under normal conditions with the skimmer removed, and a calibrated optical pyrometer was used to view the nozzle tip. The gas temperatures fall significantly below the tip temperatures determined in this way, especially at high temperatures. This disagreement is not unexpected as the nozzle design makes the tip region one of large resistance (and hence high temperature) due to the mating of the outer graphite tube and nozzle. By varying the gas pressure in the nozzle we have also observed the pressure dependence of the effective gas temperature. At the nozzle tip temperature of 1500 K a 10% change in gas temperature occurs as the pressure is raised from 500 torr to 1300 torr.

E. Beam Intensity

The beam intensity for this nozzle source was not directly measured, however a fairly accurate estimate of the intensity can be obtained

from a measurement of the pressure rise produced by the beam in the scattering chamber (region III of Figure 2). Depending on the pressure in the nozzle a pressure rise of 5×10^{-8} to 10×10^{-8} torr is observed in the scattering chamber, which is pumped by a 5000 ℓ/sec oil diffusion pump. The beam intensity is then:

$$5 \times 10^{-8} \text{ torr} \times 5000 \text{ ℓ/sec}$$

$$= 2.5 \times 10^{-4} \text{ torr - ℓ/sec}$$

using the lower estimate. At 300 K one torr - lit corresponds to approximately 3.5×10^{19} particles, hence the beam intensity is approximately 1×10^{16} particles/sec. This beams subtends an angle of about 10^{-3} steradian so the intensity is 1×10^{19} particles/sec-sr. This gives a chlorine atom intensity of about 1×10^{17} particles/sec-sr assuming a 1% Cl_2 mixture and assuming the gas in the source and the beam have the same composition. The total gas flow for this source is approximately 2×10^{-1} torr - lit/sec or 7×10^{18} particles/sec. The beam intensity is comparable to those produced by other seeded nozzle sources.[11,28]

By comparison, a molecular effusion source - mechanical velocity selector combination would give a much lower intensity. In our nozzle source arrangement the collision region subtends a solid angle of 10^{-3} steradians at the skimmer which is approximately 3 cm from the collision region. Hence the flux of Cl atoms into the collision region for a 1% seeded mixture would be 1×10^{17} particles/sec-sr $\times 10^{-3}$ sr = 1×10^{14} particles/sec. A molecular effusion source with an intensity of 5×10^{16} particles/sec-sr would have to be located at least 10 cm

from the collision region to allow for the length of the mechanical velocity selector. Hence at the effusion source orifice the collision region would subtend a solid angle of 10^{-3} sr x $(\frac{3 \text{ cm}}{10 \text{ cm}})^2$ 10^{-4} sr, yielding a flux of 5 x 10^{12} particles/sec into the collision region before velocity selection. A very efficient velocity selector[29] with a resolution of 15% (to give the same velocity distribution as our nozzle source) would have a transmission of about 5 x 10^{-2}. Hence the velocity selected flux into the collision region would be 5 x 10^{12} particles/sec x 5 x 10^{-2} = 2.5 x 10^{11} particles/sec. This is about 400 times less than the intensity of the nozzle beam described here.

F. Discussion

The graphite nozzle was not tested using seeded iodine beams. To produce an adequate vapor pressure molecular iodine must be heated to about 350 K. In order to prevent subsequent condensation of the iodine vapor the gas inlet line to the nozzle must also be heated. No provision for such heating was made in the initial construction of the source, designed primarily as a chlorine source. With this simple addition however, hyperthermal beams of both atomic and molecular iodine could be easily produced. Since the bond dissociation energy of molecular iodine is only 60% of that of chlorine, total dissociation of iodine could be easily achieved.

Due to its high reactivity, fluorine cannot be used in this graphite source. However, using this same design, a reliable atomic

and molecular fluorine source has been successfully operated[18] wherein the graphite nozzle components were replaced by pure nickel pieces of somewhat smaller size.

In its present form this source has been used at pressures of two atmospheres or less. It is limited in operating pressure by the "O"-ring fitting which attaches the stainless steel gas feed line to the graphite nozzle, although we have not determined the actual maximum operating pressure of this fitting. By metal plating the end of the nozzle and brazing the gas feed line to it, the safe operating pressure of the nozzle could probably be increased, limited only by the bursting strength of the graphite tube. Operation of the nozzle at higher pressures should result in less slippage and higher energies for seeded mixtures of halogens in light carrier gases, such as Cl_2 in He, at high temperatures. At a given pressure the gas number density (∝ 1/T) is considerably reduced at high temperatures, so operation of the nozzle at pressures of several atmospheres will not impose an unmanageable load on the pumping system.

We have not operated the nozzle at temperatures higher than 2100 K. This limitation is due to a limit on the heating power available. Since the maximum working temperature of graphite in vacuum is about 2300 K considerable increase in beam energy can be achieved with this source, if the heating power can be further increased.

C. References

1. R. B. Bernstein, in Advances in Chemical Physics (Wiley, New York, 1966), Vol. 10, p. 75.
2. R. D. Levine and R. B. Bernstein, Molecular Reaction Dynamics (Oxford University Press, New York, 1974).
3. E. H. Kennard, Kinetic Theory of Gases (McGraw-Hill, New York, 1938).
4. H. Pauly and J. P. Toennies, in Methods of Experimental Physics (Academic Press, New York, 1968), Vol. 7A, p. 227.
5. J. A. Giordmaine and T. C. Wang, J. Appl. Phys., 31, 463 (1960).
6. J. B. Andersen and J. B. Fenn, Phys. Fluids, 8, 780 (1965).
7. H. Ashkenas and O. Hagena, in Rarefied Gas Dynamics (Academic Press, New York, 1966), Vol. 2, p. 260.
8. J. G. Skofronik, Rev. Sci. Instr., 38, 1628 (1967).
9. G. Scoles and F. Torrello, "Production of Molecular Beams from Free Expanding Jets, part 1", Report of the Gruppo di Strutture Della Materia del C.N.R., August 1967.
10. R. Campargue, in Rarefied Gas Dynamics (DFVLR Press, Porz-Wahn, Germany, 1974), Vol. 9, p. C11-1.
11. M. Abauf, J. B. Anderson, R. P. Andres, J. B. Fenn, and D. G. H. Marsden, Science, 155, 997 (1967).
12. F. P. Tully, Y. T. Lee, and R. S. Berry, Chem. Phys. Lett., 9, 80 (1971).
13. E. E. Parks and S. Wexler, Chem. Phys. Lett., 10, 245 (1971).
14. S. B. Jaffe and J. B. Anderson, J. Chem. Phys., 51, 1057 (1969).
15. M. E. Gersch and R. B. Bernstein, J. Chem. Phys., 56, 6131 (1972).

16. J. G. Pruett, F. R. Grabiner and P. R. Brooks, J. Chem. Phys., 60, 3335 (1974).

17. H. J. Loesch and D. R. Herschbach, J. Chem. Phys., 51, 2038 (1972).

18. This source is described in Chapter III of this work.

19. Y. T. Lee, J. D. McDonald, P. R. Lebreton and D. R. Herschbach, J. Chem. Phys., 49, 2447 (1968).

20. L. Davis, B. T. Feld, C. W. Zabel and J. R. Zacharias, Phys. Rev., 76, 1976 (1949).

21. E. A. Ogryzlo, Can. J. Chem., 39, 2556 (1961).

22. J. J. Valentini and D. J. Auerbach, unpublished, R. J. Buss and M. J. Coggiola, unpublished.

23. C. H. Becker, J. J. Valentini and Y. T. Lee, Abstr. Thirty First Symposium on Molecular Spectroscopy, Ohio State University, 123 (1976).

24. Carbonundum Co., Graphite Products Division, Sanborn, N.Y.

25. Cajon Co., Cleveland, Ohio.

26. Y. T. Lee, J. D. McDonald, P. R. Lebreton and D. R. Herschbach, Rev. Sci. Instr., 40, 1402 (1969).

27. The recovery procedure is descrived in Chapter V of this work.

28. G. S. Aitken and R. S. Freund, Rev. Sci. Instr., 40, 1515 (1969).

29. H. H. Hostettler and R. B. Bernstein, Rev. Sci. Instr., 31, 872 (1960).

FIGURE CAPTIONS

Fig. 1. Schematic diagram of a molecular beam apparatus using a molecular effusion source. II and III are the source and experimental chambers. Typical operating conditions are $P_o \simeq 10^{-1}$ torr, $P_{II} \simeq 10^{-4}$-10^{-5} torr, $P_{III} \simeq 10^{-7}$ torr.

Fig. 2. Schematic diagram of a molecular beam apparatus using a nozzle source. I, II and III are the source, differential pumping, and experimental chambers respectively. Typical operating conditions are $P_o \simeq$ 200-1000 torr, $P_I \simeq 10^{-4}$ torr, $P_{II} \simeq 10^{-5}$ torr, $P_{III} \simeq 10^{-7}$ torr.

Fig. 3. Partially sectioned view of graphite nozzle source. A - water cooling lines for O-ring cooling block; B - nozzle retaining plate; C - springs; D - water cooling lines for support block; E - copper support block; F - graphite sleeve; G - water cooling channel; H - copper mounting block; I - outer graphite tube; J - tantalum radiation shield; K - inner graphite tube; L - graphite retaining nut; M - mica insulation; N - Cajon ultratorr fitting; O - copper O-ring cooling block; P - water cooling lines for mounting block; Q - gas inlet line.

Fig. 4. Heating current paths for graphite nozzle. E - copper support block and current return; F - graphite sleeve; H - copper mounting block and current supply; I - outer graphite tube; K - inner graphite tube; L - graphite retaining nut.

Fig. 5. Sectioned view of graphite nozzle source mounted in the differentially pumped chamber. A - Lucite insulating feedthroughs; B - water cooling for mounting block, and current supply; C - gas inlet line; D - water cooling for support block, and current return; E, J - Cajon ultratorr fittings; F - water supply for O-ring cooling block; G - nylon insulating feedthroughs; H - stainless steel outer source chamber; I - front plate water cooling lines; K - stainless steel inner source chamber; L - 1200 ℓ/sec diffusion pump, differential region; M - 2400 ℓ/sec diffusion pump, source region.

Fig. 6. Peak flux velocities for chlorine atoms (■) chlorine molecules (●) and diluent gas (▼) as a function of source temperature for three seeded gas mixtures. Solid curves indicate expected velocity dependence assuming an ideal seeded beam expansion, see text.

Fig. 7. Peak flux velocities for chlorine atoms (□) and chlorine molecules (○) as a function of source stagnation pressure. Seeded mixture was 0.98% Cl_2 in He at a source temperature of 1470 K.

Fig. 8. Peak flux velocities for bromine atoms (■), bromine molecules (●) and diluent gas (▼) as a function of source temperature. The seeded mixture was 6.3% Br_2 in Ar. The solid curve shows the expected velocity dependence assuming an ideal expansion, see text.

Fig. 9. $Br:Br_2$ ratio as a function of source temperature. Gas mixture was 6.3% Br_2 in Ar at a stagnation pressure of 1000 torr. Data has been corrected for electron impact fragmentation of Br_2 occurring in the detector ion source.

Fig. 10. $Cl:Cl_2$ ratio as a function of source temperature. Gas mixture was 0.98% Cl_2 in He at a stagnation pressure of 1000 torr. Data has been corrected for electron impact fragmentation of Cl_2 occurring in the detector ion source.

Fig. 11. Nozzle source temperature as a function of input heating power. (□) - effective source temperature derived from rare gas time-of-flight distributions, (○) nozzle tip temperature determined from optical pyrometry.

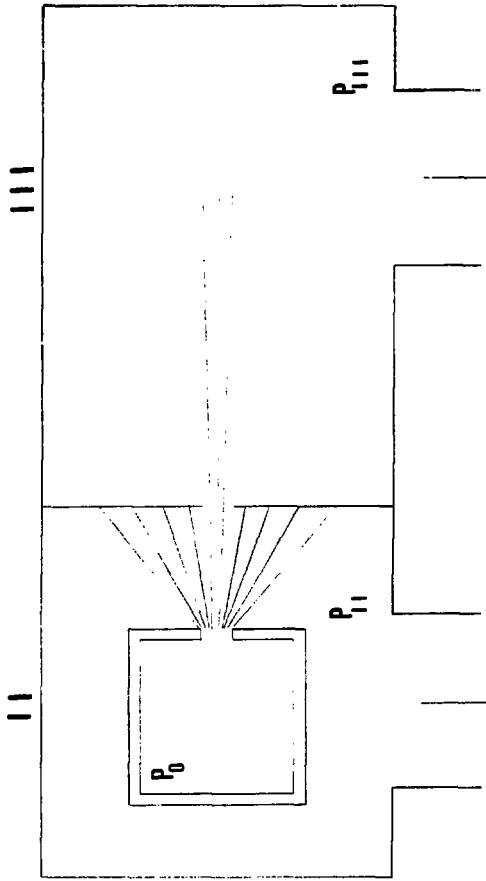

XBL 7610-4949

Fig. 1

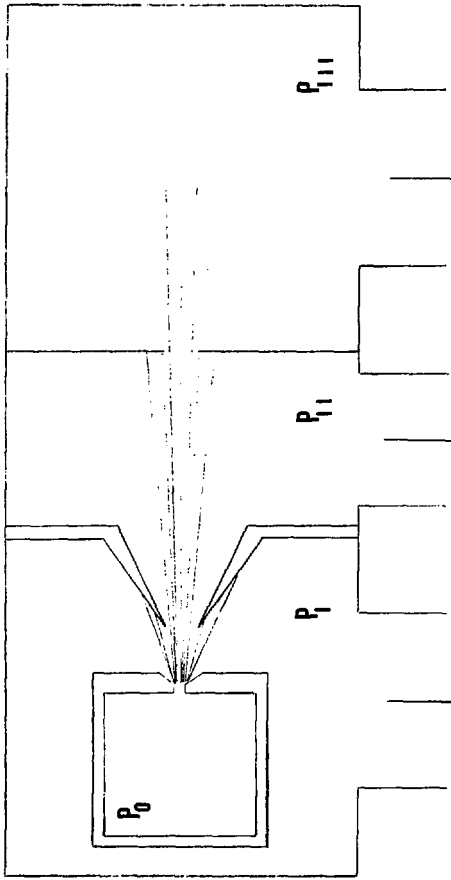

Fig. 2

XBL 7610-4950

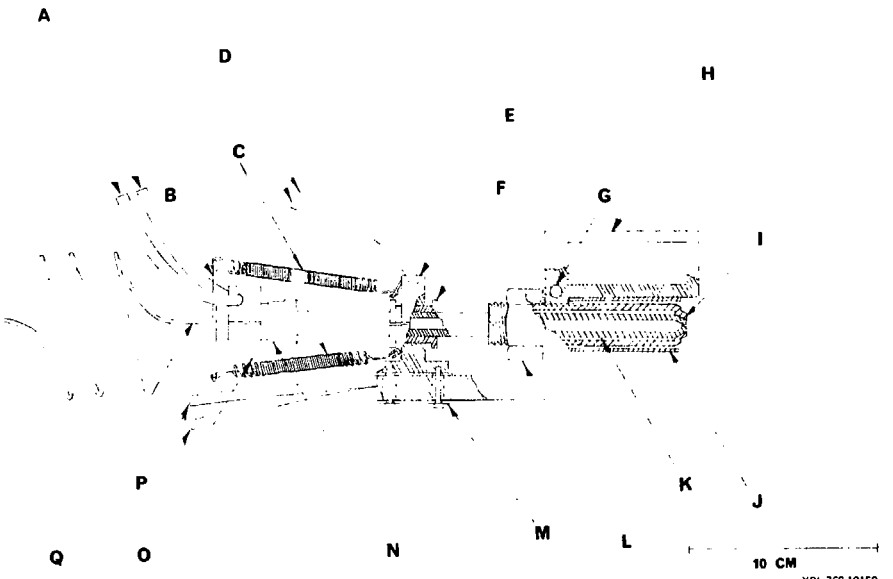

Fig. 3

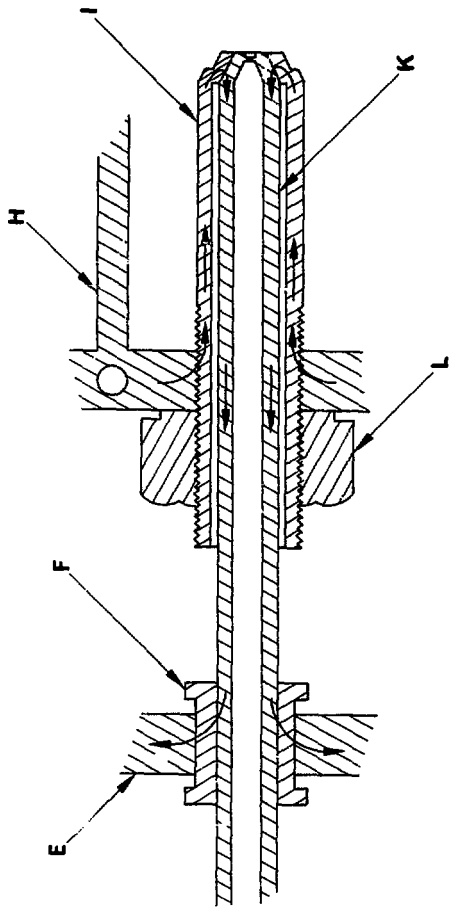

XBL 768-379

Fig. 4

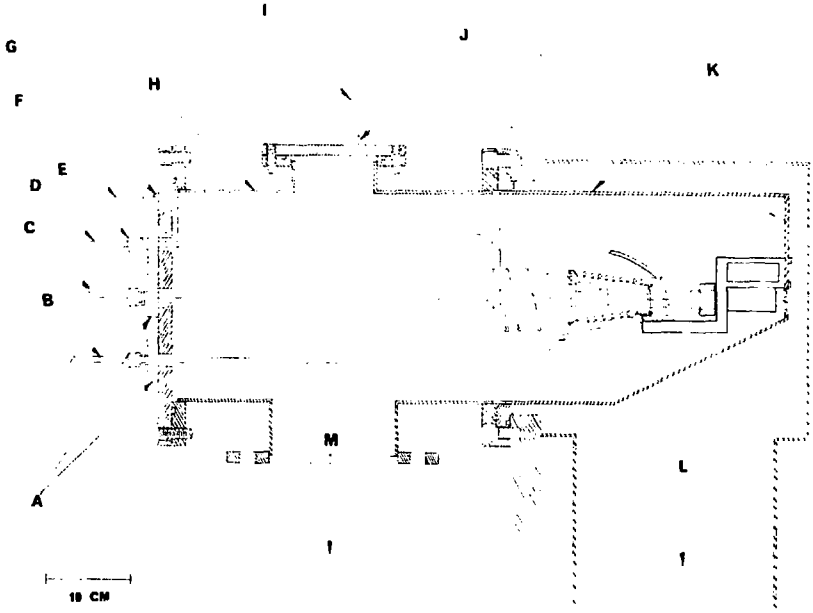

Fig. 5

XBL 760-8080

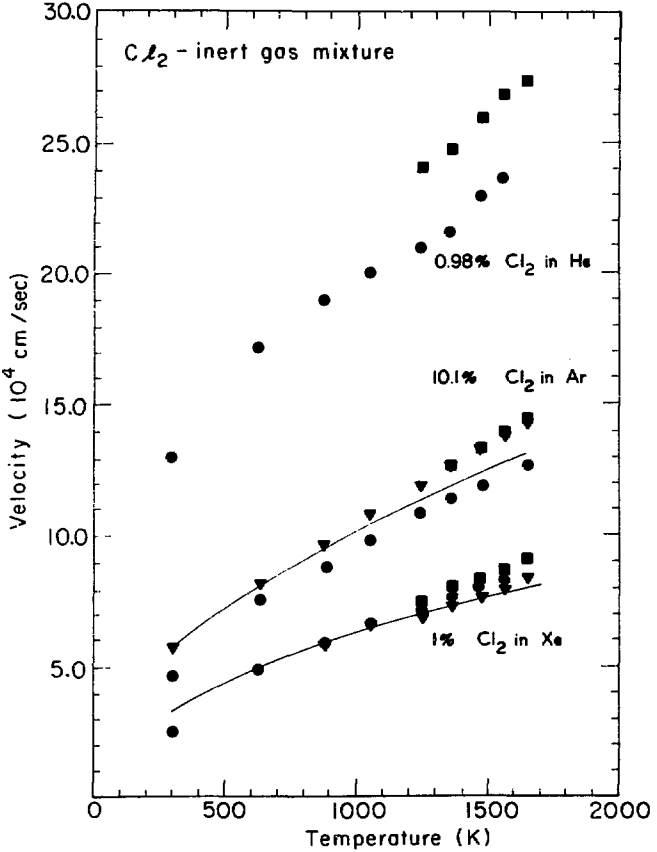

Fig. 6

XBL 767-3100

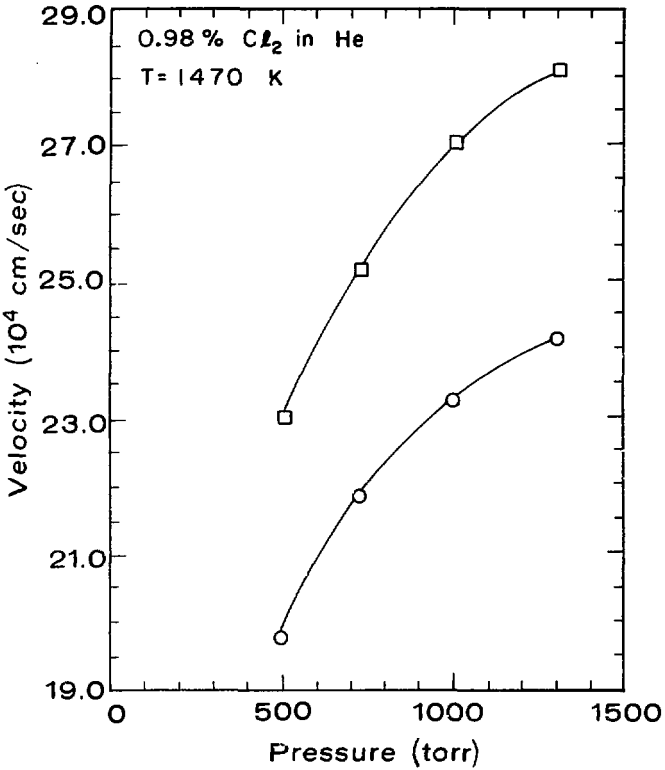

Fig. 7

XBL 767 3096

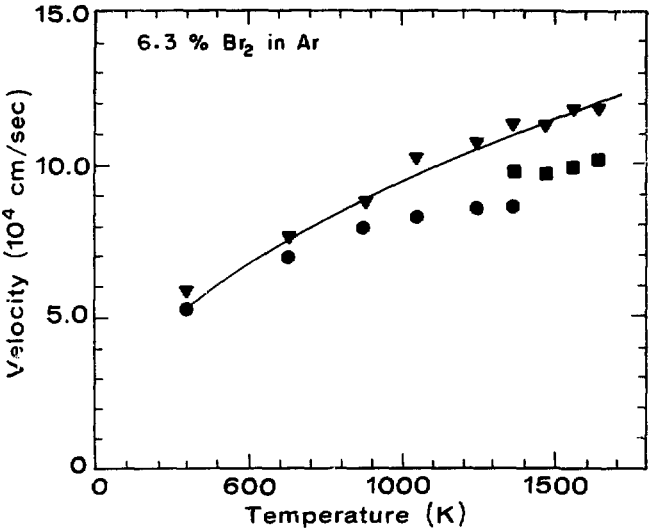

Fig. 8

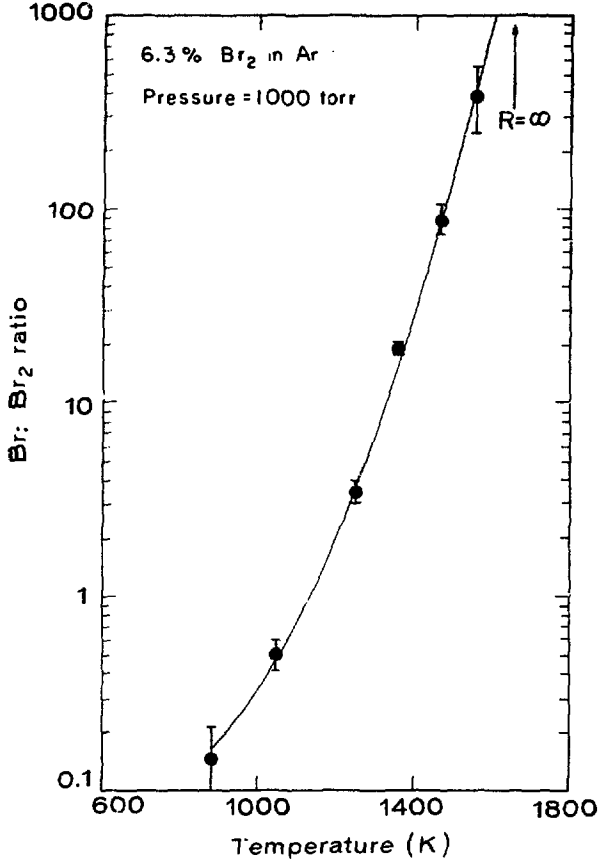

Fig. 9

XBL 767 3098

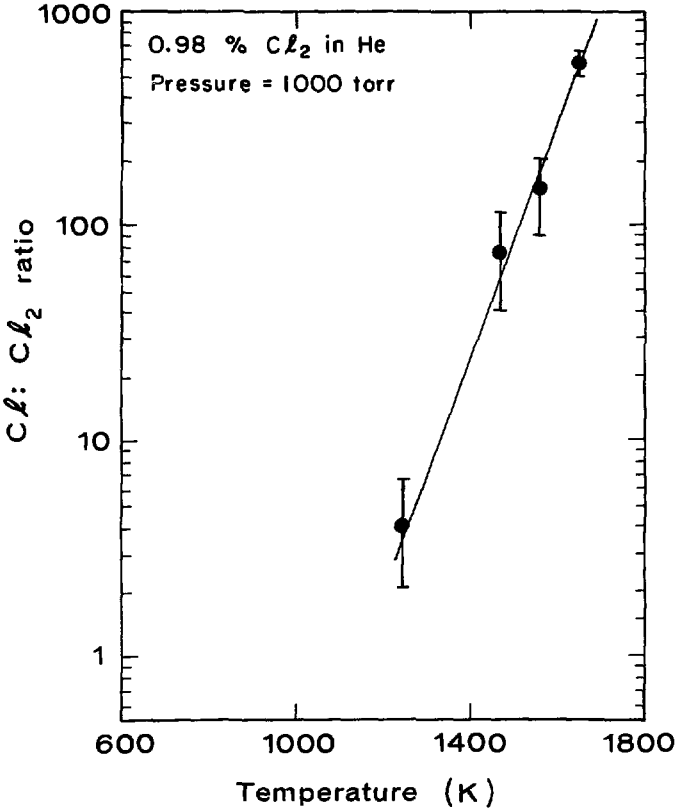

Fig. 10

XBL 767 3099

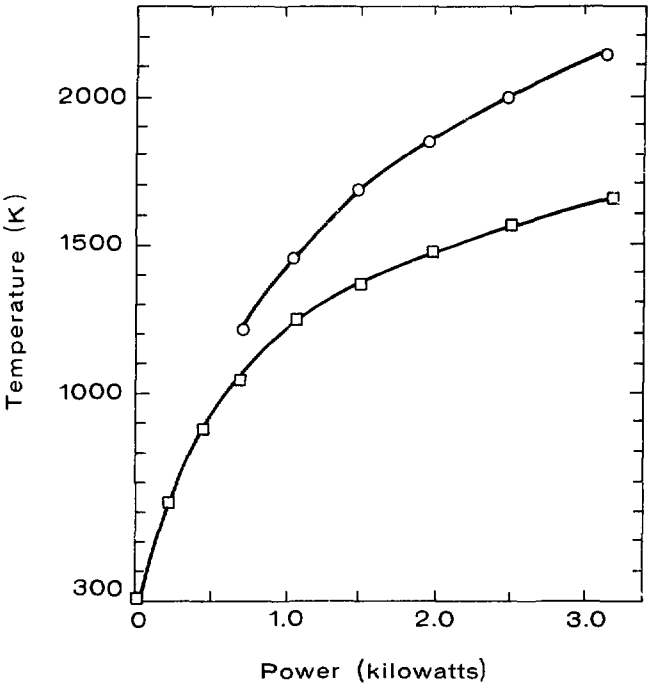

Fig. 11

XBL 766 3050

III. ENDOERGIC BIMOLECULAR REACTIONS: PRODUCTION OF STABLE TRIHALOGEN RADICALS

A. Introduction

Exchange reactions of halogen molecules, for which the net reaction is $X_2 + Y_2 \rightarrow 2XY$, for example $F_2 + I_2 \rightarrow 2IF$, comprise a very interesting system of reactions for the chemical kineticist. It has long been believed that these exchange reactions proceed either via a bimolecular four-center mechanism, whereby two product molecules are formed simultaneously, or via atom-molecule reactions initiated by thermal decomposition of halogen molecules into atoms.

Both of these mechanisms are expected to have high activation energy. The four-center mechanism is expected to have an activation barrier above the dissociation energy of the weaker reactant halogen bond, since a molecular orbit. correlation diagram given by Hoffman[1] shows that the barrier should be comparable to the promotion energy of two electrons from bonding to anti-bonding orbitals. A more complete orbital correlation diagram, including π as well as σ molecular orbitals,[2] predicts a somewhat lower barrier, but which still is comparable to the energy required to promote two electrons from bonding to anti-bonding orbitals. Since the atom-molecule mechanism has as its chain initiating step the dissociation of a halogen molecule it is also expected to have a large activation barrier.

Yet experimental rate studies of systems such as $I_2 + Br_2$ and $Cl_2 + Br_2$ in both gas phase[3,4] and "inert" solvent[5-7] have found a rather facile reaction with low activation energy. Of course in the gas phase surface effects and heterogeneous character of the system

cannot be eliminated, while in "inert" solution solvent effects and catalysis by impurities such as water may be important.[7,8]

A very recent investigation of the gas phase reaction of F_2 and I_2 in which contaminants and surface effects should play a negligible part presents very compelling evidence for a low activation energy reaction. In this reaction, studied in a low pressure flow system at room temperature, Johnston and co-workers[9] observed the IF product by monitoring the chemiluminescence from the $A^3\Pi_1$ and $B^3\Pi_o^+$ states of IF. This observation of the production of electronically excited IF in the room temperature reaction requires a mechanism which not only has a low activation energy, but which also has an IF producing step which is exoergic by about 65 kcal/mole, that is sufficiently exoergic to product IF in high vibrational levels of the B state.

The recent observation of the formation of stable CH_3IF from the crossed beam reactions of F_2 and CH_3I at collision energies above 10 kcal/mole,[10]

$$F_2 + CH_3I \longrightarrow CH_3IF + F, \qquad (1)$$

suggests a previously unanticipated reaction between halogen molecules, e.g.

$$F_2 + I_2 \longrightarrow I_2F + F. \qquad (2)$$

If the energy threshold for reaction (2) is low, as is that of (1), this reaction might be an important step in the $F_2|I_2$ exchange mechanism. Similar reactions might be important in other $X_2|Y_2$ exchange reactions.

In addition to its possible importance in $X_2|Y_2$ exchange reaction kinetics, reaction (2) is also interesting because it produces a trihalogen radical species such as I_2F. There has long been speculation regarding the existence of such triatomic halogen molecules.[11] These molecules have often been postulated as intermediates in photochemical reactions.[12-14] From the temperature dependence of the recombination rate of I atoms in the presence of I_2 the stability of I_3 has been estimated to be about 5 kcal/mole.[14] Cl_3[15] and ClF_2[16] are believed to have been identified from infrared spectra in matrix isolation experiments, but no triatomic halogen radical species has ever been detected in the gas-phase before this work.[17]

To determine the energetics of the formation of trihalogen radicals and to investigate the dynamics of halogen molecule exchange reactions we have studied a series of reactions, F_2 + XI where X = I, Cl, or H. The results of this study considerably improve our understanding of these molecule-molecule reactions, establish the energetics of trihalogen molecule formation, and allow us to propose a mechanism for the $F_2|I_2$ reaction which does explain the low activation energy and chemiluminescence.

B. Experimental

The crossed molecular beam apparatus, which has been described in detail elsewhere,[18] is shown schematically in Figure 1. Reactant beams of XI (I_2, ICl, or HI) and F_2 were produced by supersonic nozzle sources. The fluorine molecule beam was produced by the "seeding" technique. Mixtures of F_2 (1-2%) in He or He|Ne carrier gases were

used to vary the fluorine beam energy, and hence the collision energy. These fluorine mixtures were obtained commerically or made in the laboratory as needed for these experiments. The fluorine nozzle source used for these experiments was a resistance heated nickel nozzle quite similar in design and identical in operation to the graphite nozzle source described in Chapter II. The nozzle temperature was varied between 300 and 900 K by varying the heating power (up to about 90 amps and 5 volts AC) supplied by a low voltage-high current power supply. A chromel:alumel thermocouple spot-welded to the nozzle tip provided temperature monitoring. Heating of the nozzle provided the "fine" control of the collision energy. There was no appreciable F atom production at the higher nozzle temperatures.

The I_2 and ICl beams were also produced by the "seeding" technique, since the vapor pressures of these compounds are insufficient at low temperatures (400 K or less) to allow operation of a nozzle source. These beams were produced by flowing argon through a reservoir containing the I_2 or ICl and then flowing the mixed gas to the nozzle. The reservoir containing the I_2 or ICl was temperature controlled to ensure a constant partial pressure of the I_2 or ICl. For I_2 the reservoir was heated to about 350 K, while for ICl the reservoir was maintained at room temperature. The argon pressure was controlled by a vacuum regulator to provide stable operation at pressures below one atmosphere. The gas feed line from the nozzle to the reservoir and the nozzle itself were heated (350 - 400 K) to prevent condensation of the I_2 or ICl. The HI beam was generated without the use of a carrier gas. In

all cases a glass or quartz nozzle was used. Heating of the nozzle was provided by passing AC current through nichrome wire wrapped around the nozzle. The nozzle temperature was monitored by a chromel:alumel thermocouple firmly attached to the nozzle tip. This crossed beam arrangement resulted in a range of collision energies from 3 to 20 kcal/mole, with a spread in energy of ±25%.

Molecules produced by the reaction of F_2 and XI were detected in the plane of the reactant beams using a rotatable quadrupole mass spectrometer equipped with an electron bombardment ionizer. After mass selection by the mass spectrometer the ions produced are focused on an electrode held at a large negative potential (-30 kV), from which electrons are ejected. These ejected electrons, accelerated in the electric field of this electrode, strike a plastic scintillator. The light pulses thus produced are picked up by a photmultiplier and the output pulses of the photomultiplier, proportional in number to the product molecule number density, are recorded. In this way the angular distribution of the products was measured.

Product velocity distributions at selected angles were also determined by means of a cross correlation time-of-flight technique.[19] For these measurements the product molecules were modulated at the detector entrance aperture by a rotating wheel, the periphery of which consists of a pseudo-random binary sequence of open and closed slots. By correlating the modulating function with the observed distribution of flight times recorded by a 256 channel scaler the true distribution of flight times was recovered. On-line computer control and data reduction was used to allow immediate recovery of the time-of-flight

distribution of the products. Velocity distributions were obtained from these time-of-flight distributions by techniques described in Chapter V.

Angular distribution data were obtained using counting times between 40 and 100 seconds for each point, and periodically returning to a reference angle to provide long-term normalization. Plotted angular distributions represent the average of several separate scans. Time-of-flight data were recorded for 15 to 45 minues depending on the signal level. Product angular and velocity distributions were measured in this way for several collision energies. In addition, separate experiments were carried out to accurately determine the energy threshold for product formation.

C. Results and Analysis

Any attempt to observe the trihalogen species XIF as a product of the endoergic reaction of F_2 and XI,

$$F_2 + XI \longrightarrow XIF + F, \tag{3}$$

will only be successful if reaction (3) is less endoergic than the reaction

$$F_2 + XI \longrightarrow X + IF + F, \tag{4}$$

that is, if XIF decomposition into IF and X is endoergic; and provided that the four-center exchange mechanism does not dominate. The present investigation shows that above threshold energies of 4, 6, and 11 kcal/mole respectively, collisions between F_2 and XI(X = I, Cl, H) do produce

principally XIF and F as in reaction (3). These threshold energies were determined from a measurement of the relative product signal as a function of the collision energy, the results of which are shown in Figure 2. As the collision energy is increased, reaction (4) becomes important, first for $F_2 + I_2$, and later for $F_2 + ICl$ also, but not for $F_2 + HI$ at the collision energies used here. The threshold energy for reaction (4) can be calculated from bond dissociation energies[20] (F_2: 36.7 kcal/mole, I_2: 35.6 kcal/mole, ICl: 49.8 kcal/mole, HI: 70.4 kcal/mole, IF: 66.4 kcal/mole) and is 6.1 kcal/mole, 20.1 kcal/mole, and 40.7 kcal/mole for X = I, Cl, and H respectively.

The stabilities of the XIF species (X = I, Cl, CH_3, H) have been derived from the experimentally measured thresholds for the reactions: $F_2 + XI \rightarrow XIF + F$, and the known F_2 and XI dissociation energies. Figure 3 gives an energy schematic for the trihalogens and pseudo-trihalogens discussed. It is interesting to note that I_2F is only about 3 kcal/mole more stable than I + IF. As the terminal atom (group) in XIF is changed through the sequence I, Cl, CH_3, H the trihalogen stability increases, reflecting the increased X-I diatomic (polyatomic) bond strength.

Angular distributions of both I_2F (m/e 273) and IF (m/e 146) products of the $F_2 + I_2$ reaction at three collision energies are shown in Figures 4 and 5. In each case, part of the measured IF^+ signal resulted from break-up of I_2F in the detector ionizer, hence a fraction of the I_2F signal has been subtracted from the IF signal, and the corrected IF angular distributions are also shown. The correction factor was

determined from the fragmentation ratio, $I_2F^+:IF^+$, for I_2F produced at collision energies (~5 kcal/mole) at which IF is not expected to form directly. At these collision energies, below the endoergicity of IF formation via reaction (4), the angular distributions of IF and I_2F are identical, the intensity of I_2F (arbitrary units) being just twice that of IF at every angle. Hence $I_2F^+:IF^+$ was ~2.0 for this detector using 200 eV ionizing electrons.

Figures 6 and 7 show corresponding angular distributions of ClIF (m/e 181, Cl^{35} IF) and IF from the F_2 + ICl reaction. Corrections to the IF signal for ClIF fragmentation have been made as for I_2F/IF. As can be seen in Figure 6 the ClIF and IF angular distributions are identical, within experimental error, for collision energies of 13.3 kcal/mole and 10.3 kcal/mole. Since the formation of IF via reaction (4) is 20.1 kcal/mole endoergic, this reactive channel is not open at these lower collision energies, and the IF observed must be produced by ionizer fragmentation of ClIF, as the angular distributions indicate. The ClIF fragmentation ratio, $ClIF^+:IF^+$, was thus 1.0 under these conditions. Although the reactive channel $F_2 + ICl \rightarrow Cl + IF + F$ is energetically inacessible at all the nominal collision energies indicated, there are F_2/ICl collisions involving F_2 molecules from the high velocity tail of the supersonic velocity distribution (±25% spread in energy) for the two higher collision energy experiments which are sufficiently energetic to produce IF. That this channel is open can be seen from the corrected (for ClIF fragmentation) IF distributions of Figure 7.

No IF distributions are shown in Figure 8 for the F_2 + HI system, as the reactive channel (4) producing IF is prohibitively endoergic (40.7 kcal/mole). Some IF^+ was produced by ionizer fragmentation, as determined from an investigation at high mass resolution, but the angular distributions shown were taken with less than unit mass resolution and represent the sum of the HIF^+ (m/e 147) and IF^+ (m/e 146) signals.

It is important to note that for the F_2 + ICl system there were no peaks in the mass spectrum at m/e 56 ($Cl^{37}F$) or m/e 54 ($Cl^{35}F$). In addition, for F_2 + HI no peak at m/e 20 (HF) was observed. This strongly suggests that the observed products are indeed ClIF and HIF, with the F atom attached to I, not to Cl or H as IClF or IHF. For I_2F and ClIF this is in agreement with the usual pattern of nuclear arrangements in non-hydrogenic triatomic ABC systems, which almost always have the least electronegative atom of the three at the middle position of the molecule. For all molecules with more than twelve valence electrons this general conclusion follows from the fact that the charge distribution of the π orbitals is generally more concentrated at the terminal atoms than at the center of the molecule. For F_2 + HI the absence of a peak at m/e 20 (HF) is less compelling evidence for the HIF nuclear arrangement than the corresponding absence of mass peaks at m/e 56 and m/e 54 is for the ClIF arrangement. Since m/e 20 is a mass with relatively high background due to the presence of Ar^{++}, the detector sensitivity to HF is correspondingly reduced.

Energetic considerations also support the HIF arrangement as the correct one. Since HF + I (135 kcal/mole) lies 39 kcal/mole below the stability of the pseudotrihalogen product of the F_2 + HI

reaction, stable by 96 kcal/mole with respect to the separated atoms, one does not expect to observe the pseudotrihalogen in F_2 + HI collisions if its structure is FHI. For such an arrangement the reaction would be expected to produce HF + I. One does not expect a significant energy barrier between FHI and HF + I, since the reaction Cl + HI → HCl + I, which must proceed through a Cl-H-I transition state, is a very fast reaction at thermal energies, often used as a pump reaction in HCl chemical laser systems.

From the angular distributions shown and from time-of-flight velocity analysis of the products, center-of-mass contour maps of product flux have been constructed. These are shown in Figures 9, 10, and 11.

These contour maps of $I_{c.m.}(\theta, u)$, the center-of-mass doubly differential reactive scattering cross section, were constructed by iterative deconvolution of the measured $\bar{I}_{LAB}(\Theta, v)$ cross section data, using a computer program described in Chapter V. This technique solves the equation:

$$\bar{I}_{LAB}(\Theta, v) = \sum_i f_i \frac{v^2}{u_i^2} I_{c.m.}(\theta_i, u_i) \qquad (5)$$

iteratively for $I_{c.m.}(\theta, u)$. The summation is taken over the range of transformation Newton diagrams generated by the finite widths of the beam velocity distributions and angular spreads, and f_i is the weighting factor for the $i^{\underline{th}}$ Newton diagram. Quantities with a bar indicate beam velocity and intersection angle averaged quantities.

For substantially endoergic reactions at collision energies not far in excess of the threshold, the reactive cross section is expected

to be quite strongly dependent on the collision energy. This is certainly the case for the reactions studied here. In the case of $F_2 + I_2$ and F_2 + ICl the energy dependence of the cross section for production of I_2F or ClIF is complicated by the presence of a second reactive channel, that which results in IF production. In order to obtain a center-of-mass distribution which would accurately reproduce the experimental data it was necessary to weight the Newton diagrams according to the energy dependence of the reactive cross sections. Hence, equation (5) becomes:

$$\bar{I}_{LAB}(\theta, v) = \sum_i f_E f_i \frac{v^2}{u_i^2} I_{c.m.}(\theta_i, u_i). \qquad (6)$$

The cross section energy dependences used in fitting all three systems were similar, namely a very rapid rise from threshold with increasing collision energy, gradually tapering off to a near plateau. The energy dependence was determined from experimental relative cross section measurements, the results of which are partially shown in Figure 2. For $F_2 + I_2 \rightarrow I_2F + F$ the cross section energy dependence was also measured up to collision energies of about 16.0 kcal/mole. The reactive cross section reaches a plateau at about 12 kcal/mole where the relative cross section is about 100 in the arbitrary units of Figure 2. For F_2 + ICl → ClIF + F, the cross section energy dependence was not measured at collision energies higher than about 12 kcal/mole, so a continuation of the curve shown in Figure 2 was made, similar in form to that for $F_2 + I_2$, but shifted by about 6 kcal/mole to higher energy. For F_2 + HI the curve of Figure 2 was

continued to a plateau at about 15 kcal/mole. These "extrapolations" were chosen so as to give an accurate fit to the experimental angular and velocity data, i.e. $\bar{I}_{LAB}(\theta, v)$, and so as to be physically consistent, that is to give a smoothly varying cross section energy dependence in good agreement with the experimental relative cross section data. The results of this analysis did not prove to be very sensitive to the exact form of the cross section energy dependence. The only important feature was the steep rise from threshold shown in Figure 2 gradually tapering off at high collision energy.

This energy weighting makes the most probable Newton diagram somewhat larger (~5%) than that which maximizes the quantity:

$$(v_1^2 + v_2^2)^{1/2} n_1 (v_1)\, n_2 (v_2), \qquad (7)$$

the product of the relative velocity and the number densities of the two beams. This energy weighting also makes the most probable collision energies somewhat larger (~10%) than the nominal collision energies, derived from the maximum in equation (7), which are given in the figures.

The experimental data and laboratory data calculated from the deconvoluted center-of-mass flux distributions are compared in Figures 12 and 13. The fit to the lab angular distributions and I_2F lab velocity distributions are quite good. Fits to the ClIF and HIF velocity distributions, not shown, are equally satisfactory.

The center-of-mass contour maps show the sharply forward peaked nature of the XIF products. It is significant that the I_2F distribution

is considerably narrower in recoil velocity than that of the ClIF or HIF products. In part this is a consequence of the more restrictive kinematics of the $I_2F + F$ system, for which the detected product is more than 14 times the mass of the other.[21] However, it is also indicative of a "thermodynamic" constraint of the products to large recoil velocity (energy) due to the low stability (~3 kcal/mole) of I_2F with respect to I + IF. This thermodynamic constraint allows formation of the trihalogen only when the excess energy channeled into translation of products is such that internal excitation of I_2F is not sufficient to dissociate it into IF and I. This behavior is evident in the I_2F lab angular distributions of Figure 4 and 5, which show only slight variation in going from 9.6 kcal/mole collision energy (~5.6 kcal/mole excess energy) to 17.0 kcal/mole collision energy (~13.0 kcal/mole excess energy). No such constraint exists, at the collision energies studied, for either ClIF, stable by 15 kcal/mole with respect to Cl + IF, or HIF, stable by 30 kcal/mole with respect to H + IF, and this is reflected in both the center-of-mass contour maps and lab angular distributions.

The thermodynamic constraint of the I_2F/F recoil energy distribution is even more clearly evident in Figure 14, which gives the intensity, $P(E_T')$, versus recoil energy, E_T', i.e. $\sum_{\theta} I_{c.m.}(\theta, E_T')$ for the systems studied. Here $I_{c.m.}(\theta, E_T') \propto I_{c.m.}(\theta, u)/u$. The I_2F/F distribution is much more sharply peaked than that for ClIF/F or HIF/F and peaks at an energy which represents a much larger fraction of the available energy than the ClIF/F distribution. The average product

translational energy,

$$\overline{E_T'} = \frac{\sum_{E_T'} P(E_T') \cdot E_T'}{\sum_{E_T'} P(E_T')} ,$$

is ~30% of the total available energy for ClIF production, while for the I_2F + F products more than 50% (5.1 kcal/mole) of the available energy appears in translation. For HIF production the average energy in translation is again high, 2.8 kcal/mole, ~47%. Any such comparison of product translational energies must of course recognize the rather substantial change in the reaction kinematics in changing the F atom abstracting species from I_2 to ICl to HI. However, the F_2 + I_2 and F_2 + ICl systems would seem to be similar enough kinematically to allow one to attribute the recoil energy distribution differences to the operation of this thermodynamic constraint.

It is clear that the increased sharpness of the I_2F lab angular distributions relative to those for ClIF and HIF is due to the sharpness in recoil velocity (energy) and not in recoil angle. This can be seen in Figure 15, which shows the center-of-mass angular distributions, where $I(\theta) = \sum_{E_T'} I_{c.m.}(\theta, E_T')$. The I_2F distribution is actually broader (~30° HWHM) than either the HIF or ClIF distributions (~15° HWHM). It is not clear whether the relative broadness of the I_2F distribution is dynamically significant or merely a consequence of the more unfavorable kinematics of the I_2F/F system which makes ratio method deconvolution of the center-of-mass distribution more difficult.

D. Discussion

The angular distributions of XIF and IF clearly indicate that the production of the trihalogen radical molecules XIF and the diatomic IF proceeds by reaction (3) and reaction (4), and not a reaction of XI dimer with F_2. If the XIF and IF observed were merely the result of fragmentation in the detector ionizer of some XIFF species produced by an $(XI)_2 + F_2 \rightarrow XIFF + XI$ reaction, or a reaction proceeding through a six-center collision complex as has been claimed for $(Cl_2)_2 + Br_2$,[22] the XIF and IF products should have identical angular distributions at all energies and the same energy threshold behavior. As can be seen in Figures 4 and 5 the I_2F and IF products of the $F_2 + I_2$ reaction have distinctly different angular distributions with different collision energy dependences. Although no angular distribution is shown for $F_2 + I_2$ in which only I_2F is produced, such angular distributions have been recorded at energies slightly in excess of the threshold for $F_2 + I_2 \rightarrow I_2F + F$ yet below the threshold (6.1 kcal/mole) for IF production via $F_2 + I_2 \rightarrow I + IF + F$.

Although the energetics are somewhat different, the F_2/ICl system shows the same behavior. The threshold for $F_2 + ICl \rightarrow Cl + IF + F$ is 20.1 kcal/mole, much higher than the analogous $F_2 + I_2$ threshold. If ClIF and IF production takes place via reactions (3) and (4), the IF and ClIF distributions should be identical until the collision energy is greater than 20.1 kcal/mole. Below this energy any IF observed would be due to fragmentation of ClIF in the detector ionizer. The ClIF and IF angular distribution data of Figures 6-8 bear this out. At collision energies of 10.3 kcal/mole and 13.3 kcal/mole the ClIF

and IF distributions are identical within the statistical uncertainty. At the higher collision energies the ClF and IF angular distributions differ markedly, indicative of the now energetically accessible $F_2 + ICl \rightarrow Cl + IF + F$ reaction. As pointed out earlier, although this reactive channel is still inaccessible at the nominal collision energies indicated, there are F_2/ICl collisions involving F_2 molecules from the high velocity tail of the supersonic beam velocity distribution (±25% spread in energy) which are sufficiently energetic to produce IF in this way. The behavior of both the F_2/I_2 and ICl systems are thus consistent with the operation of reactions (3) and (4).

Our results also indicate that these reactions do not proceed via a highly exoergic four-center exchange mechanism, $F_2 + XI \rightarrow XF + IF$. As has already been noted, for F_2 + ICl and F_2 + HI no ClF or HF products were detected. For $F_2 + I_2$ the four-center mechanism produces only IF, but this reaction is exoergic by more than 60 kcal/mole. If even a relatively small fraction of this energy appeared as product translation, the IF angular distributions would be much broader. For the angular distributions at 9.9 kcal/mole and 12.9 kcal/mole collision energies the maximum IF translational energies are only about 1 kcal/mole and 3 kcal/mole respectively, a very small fraction of the total available energies for the four-center mechanism, 70 kcal/mole and 73 kcal/mole respectively. Moreover, the IF angular distributions change quite a lot when the collision energy is raised from 9.9 kcal/mole to 17.0 kcal/mole, becoming much broader, clearly indicative of increased translational recoil energy. Such changes are not likely if the four-

center reaction is operative, as the total available energy increases only from 70 kcal/mole to 77 kcal/mole as the collison energy changes from 9.9 kcal/mole to 17.7 kcal/mole. This behavior is however consistent with the operation of the endoergic (6.1 kcal/mole) $F_2 + I_2 \rightarrow I + IF + F$ reaction, for which the total available energy increases from only 4 kcal/mole to 11 kcal/mole when the collision energy increases from 9.9 kcal/mole to 17.0 kcal/mole.

We have attempted to extend these studies of trihalogen energetics to systems not involving an XI-F bond. Crossing beams of Cl_2 and either ICl or IBr we attempted to observe the trihalogen species ClICl and ClIBr. However, even at collison energies greater than 40 kcal/mole for Cl_2 + ICl and greater than 43 kcal/mole for Cl_2 + IBr no trihalogen product could be detected. It may be that the cross sections for the Cl_2 + IBr and Cl_2 + ICl reactions are much smaller than those for the corresponding fluorine reactions, so much smaller that the amount of trihalogen produced is undetectable. It is more likely, however, that our failure to observe reaction in these systems is just a consequence of a much lower trihalogen stability for XICl species than for the corresponding XIF species and consequent higher threshold energy. The threshold energy for the $Y_2 + XI \rightarrow XIY + Y$ reaction is of course determined by the stability of XIY relative to Y_2. Since the Cl_2 dissociation energy (~58 kcal/mole) is about 20 kcal/mole higher than the F_2 dissociation energy, the Cl_2 + XI reactions are expected to have a higher threshold energy. However, the fact that the $Cl_2 + ICl \rightarrow ClICl + Cl$ reaction does not appear to proceed even at a collision energy as high as 40 kcal/mole implies that ClICl must be at least

14 kcal/mole less stable, with respect to the separated atoms, than ClIF, which has a threshold of 6 kcal/mole.

The negative results of the Cl_2 + ICl and Cl_2 + IBr experiments at collision energies of 40 and 43 kcal/mole respectively, yield upper limits to the stabilities, with respect to the separated atoms, of ClICl and ClIBr, 67 kcal/mole and 57 kcal/mole respectively. Since Cl + ICl is stable by 50 kcal/mole relative to the separated atoms, as is of course Br + ICl, it is possible that ClICl and ClIBr are stable with respect to Cl + ICl and Br + ICl. Even if this is the case, the thresholds for ClICl and ClIBr formation would be so high that these species would probably not be important in Cl_2/IBr or Cl_2/ICl exchange reactions at thermal energies.

These results present further evidence that the XIF and IF products observed in this study are not products of ionizer fragmentation of the XIFF product of the dimer reaction, $F_2 + (XI)_2 \rightarrow XIFF + XI$. Since this reaction involves the breaking of only van der Waals "bonds", the $Cl_2 + (XI)_2$ reactions should also proceed with low thresholds, contrary to the results presented here.

The very sharply forward peaked XIF distributions shown in the contour maps of Figures 10-12 for all three F_2 + XI systems would seem to indicate a preference for a bent geometry for F atom abstraction by XI, that is a preference for an F-F-I angle or F-I-X angle of less than 180° in F-F-I-X. When X=H the mass of X is negligible in comparison with I, and the F-I-X angle will not be an important determinant of the product angular distribution. The foward peaking of HIF is thus a

consequence of the bent F-F-I angle. Of course high energy collisions tend to favor forward peaking, and it is important to note that the IF produced in the $I + F_2$ reaction, kinematically identical to the $HI + F_2$ system, is backward peaked at thermal energies,[23] indicating that the bending angle of F-F-I must not be very large. The forward scattering of HIF observed in this work, in contrast to the backward peaking of IF from $I + F_2$, can be attributed to the difference in collision energy rather than to a larger bending angle for F-F-IH compared to F-F-I.

For X = I or Cl the mass of X is no longer negligible in comparison with I and both the F-F-I and F-I-X angles will be important. For the $F_2 + I_2$ and F_2 + ICl systems backward scattering of XIF at the higher collision energies is only possible if all four atoms are aligned collinearly in the critical configuration. The observed forward peaking of XIF clearly argues against such a geometry, favoring bending of one or both of F-F-I and F-I-X.

It must be noted that the ClIF angular distributions of Figures 6 and 7 appear to be backward peaked, i.e. peaked to the fluorine beam side of the center-of-mass angle. However, this center-of-mass angle is the correct c.m. angle for the Newton diagram which maximizes equation (7). As has been discussed above, the necessary energy weighting of the Newton diagrams will make the most probable Newton diagram somewhat larger (i.e. larger relative velocity) than that which maximizes equation (7). This larger Newton diagram will have a smaller c.m. angle, by 5° or so for F_2 + ICl. This energy weighting will also emphasize all of the larger Newton diagrams which occur in equation (6). As a result, although these angular distributions appear

distinctly backward peaked, when properly deconvoluted they will appear much less backward peaked or even forward peaked in the physically significant c.m. coordinate system. This effect can be clearly seen by comparing the ClIF lab angular distribution (Figure 8) at a collision energy of 17.4 kcal/mole, which appears to be only mildly forward peaked, with the deconvoluted c.m. contour map of this system at this energy (Figure 11), which is very sharply forward peaked. At lower collision energies where the cross section is more strongly dependent on the collision energy, such differences in lab angular distributions and c.m. contour maps will be even more pronounced.

Simple molecular orbital considerations[24] lead one to expect the F-F-I and F-I-X angles in FFIX to be quite similar, so it is likely that both F-F-I and F-I-X are slightly bent. There are however no ABC molecules with 21 valence electrons, like XIF, whose molecular geometry is exactly known, so it is difficult to precisely predict a preference for a particular F-F-I or F-I-X angle, nor can an unambiguous answer be determined from a simple M.O picture. Although Cl_3 is believed to be linear,[15] ClF_2 is thought to have a bond angle ~145°.[16,25] All known triatomic molecules with 20 valence electrons are bent (~100° bond angle), and those with 22 electrons are linear. It is thus not inconsistent to expect a slightly bent F-F-I and F-I-X geometry in F_2 + XI reactions.

The potentially important role played by stable radicals in promoting bimolecular chemical reactions such as F_2 + XI had not been suspected previously. The fact that a fluorine atom, which can initiate

a chain reaction in F_2/XI mixtures, can be generated in a collision between F_2 and XI through reaction (3) at a relative kinetic energy as low as 4 kcal/mole (for $F_2 + I_2$) is intriguing. This is especially so considering that 37 kcal/mole is necessary to dissociate F_2 and at least 36 kcal/mole to dissociate XI.

The threshold energy of reaction (4), which also produces an F atom, as well as an X atom, is 6.1 kcal/mole, 20.1 kcal/mole, and 40.7 kcal/mole for X = I, Cl, and H respectively. For the $F_2 + I_2$ and F_2 + ICl systems these energies are also smaller than the F_2 or XI bond dissociation energies. Even if XIF production by reaction (3) is not important, reaction (4) could be a significant source of F and X atoms in F_2/XI mixtures.

The results presented here have an important bearing on the interpretation of the results of the recent study by Johnston and co-workers[9] of the gas phase kinetics of the F_2/I_2 system. Johnston and co-workers were not able to establish a mechanism for this reaction which would have a low activation energy, and at the same time a very exoergic IF producing step to account for the observed chemiluminescence. Shown below are some of the possible IF producing steps:

$$F_2 + I_2 \longrightarrow 2IF \qquad (3)$$

$$F + I_2 \longrightarrow IF + I \qquad (9)$$

$$I + F_2 \longrightarrow IF + F \qquad (10)$$

$$I + F + M \longrightarrow IF + M \qquad (11)$$

$$I + IF_2 \longrightarrow 2IF \qquad (12)$$

$$F + I_2F \longrightarrow 2IF \qquad (13)$$

Reaction (8), the four-center exchange reaction, should have a high activation energy and was not observed in our study even at collision energies of almost 20 kcal/mole. It is thus not likely to be the IF producing step even though it is sufficiently exoergic to yield electronically excited IF. Reactions (9) and (10) are not sufficiently exoergic (-30 kcal/mole) to produce IF in either the A or B states. Reaction (11), the atom recombination reaction, where M is some third body, was dismissed by Johnston because the observed kinetics could only be reproduced by making physically unreasonable assumptions about the I and F termination reactions. While reaction (12) would probably be quite exoergic, IF_2 is not expected to be stable, and was not observed in our work. A crossed beam study[23] of the $I + F_2 \rightarrow IF + F$ reaction showed that the IF product was backward peaked, indicating that the $I - F_2$ interaction is not attractive.

This leaves reaction (13) which is about 64 kcal/mole exoergic. It has as reactants species which are produced at thermal energies (4 kcal/mole or greater) by reaction (3). Hence it agrees well with the observation of IF^* production at room temperature. The mechanism for the exchange reaction producing electronically excited IF, assuming reaction (13) is the IF^* producing step, would be:

$$F_2 + I_2 \xrightarrow{k_1} I_2F + F$$

$$F + I_2F \xrightarrow{k_2} IF + IF^*$$

$$IF^* \xrightarrow{k_3} IF + h\nu$$

$$IF^* + M \xrightarrow{k_4} IF + M.$$

Making a standard steady-state approximation for $[I_2F]$, the concentration of I_2F, yields

$$[IF^*] = \frac{k_1/k_2[F_2][I_2]}{k_4[M] + k_3}.$$

Not included in the above mechanism are the fast atom-molecule exchange reactions:

$$F + I_2 \longrightarrow IF + I,$$

$$I + F_2 \longrightarrow IF + F.$$

which are just the chain propagating steps of the atom-molecule exchange mechanism. These two reactions will have no effect on the form of the expression for [IF*] derived above, but they will of course be the pincipal reactions producing ground state IF. Although the dependence of the chemiluminescence on the concentration of F_2, I_2, and M was measured only over a limited range of concentration by Johnston and co-workers, the expression above is consistent with the concentration dependence that was measured.

E. References

1. R. Hoffman, J. Chem. Phys., 49, 3739 (1968).
2. D. A. Dixon, D. L. King, and D. R. Herschbach, Disc. Faraday Soc., 55, 375 (1973).
3. W. Jost, Z. Physik, Chem., B14, 413 (1931).
4. G. Brauer and E. Victor, Z. Elektrochem., 41, 508 (1935).
5. P. R. Walton and R. M. Noyes, J. Amer. Chem. Soc., 88, 4325 (1966).
6. P. R. Walton and R. M. Noyes, J. Phys. Chem., 71, 1952 (1967).
7. P. Schweitzer and R. M. Noyes, J. Amer. Chem. Soc., 93, 356 (1971).
8. J. Hildebrand, J. Amer. Chem. Soc., 68, 915 (1946).
9. J. W. Birks, S. D. Gabelnick, and H. S. Johnston, J. Mol. Spectrosc., 57, 23 (1975).
10. J. M. Farrar and Y. T. Lee, J. Amer. Chem. Soc., 96, 7570 (1974).
11. G. K. Rollefson and H. Eyring, J. Amer. Chem. Soc., 54, 170 (1932).
12. M. I. Christie, A. J. Harrison, R. G. W. Norrish, and G. Porter, Proc. Roy. Soc. (London), A231, 446 (1955).
13. P. F. Ashmore, F. S. Dainton, and T. M. Sugden, Eds., Photochemistry and Reaction Kinetics (Cambridge University Press, London, 1967), pp. 75, 81, 103, 115.
14. D. L. Bunker and N. Davidson, J. Amer. Chem. Soc., 80, 5090 (1958).
15. L. Y. Nelson and G. C. Pimentel, J. Chem. Phys., 47, 3671 (1967).
16. G. Mamantov, E. J. Vasini, M. C. Moulton, D. G. Vicktroy and T. Maekawa, J. Chem. Phys., 54, 3419 (1971).
17. J. J. Valentini, M. J. Coggiola, and Y. T. Lee, J. Amer. Chem. Soc., 98, 853 (1976).

18. Y. T. Lee, J. D. McDonald, P. R. Lebreton, and D. R. Herschbach, Rev. Sci. Instr., 40, 1402 (1969).

19. V. L. Hirschy and J. P. Aldridge, Rev. Sci. Instr., 42, 381 (1971).

20. B. Darwent, Bond Dissociation Energies in Simple Molecules, National Bureau of Standards, Washington, 1970, NSRD-NDB-31.

21. For a discussion at kinematics and the lab to c.m. transformation problem see M. A. D. Fluendy and K. P. Lawley, Chemical Applications of Molecular Beam Scattering (Chapman and Hall, London, 1973).

22. D. L. King, D. A. Dixon, and D. R. Herschbach, J. Amer. Chem. Soc., 96, 3328 (1974).

23. Y. C. Wong, unpublished.

24. A. P. Walsh, J. Chem. Soc., 2266 (1953).

25. S. R. Ungemach and H. F. Schaefer, J. Amer. Chem. Soc., 98, 1658 (1976).

FIGURE CAPTIONS

Fig. 1. Schematic diagram of the crossed molecular beam apparatus used in the study of F_2 + XI reactions.

Fig. 2. Energy dependence of the relative total cross sections for the reactions: (○) $F_2 + I_2$; (●) F_2 + ICl; (△) F_2 + HI.

Fig. 3. Schematic energy diagram showing the stabilities of the XIF, X = I, Cl, CH_3, and H, trihalogens and pseudo-trihalogens. All energies are in kcal/mole with respect to the separated atoms shown at the top.

Fig. 4. ● Experimental laboratory angular distribution of IF produced in the reaction $F_2 + I_2$ at collision energies of 12.9 and 9.7 kcal/mole; ◇ experimental laboratory angular distribution of I_2F produced in the same reaction: ○ IF angular distribution corrected for I_2F^+/IF^+ fragmentation, see text.

Fig. 5. ● Experimental laboratory angular distribution of IF produced in the reaction $F_2 + I_2$ at a collision energy of 17.0 kcal/mole; ◇ experimental laboratory angular distribution of I_2F produced in the same reaction; ○ IF angular distribution corrected for I_2F^+/IF^+ fragmentation, see text.

Fig. 6. ● Experimental laboratory angular distribution of IF produced in the reaction F_2 + ICl at collision energies of 10.3 and 13.3 kcal/mole; ◇ experimental laboratory angular distribution of ClIF produced in the same reaction; ○ IF angular distribution corrected for $ClIF^+/IF^+$ fragmentation, see text.

Fig. 7. ● Experimental laboratory angular distribution of IF produced in the reaction F_2 + ICl at collision energies of 17.4 and 16.1 kcal/mole; ◇ experimental laboratory angular distribution of ClIF produced in the same reaction; ○ IF angular distribution corrected for $ClIF^+/IF^+$ fragmentation, see text.

Fig. 8. ● Experimental laboratory angular distribution of HIF produced in the reaction F_2 + HI at collision energies of 16.1 and 14.9 kcal/mole.

Fig. 9. Contour map of I_2F flux density in the center-of-mass coordinate system produced in the reaction F_2 + I_2 at a collision energy of 12.9 kcal/mole. These contours were obtained by fitting the experimental laboratory angular and velocity distributions.

Fig. 10. Contour map of ClIF flux density in the center-of-mass coordinate system produced in the reaction F_2 + ICl at a collision energy of 17.4 kcal/mole. These contours were obtained by fitting the experimental laboratory angular and velocity distributions.

Fig. 11. Contour map of HIF flux density in the center-of-mass coordinate system produced in the reaction F_2 + HI at a collision energy of 16.1 kcal/mole. These contours were obtained by fitting the experimental laboratory angular and velocity distributions.

Fig. 12. ○ Experimental laboratory angular distributions of I_2F, ClIF and HIF produced from the reactions F_2 + I_2, ICl and HI

at collision energies of 12.9, 17.4 and 16.1 kcal/mole, respectively; — best fit laboratory angular distributions calculated by transforming $I_{c.m.}(\theta, u)$ (figures 8-10) to the laboratory frame using a full range of Newton diagrams, and then summing oven laboratory velocities.

Fig. 13. □ Experimental laboratory velocity distribution of I_2F produced in the reaction $F_2 + I_2$ at a collision energy of 12.9 kcal/mole at four laboratory angles; — laboratory velocity distribution derived from the center-of-mass product distribution shown in figure 8.

Fig. 14. ● Product recoil energy distributions for I_2F, ClIF and HIF produced in the reactions $F_2 + I_2$, ICl and HI at collision energies of 12.9, 17.4 and 16.1 kcal/mole, respectively, obtained by angle averaging $I_{c.m.}(\theta, E_T')$. Vertical dashed line represents the approximate kinematic recoil energy limit.

Fig. 15. ○ Center-of-mass angular distributions of I_2F, ClIF and HIF produced in the reactions $F_2 + I_2$, ICl and HI at collision energies of 12.9, 17.4 and 16.1 kcal/mole, respectively, obtained by averaging $I_{c.m.}(\theta, E_T')$ over recoil energy, for center-of-mass angles $\theta \leqslant 180$; □ corresponding center-of-mass angular distributions for center-of-mass angles $\theta \geqslant 180$, plotted for $2\pi - \theta$; — smoothed center-of-mass angular distribution representing the smoothed average of each set of points.

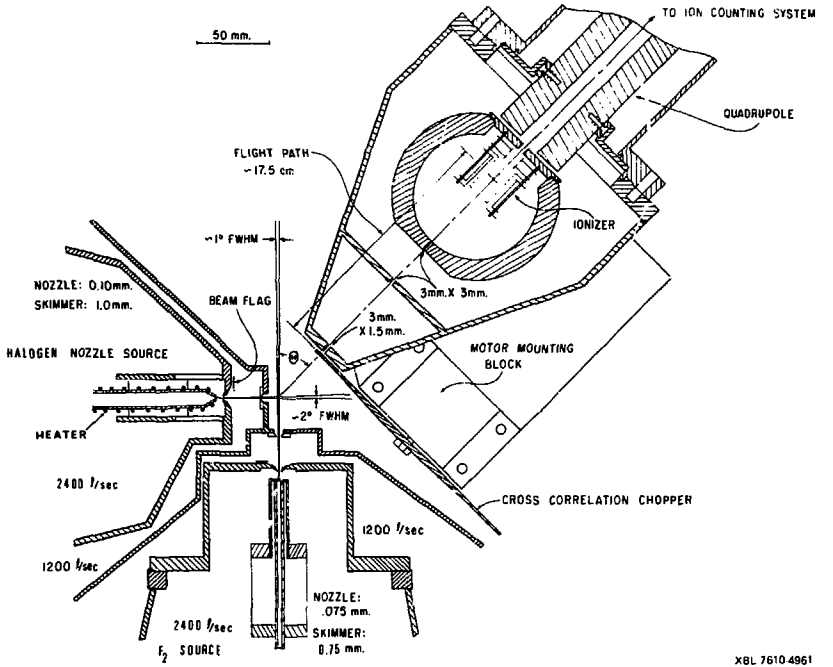
50 mm.
TO ION COUNTING SYSTEM
QUADRUPOLE
FLIGHT PATH
~17.5 cm
IONIZER
~1° FWHM
NOZZLE: 0.10mm.
SKIMMER: 1.0mm.
BEAM FLAG
3mm.X 3mm.
3mm.
X1.5mm.
HALOGEN NOZZLE SOURCE
θ
MOTOR MOUNTING
BLOCK
~2° FWHM
HEATER
2400 l/sec
CROSS CORRELATION CHOPPER
1200 l/sec
1200 l/sec
NOZZLE:
.075 mm.
2400 l/sec
SKIMMER:
0.75 mm.
F2 SOURCE
XBL 7610-4961

Fig. 1

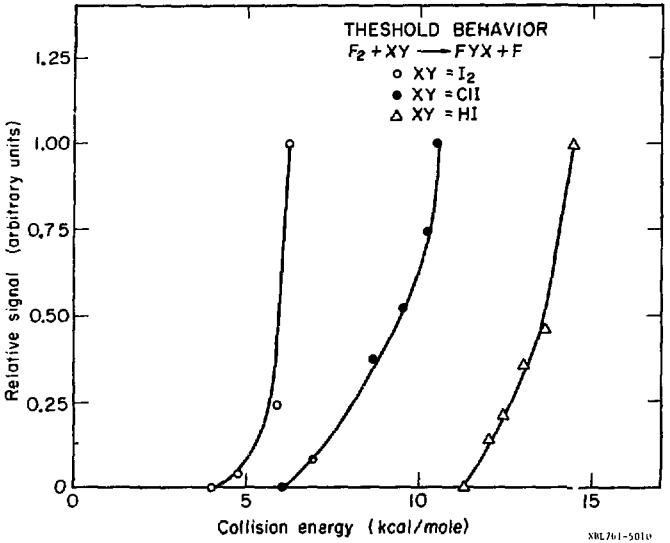
THESHOLD BEHAVIOR
$F_2 + XY \longrightarrow FYX + F$
o XY = I_2
● XY = ClI
△ XY = HI
Relative signal (arbitrary units)
1.25
1.00
0.75
0.50
0.25
0
0
5
10
15
Collision energy (kcal/mole)
XBL761-5010

Fig. 2

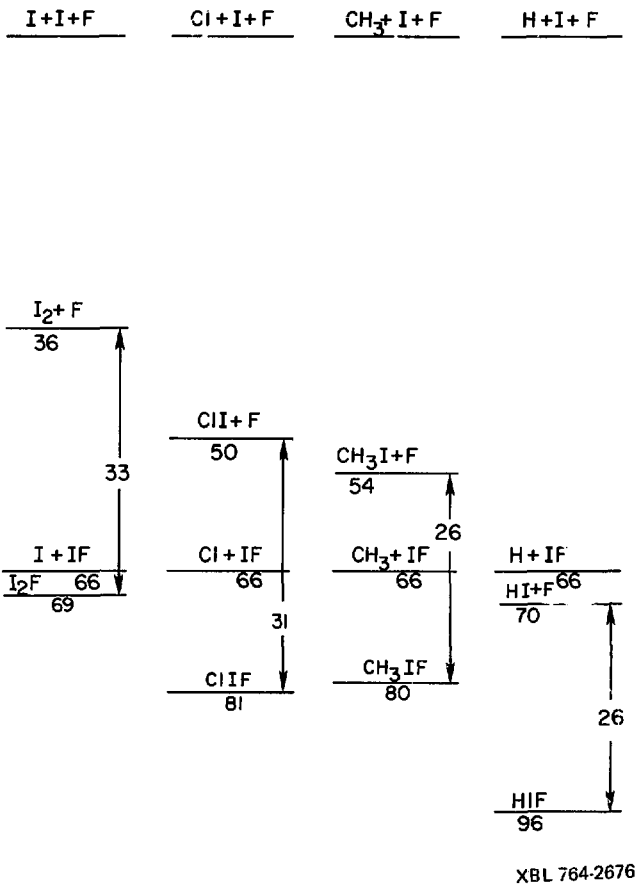

XBL 764-2676

Fig. 3

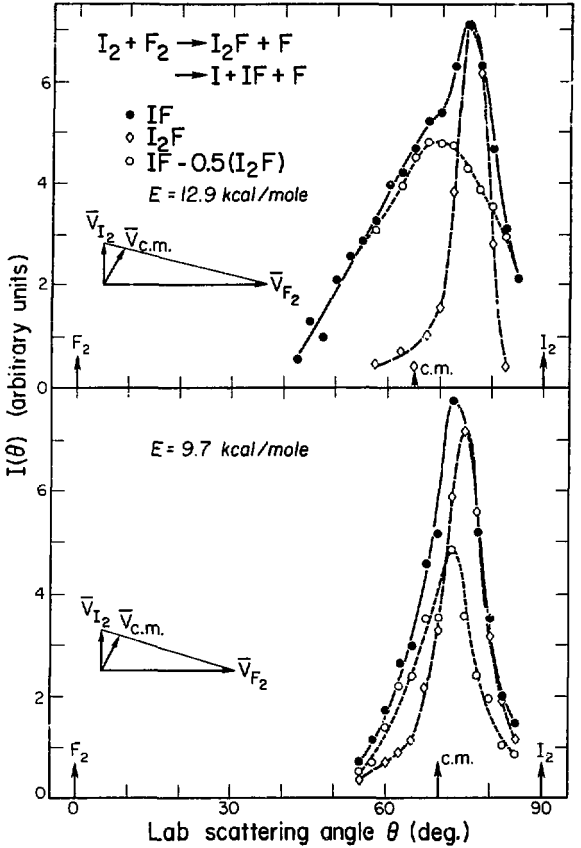

Figure 4

XBL 7510-8536

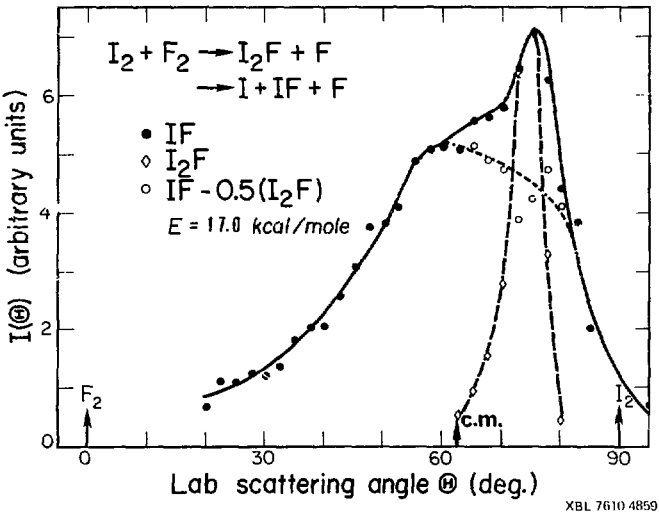
$I_2 + F_2 \rightarrow I_2F + F$
$\rightarrow I + IF + F$
IF
I_2F
IF - 0.5(I_2F)
E = 17.0 kcal/mole
I(Θ) (arbitrary units)
0
2
4
6
F_2
c.m.
I_2
0
30
60
90
Lab scattering angle Θ (deg.)
XBL 7610 4859

Fig. 5

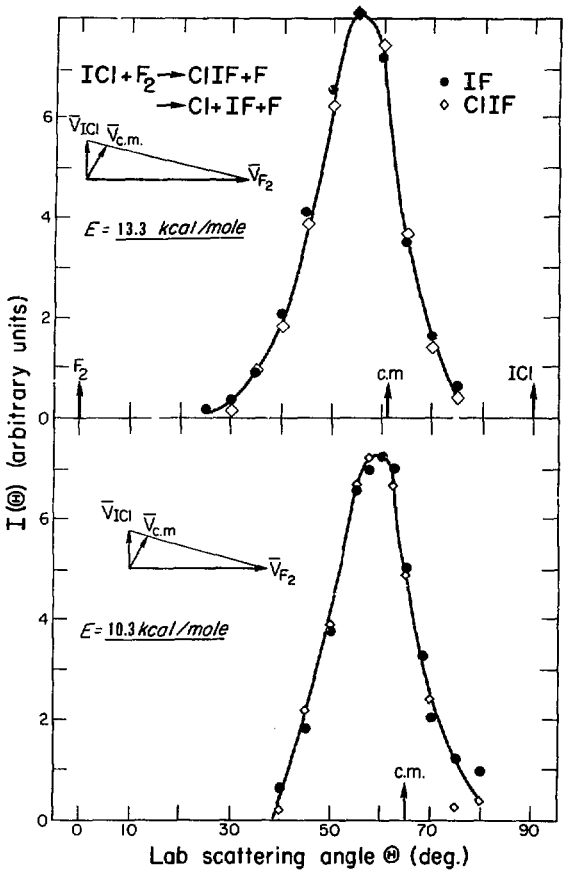
ICl + F2 → ClIF + F
→ Cl + IF + F
• IF
◇ ClIF
V̄ICl V̄c.m.
V̄F2
E = 13.3 kcal/mole
F2
c.m
ICl
E = 10.3 kcal/mole
I(Θ) (arbitrary units)
Lab scattering angle Θ (deg.)
0
10
30
50
70
90
XBL 7610-4960

Fig. 6

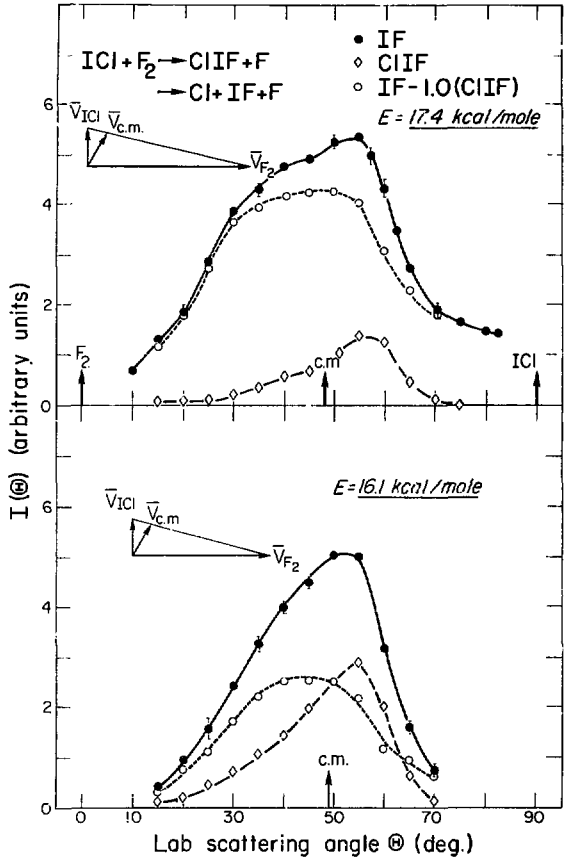

Fig. 7

XBL 764-2668

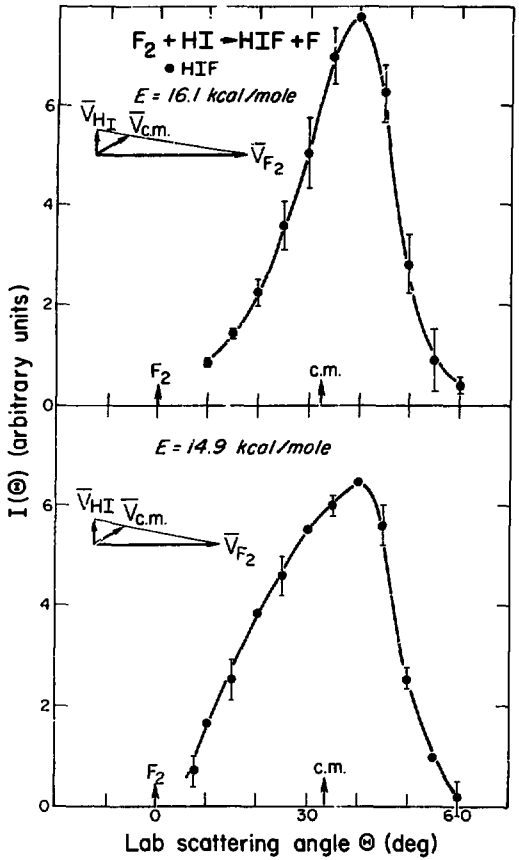

Fig. 8

XBL 764 2675

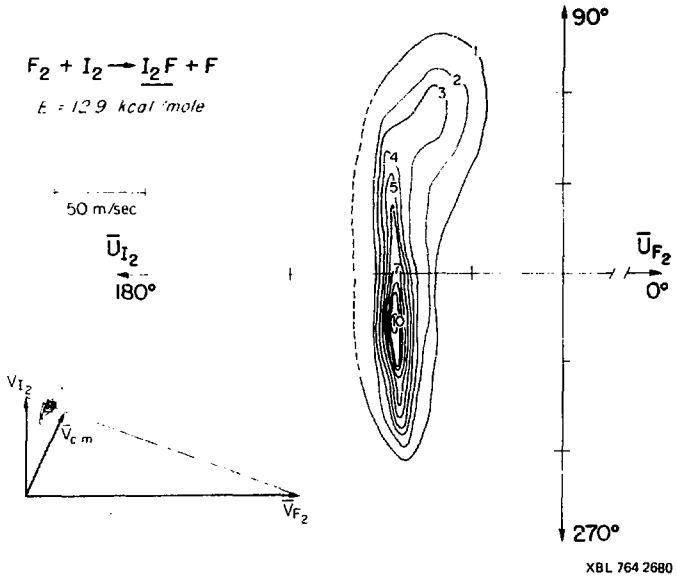
$F_2 + I_2 \rightarrow \underline{I_2}F + F$
E = 12.9 kcal/mole
50 m/sec
$\bar{U}_{I_2}$
180°
90°
$\bar{U}_{F_2}$
0°
270°
1
2
3
4
5
V_{I_2}
$\bar{V}_{c\,m}$
$\bar{V}_{F_2}$
XBL 764 2680

Fig. 9

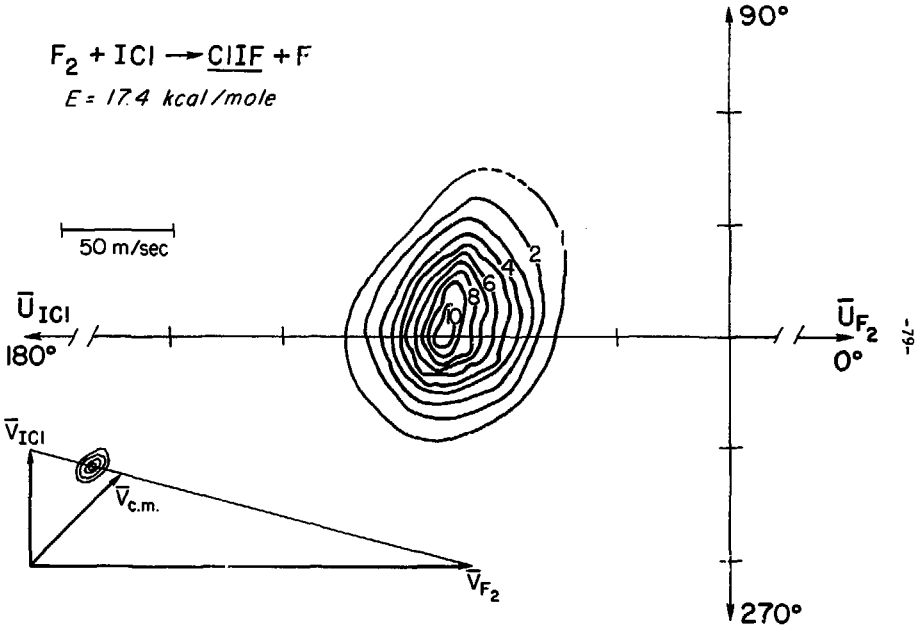

Fig. 10

XBL 764-2678

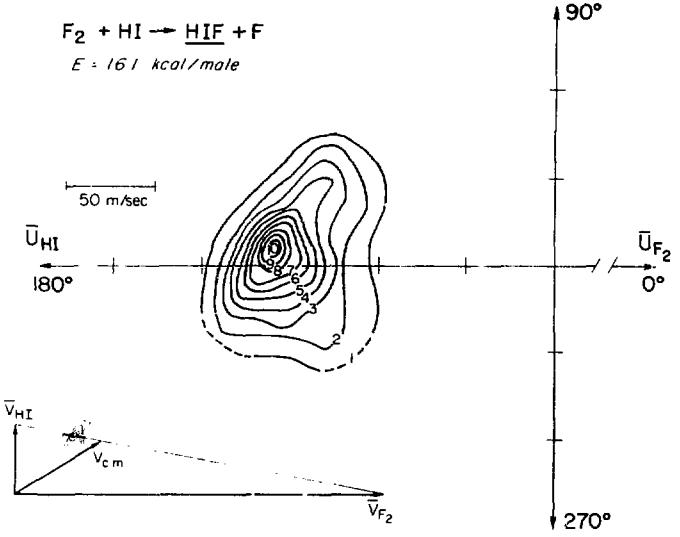

XBL 764-2681

Fig. 11

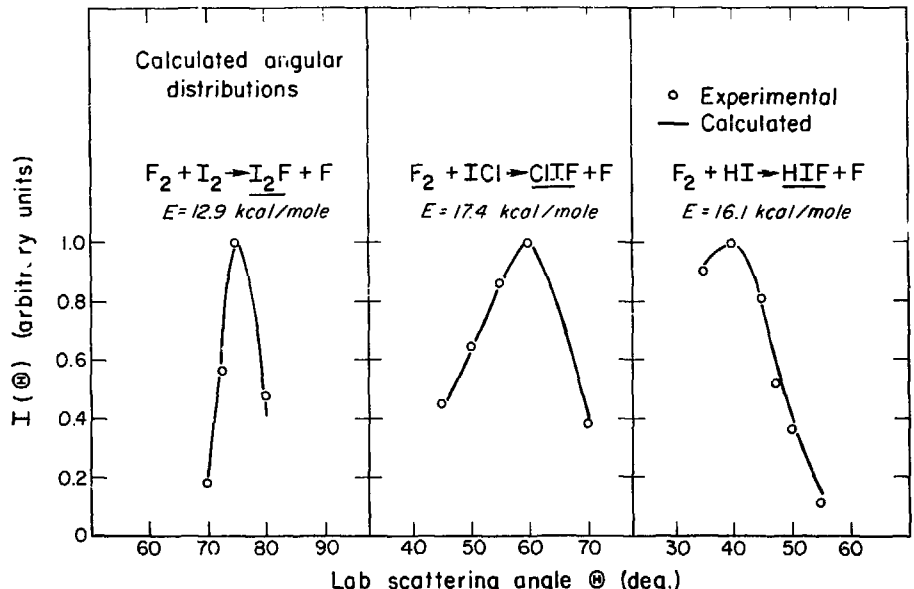

XBL 764-2677

Fig. 12

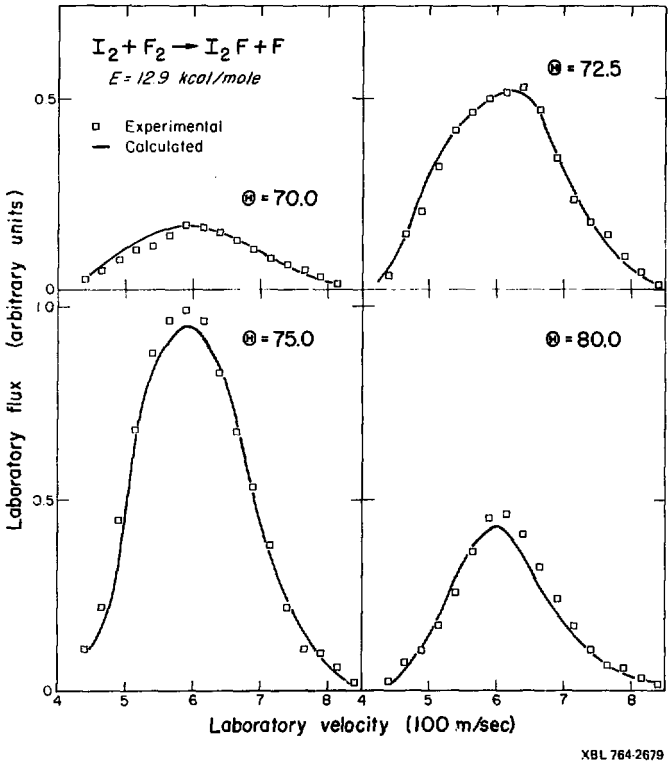
$I_2 + F_2 \rightarrow I_2F + F$
E = 12.9 kcal/mole
Experimental
Calculated
Θ = 70.0
Θ = 72.5
Θ = 75.0
Θ = 80.0
Laboratory flux (arbitrary units)
Laboratory velocity (100 m/sec)
0
0.5
1.0
4
5
6
7
8
XBL 764-2679

Fig. 13

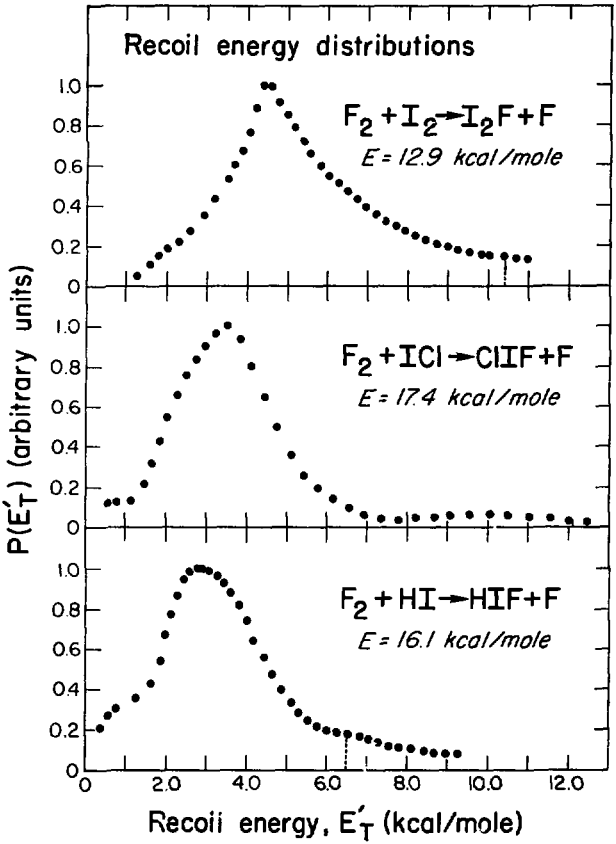

Fig. 14

XBL 764-2669

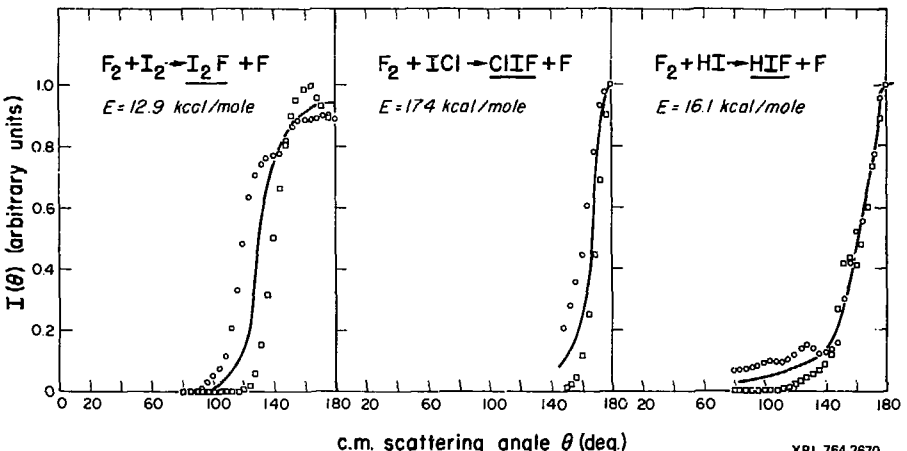
F2+I2→I2F+F
E=12.9 kcal/mole
F2+ICl→ClIF+F
E=17.4 kcal/mole
F2+HI→HIF+F
E=16.1 kcal/mole
I(θ) (arbitrary units)
0
0.2
0.4
0.6
0.8
1.0
0 20 60 100 140 180 20 60 100 140 180 20 60 100 140 180
c.m. scattering angle θ (deg.)
XBL 764-2670

Fig. 15

IV. THE Cl + Br_2 → BrCl + Br REACTION

A. Introduction

The atom-molecule exchange reactions of halogens are a considerably less complicated class of reactions than the molecule-molecule exchange reactions we have investigated. In the reaction, X + Y_2, only one reactive channel is possible, exchange to produce XY and Y. Despite the relative simplicity of these reactions, their dynamics are not well understood.

Reactions like

$$Cl + Br_2 \rightarrow BrCl + Br$$

$$Br + I_2 \rightarrow IBr + I$$

and the slightly more complicated

$$Cl + IBr \rightarrow ICl + Br$$

$$Cl + BrI \rightarrow BrCl + I$$

$$Br + ICl \rightarrow IBr + Cl$$

$$Br + ClI \rightarrow BrCl + I$$

have been studied in crossed molecular beam experiments by three different groups.[1-4] However, these early studies always employed molecular effusion sources to produce both the molecule and atom beams, with an attendant large spread in initial collision energy, and in most cases no velocity distribution data on the products was obtained. The conclusions that have been drawn, invoking possible complex formation, attractive potential energy surfaces with possible energy wells, and relatively small total cross sections, have as a result been mostly tentative. In the single case[2] in which velocity analysis was made,

the center-of-mass product distribution could not be very accurately recovered. A classical trajectory study of Br + I_2, Cl + I_2, and Cl + Br_2 using empirical surfaces having energy minima 0-10 kcal/deep with adjustable shapes and positions has been carried out by Borne and Bunker[5] in an attempt to explain the dynamics of these reactions. However, these authors found that no reasonable potential well for collinear reactant approach could explain the observed scattering.

A more complete crossed molecular beam study of one or more of these reactions with better defined initial conditions and product velocity analysis to allow complete unfolding of the center-of-mass distribution was obviously warranted. Investigation of these reactions at several collision energies in order to more completely probe the features of the X + Y_2 potential energy surface was also needed. For these reasons, we began a study of the Cl + Br_2 → BrCl + Br reaction using crossed beams of Cl and Br_2 produced from supersonic nozzles, to allow us to study the reaction as a function of collision energy under well-defined initial conditions.

B. Experimental

The crossed molecular beam apparatus used in studying this reaction is the same as that shown in Fig. 1 of Chapter III. Both the bromine molecule and chlorine atom beams were produced by supersonic nozzle sources. The same type glass nozzle source used to produce the I_2, ICl, and HI for the experiments of Chapter III was used here to generate

a bromine beam. The bromine was contained in a glass bulb immersed in a temperature regulated bath, held at 300 K. The glass gas feed line from the bulb to the nozzle and the nozzle itself were heated to prevent condensation of the bromine. This heating was provided by passing AC current through a heating "tape" wrapped around the feed line and nozzle. The nozzle temperature was monitored by a chromel: alumel thermocouple firmly attached to the nozzle tip. The nozzle temperature was maintained at about 360 K.

The chlorine atom beam was produced by the graphite nozzle source described in Chapter II. Mixtures of 10% Cl_2 in argon, 5% Cl_2 in helium, and 1% Cl_2 in helium were used as seeded gas mixtures for these experiments. These chlorine mixtures were obtained commerically. For these experiments the nozzle was operated with a nozzle tip temperature of about 1900 K, which gives an effective source temperature of about 1450 K (Cf. Fig. 11 of Chapter II). This gave collision energies of 6.8, 14.7, and 17.7 kcal/mole for the three gas mixtures used, with a spread in energy of ±35%.

Angular distribution measurements were made as for the F_2/XI reactions in Chapter III. These data were obtained using counting times of 60 to 120 seconds for each point, periodically returning to a reference angle to provide long-term normalization. Plotted angular distributions represent the average of several separate scans.

Product velocity distributions at selected angles were determined using a simple time-of-flight technique. These spectra of product intensity as a function of flight time were recorded using a 40 channel

multiscaler which had adjustable channel time width and delay time. For these measurements the BrCl product was modulated at the detector entrance aperture by a rotating, 17.8 cm diameter aluminum wheel with four slots of .30 cm width cut out at equally spaced points along the periphery. The wheel was rotated at a frequency of about 400 Hz. This gave a shutter function FWHM of about 13 μsec, about 7% time (velocity) resolution. Time-of-flight data were recorded for 60 to 180 minutes depending on the signal level.

C. Results

The angular distributions of the BrCl product at three different collision energies are shown in Figure 1. At all three collision energies the interhalogen product is quite strongly forward peaked, i.e., peaked toward the initial Cl atom velocity. As the collision energy is raised the product peaks more sharply in the forward direction. At the lowest collision energy some BrCl product does appear in the backward direction while at the higher collision energies the ClBr product is almost exclusively forward peaked.

From the angular distributions shown and from time-of-flight velocity analysis of the products, center-of-mass contour maps of product flux have been constructed. These are shown in Figs. 2, 3, and 4. These contour maps of $I_{c.m.}(\theta, u)$, the center of mass doubly differential reactive scattering cross section, were constructed by iterative deconvolution of the measured $\bar{I}_{LAB}(\theta, v)$ cross section data,

using computer program RECON described in Chapter V. The deconvolution procedure was identical to that used for recovering the center-of-mass distribution for the XIF products of the F_2 + XI reactions. However, since the Cl + Br_2 reaction does not appear to have a reaction energy barrier,[2,3] no energy weighting of the reactive cross section was used in recovering $I_{c.m.}(\theta, u)$.

The experimental data and laboratory data calculated from the deconvoluted center-of-mass flux distributions are compared in Figs. 5 and 6. The fit to the lab angular distributions and the velocity distributions at E_{COLL} = 14.7 kcal/mole are quite good. The fit to the velocity distributions at E_{COLL} = 6.8 kcal/mole are slightly better, while the fit to the velocity distributions at the highest collision energy is about the same as that at the intermediate collision energy shown.

The contour maps of Figs. 2, 3, and 4 show quite clearly that the BrCl product does peak almost exclusively in the forward hemisphere, even at the lowest collision energy. The BrCl which appears in the backward hemisphere in the lab angular distribution at a collision energy of 6.8 kcal/mole is mostly due to smearing of the lab angular distribution due to the range of Newton diagrams which effect the center-of-mass to lab transformation.

The contour maps show that the c.m. angular spread of the BrCl product does not change very much even when the collision energy increases from 6.8 kcal/mole to 17.7 kcal/mole. However, as the collision energy is increased the spread of the BrCl product in recoil

velocity decreases quite sharply. It is this decrease in range of recoil velocity that gives rise to the increased sharpness of the product lab angular distributions as the collision energy increases.

The change in the form of the recoil energy distribution is shown in detail in Figure 7. This figure gives plots of the relative intensity, $P(E_T'/E_{TOT})$, as a function of the fraction of the total available energy, E_{TOT}, which appears in translational energy of the products, E_T'. $P(f) = P(E_T'/E_{TOT}) = \sum_{\theta} I_{c.m.}(\theta, E_T') = \sum_{\theta} I_{c.m.}(\theta, u)/u$, where $I_{c.m.}(\theta, u)$ is the center-of-mass flux distribution as shown in Figs. 2, 3, or 4. These distributions show that when averaged over recoil angle, the recoil energy distributions do not peak at energies which are very different. In all cases the distributions peak at approximately .14 - .18, i.e., 14% - 18% of the total available energy. However, these recoil energy distributions do show a dramatic change as the collision energy is increased. At the lowest collision energy the recoil energy distribution is quite broad, extending to the maximal kinematic limit, $E_T'/E_{TOT} = 1$. As the collision energy is increased the recoil energy distribution becomes sharper, and the amount of product which appears with a large amount of translational energy decreases dramatically.

The fact that the recoil energy distribution for the lowest collision energy does not approach 0 at $E_T'/E_{TOT} = 1$ is a consequence of the imperfect deconvolution of the laboratory data. This means that the distribution probably decreases more sharply as $f \to 1.0$. For the higher collision energies the data are not plotted to f = 1.0, since the data are not

as accurate at high values of f. Clearly, however, there is negligible probability of having translational recoil energies of greater than about 60% of the total available energy.

The average product translational energy,

$$\overline{E_T'} = \frac{\sum_{E_T'} P(E_T') \cdot E_T'}{\sum_{E_T'} P(E_T')} ,$$

is, however, a considerably larger fraction of the total energy, ~38%, for the lowest collision energy, than for the higher collision energies, ~22%. This is of course due to the much greater range of recoil energies for the lowest collision energy than for the higher energies, even though the peak recoil energy is about the same fraction of the total energy for each case.

It is clear that the increased sharpness of the BrCl lab angular distributions at higher energy is a consequence of the narrower recoil energy (velocity) distributions at higher energies, and not an increasingly sharp center-of-mass angular distribution. As can be seen in Figure 8 the center-of-mass angular distributions, $I(\theta) = \sum_{E_T'} I_{c.m.}(\theta, E_T')$, are nearly identical at all three collision energies.

We have also made an attempt to determine the total reactive cross section, σ_R, for the Cl + Br_2 reaction at these collision energies. This was done by comparing the integrated intensity of reactive scattering to the observed intensity of small angle elastic scattering of chlorine atoms from bormine, which was normalized to the theoretical small angle elastic scattering intensity from theoretical van der Waals force constants.

The total cross section, in arbitrary units, is given by:

$$\sigma_R' = 2\pi \int_0^{\infty} \int_0^{\pi} \bar{I}_{c.m.}(\theta, u) \sin\theta \; d\theta \; du,$$

where $\bar{I}_{c.m.}(\theta, u)$ is derived from a single ("canonical") Newton diagram transformation of the measured $\bar{I}_{LAB}(\theta, v)$ data. This "canonical" Newton diagram was taken as the one which maximizes the quantity $(v_1^2 + v_2^2)\cdot f(v_1)\cdot f(v_2)\cdot f(\gamma)$, where $f(v_1)$, $f(v_2)$ are the velocity distribution functions of the two reactant beams and $f(\gamma)$ is the intersection angle distribution. This total cross section is related to the "true" total cross section by two constants, C_1 and C_2:

$$\sigma_R = \sigma_R' \cdot C_1 \cdot C_2 .$$

C_1 gives the ratio of detection efficiency for chlorine atoms (m = 35) to detection efficiency for BrCl (m = 116). C_2 gives the ratio of the theoretical small angle chlorine atom elastic scattering intensity in absolute units to the observed elastic scattering in arbitrary laboratory units.

The theoretical small angle elastic scattering intensity is given by:

$$I_{Cl}(\theta) = \frac{v}{u^2 \cos\delta} \cdot .239 \, (C_6/\bar{E})^{1/3} \, \theta^{-7/3},$$

where the first factor is the c.m. to lab transformation Jacobian, v and u are the lab and center of mass chlorine velocities, and δ is the angle between the $\bar{u}$ and $\bar{v}$ vectors. C_6 is the van der Waals constant and $\bar{E}$ is the most probable ("canonical") collision energy. C_6 was estimated to be 290×10^{-60} erg cm^6 using the combination rule[6]

$$C_{ab} = \frac{2C_{aa}C_{bb}}{[(\alpha_b/\alpha_a)C_{aa} + (\alpha_a/\alpha_b)C_{bb}]}$$

for C_6, and the Slater-Kirkwood approximation[7]

$$C_{ii} = 12.6 \times 10^{-60} \text{ erg-cm}^6 \, \alpha_i^2 \, (N_i/\alpha_i)^{1/2}$$

for C_{aa}, C_{bb}. Here α_a, α_b are the static dipole polarizabilities, in Å^3, of Cl and Br_2, and N_a, N_b are the number of electrons in the outer shells of Cl and Br_2, 7 and 14 respectively. The Cl and Br_2 polarizabilities, 2.2 Å^3 and 6.4 Å^3 respectively, were approximated from the values[8] for HX and H_2 by $\alpha(X) = \alpha(HX) - 1/2\alpha(H_2)$ and $\alpha(X_2) = 2\alpha(X)$.

The result of this calculation at collision energies of 6.8 kcal/mole and 14.7 kcal/mole gives $\sigma_R = 11$ Å^2 and $\sigma_R = 14$ Å^2 respectively. These numbers are probably only accurate to within a factor of three due to uncertainties attendant to the calculation of the total cross section in this manner.

D. Discussion

The fact that the center of mass angular distributions of the BrCl product are essentially identical and peaking sharply forward at collision energies of 6.8 kcal/mole, 14.7 kcal/mole, and 17.7 kcal/mole seems to indicate that the Cl + Br_2 interaction is an attractive one, without any appreciable activation energy or barrier. The lack of an energy barrier is also indicated by the fact that the total reactive cross section does not seem to be strongly dependent on the collision

energy. The total cross section at 14.7 kcal/mole (5-42 $\mathring{A}^2$) is nearly the same as that at 6.8 kcal/mole (4-33 $\mathring{A}^2$). If the reaction had an appreciable barrier, a few kcal/mole, the total reactive cross section should increase rather sharply as the collision energy increases from 6.8 kcal/mole to 14.7 kcal/mole, behavior similar to that observed for the F_2 + XI reactions. The magnitude of the total cross section determined here is not much different from that measured previously for the Cl + Br_2 reaction at even lower collision energy, ~3.0 kcal/mole. Here the cross section was estimated to be about 1 $\mathring{A}^2$ to 20 $\mathring{A}^2$.[2,3]

Thus, although the forward peaking of the ClBr product indicates that the dominant interaction between the reactants is attractive, the estimated total reactive cross sections are much smaller than hard sphere values. This might indicate that although the interaction is attractive it is short range in nature. Or it might mean that reaction may take place for a wide range of impact parameters, but with low probability. Such a situation could arise if the reaction demonstrated a stereochemical constraint, i.e, a strong preference for a particular Cl-Br-Br geometry. As discussed in reference to the F_2/XI reactions, the trihalogens may have a bent geometry. Thus the forward peaking and small cross sections may be due to a preference for a bent Cl-Br-Br geometry.

Although the center-of-mass angular distributions and reaction cross sections seem to show little or no variation as the collision energy is increased, the recoil energy distributions at the three collision energies studied show dramatic differences. These differences are

indicative of a change in the dynamics of the reaction as the collision energy increases.

The sharp recoil energy distribution at the highest collision energy, peaking a a small fraction (14%) of the total available energy, seems to indicate that the reaction is approaching the spectator stripping model. This highly simplified model assumes that the unreacting Br atom in Br_2 acts as a fully disinterested spectator of the reaction. When the internal energy of Br_2 is ignored, or is insignificant, as is the case when the Br_2 beam is produced by supersonic expansion, the spectator stripping model predicts all products to be scattered exactly forward in the c.m. system. This model also gives a unique recoil translational energy E_T', which is simply related by a mass factor to the collision energy E_{COLL}:

$$E_T' = \frac{m_{Cl}\, m_{Br}}{m_{Br_2}\, m_{BrCl}} E_{COLL} = .15\, E_{COLL} .$$

For E_{COLL} = 17.7 kcal/mole, E_T' = 2.7 kcal/mole, or 11% of the total available energy. The recoil energy distribution at E_{COLL} = 17.7 kcal/mole peaks at 14% of the total available energy, it is quite narrow, and is much closer to the spectator stripping limit than the recoil energy distributions at lower collision energy.

For E_{COLL} = 14.7 kcal/mole the recoil energy distribution is less sharp than at the highest collision energy, and peaks at 18% of E_{TOT}, while the spectator stripping model predicts a peak at 11%. Even so, this recoil energy distribution at 14.7 kcal/mole collision energy more closely resembles that at 17.7 kcal/mole collision energy than

that at 6.8 kcal/mole collision energy, as might be expected from the relative magnitudes of the collision energies. The recoil energy distribution at the intermediate energy represents a transition from the clearly nonstripping behavior at the lowest collision energy to the nearly stripping limit behavior at the highest collision energy.

The spectator stripping model assumes an impulsive collision in which Cl and a Br combine with negligible momentum transfer to the nonreacting Br atom of Br_2. The recoil energy distribution at the lowest collision energy clearly indicates substantial momentum transfer. This recoil energy distribution is quite similar to the recoil energy distribution obtained by LeBreton[9] at a mean collision energy of 5 kcal/mole.

Although the data obtained by LeBreton were never fully analyzed, it appears that an osculating complex model, assuming a complex lifetime of approximately one rotational period, and randomization of the total available energy into all accessible modes of the reaction intermediate, will fairly accurately reproduce his observed recoil energy and c.m. angular distributions. However, such an osculating complex model will probably not be able to give the sharply forward peaked distribution for BrCl observed in our work. It seems possible that the agreement between this osculating complex model and the measured data achieved in the earlier work might arise from the fact that the data were taken using effusive beams of chlorine and bromine and no deconvolution of the data to correct for the very large spread in initial conditions was performed. Our results would seem to indicate that if the Cl + Br_2

potential surface possesses an energy well, corresponding to a stable Cl-Br-Br complex, it must not be more than a few kcal/mole deep.

The results do however quite conclusively show that the Cl + Br_2 potential surface is an attractive one, giving forward peaking and a large fraction of the available energy in internal degrees of freedom, as expected for an exoergic reaction on an attractive surface with early energy release. The reaction dynamics will probably not be adequately explained by either a simple spectator stripping model or a simple osculating complex model, but it seems clear that as the collision energy is increased the reaction changes from a three body to more like a two body process.

It is also clear from the recoil energy distributions shown in Figure 7 that the reaction channels reagent translational energy into product internal energy with very high efficiency. At E_{COLL} = 6.8 kcal/mole the average internal energy is about 7.9 kcal/mole, while at collision energies of 14.7 kcal/mole and 17.7 kcal/mole this value increases to 16.2 kcal/mole and 18.4 kcal/mole. Thus one expects that the BrCl product will be highly vibrationally and rotationally excited.

It is possible that more than one electronic state is important in the dynamics of this reaction. The thermal dissociation chlorine atom source produces both the $^2P_{3/2}$ and $^2P_{1/2}$ (~15-20%) states of chlorine, and the reaction dynamics of these two states may be somewhat different. Since the spin orbit splitting in chlorine is 2 kcal/mole, these differences may only be important at low collision energies.

Airey, Pacey, and Polanyi[10] have detected Br ($^2P_{1/2}$) in infrared chemiluminescence studies, observing the excited electronic state in the H + HBr → H_2 + Br reaction. Since the spin-orbit splitting in bromine is quite large, about 8 kcal/mole, we should observe a bimodal recoil energy distribution if both the $^2P_{1/2}$ and $^2P_{3/2}$ states were produced in the Cl + Br_2 reaction. The recoil energy distributions do not give a clear indication that such is the case. However, if the BrCl internal energy distribution were different for the two Br states, such a bimodal distribution might be obscured.

E. References

1. D. Beck, F. Engelke, and H. J. Loesch, Ber. Bunsenges. Phys. Chem., 72, 1105 (1968).
2. N. C. Blais and J. B. Cross, J. Chem. Phys., 52, 3580 (1970).
3. Y. T. Lee, J. D. McDonald, P. R. LeBreton, and D. R. Herschbach, J. Chem. Phys., 49, 2447 (1968).
4. Y. T. Lee, P. R. LeBreton, J. D. McDonald, and D. R. Herschbach, J. Chem. Phys., 51, 455 (1969).
5. T. B. Borne and D. L. Bunker, J. Chem. Phys., 55, 4861 (1971).
6. H. L. Kramer and D. R. Herschbach, J. Chem. Phys., 53, 2792 (1970).
7. J. C. Slater and J. G. Kirkwood, Phys. Rev., 37, 682 (1931).
8. H. O. Hirschfelder, C. F. Curtiss, and R. B. Bird, Molecular Theory of Gases and Liquids (Wiley, New York, 1954), p. 950.
9. P. R. LeBreton, private communication.
10. J. R. Airey, P. D. Pacey, and J. C. Polanyi, Eleventh Symposium Combust., 85 (Combustion Inst., Pittsburgh, 1967).

FIGURE CAPTIONS

Fig. 1. Experimental laboratory angular distributions of BrCl produced in the reaction Cl + Br_2 at collision energies of 6.8 kcal/mole, 14.7 kcal/mole, and 17.7 kcal/mole.

Fig. 2. Contour map of BrCl flux density in the center-of-mass coordinate system produced in the reaction Cl + Br_2 at a collision energy of 6.8 kcal/mole.

Fig. 3. Contour map of BrCl flux density in the center-of-mass coordinate system produced in the reaction Cl + Br_2 at a collision energy of 14.7 kcal/mole.

Fig. 4. Contour map of BrCl flux density in the center-of-mass coordinate system produced in the reaction Cl + Br_2 at a collision energy of 17.7 kcal/mole.

Fig. 5. — Experimental laboratory angular distributions of BrCl produced in the Cl + Br_2 reaction at collision energies of 6.8 kcal/mole, 14.7 kcal/mole, and 17.7 kcal/mole; O laboratory angular distributions calculated by transforming $I_{c.m.}(\theta, u)$ (Figures 2-4) to the laboratory frame using a full range of Newton diagrams, and then summing over laboratory velocities.

Fig. 6. □ Experimental laboratory velocity distributions of BrCl produced in the Cl + Br_2 reaction at a collision energy of 14.7 kcal/mole at four laboratory angles; — laboratory velocity distributions derived from the center-of-mass product distribution shown in Figure 3.

Fig. 7. ● Product recoil energy distributions for the Cl + Br_2 reaction at collision energies of 6.8 kcal/mole, 14.7 kcal/mole, and 17.7 kcal/mole, as a function of the fraction of the total available energy, obtained by angle averaging $I_{c.m.}(\theta, E_T')$, see text.

Fig. 8. O Center-of-mass angular distributions of BrCl produced in the Cl + Br_2 reaction at collision energies of 6.8 kcal/mole, 14.7 kcal/mole, and 17.7 kcal/mole, obtained by averaging $I_{c.m.}(\theta, E_T')$ over recoil energy.

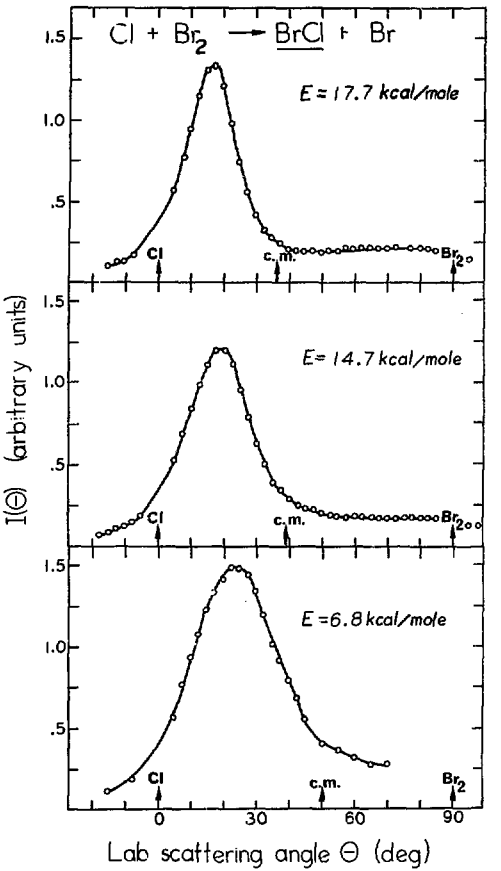

Fig. 1

XBL 7611-4782

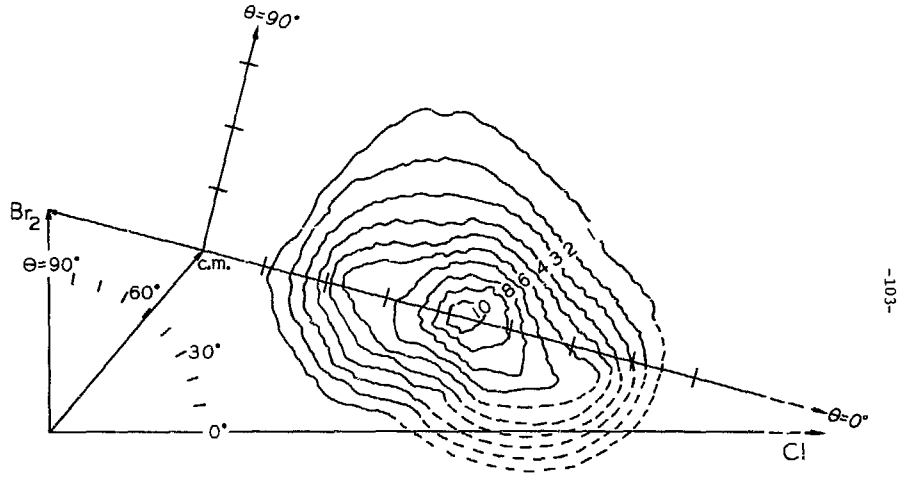
θ=90°
Br2
Θ=90°
c.m.
60°
30°
0°
θ=0°
Cl
2
4
6
8
10
Cl + Br2 → BrCl + Br
E = 6.8 kcal/mole
100 m/sec
XBL 7611-9716

Fig. 2

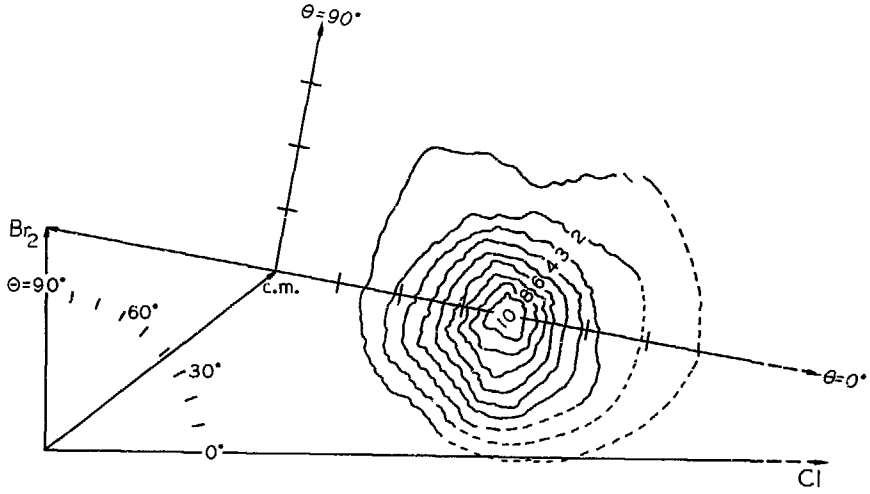
Θ=90°
Br2
Θ=90°
60°
30°
0°
c.m.
Θ=0°
Cl
Cl + Br2 → BrCl + Br
E = 14.7 kcal/mole
100 m/sec

Fig. 3

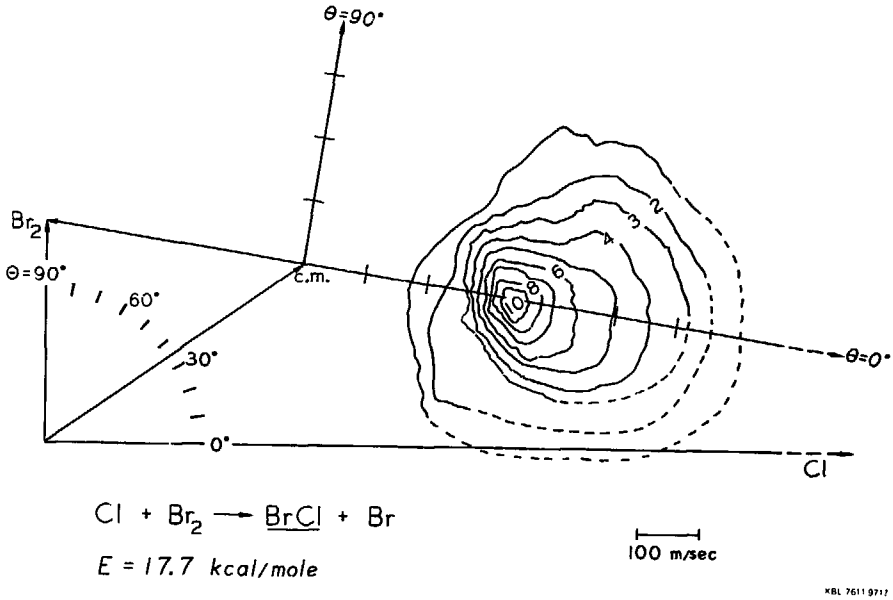
Θ=90°
Br2
Θ=90°
60°
30°
0°
c.m.
Θ=0°
Cl
2
3
4
6
8
0
Cl + Br2 → BrCl + Br
E = 17.7 kcal/mole
100 m/sec
KBL 7611 9717

Fig. 4

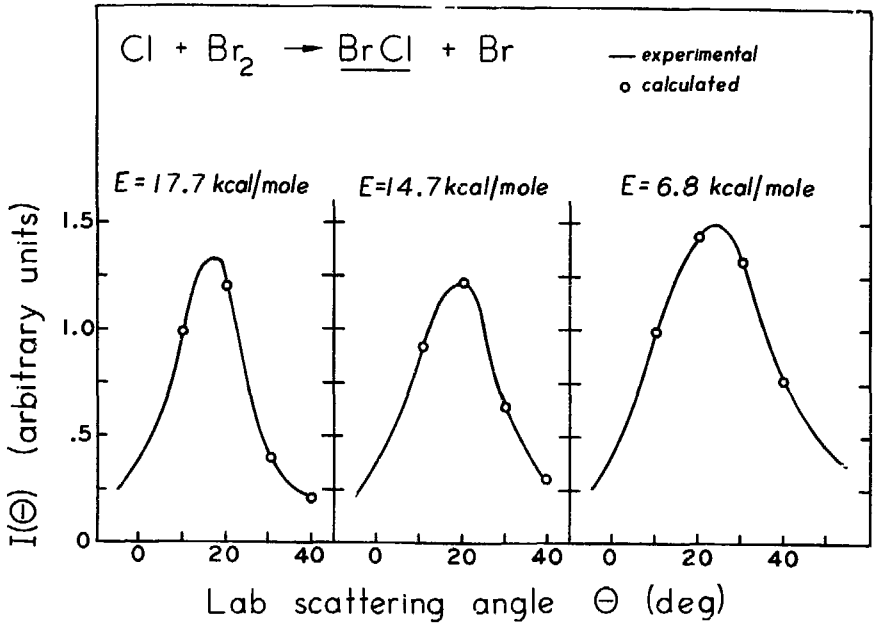

XBL 7611 4781

Fig. 5

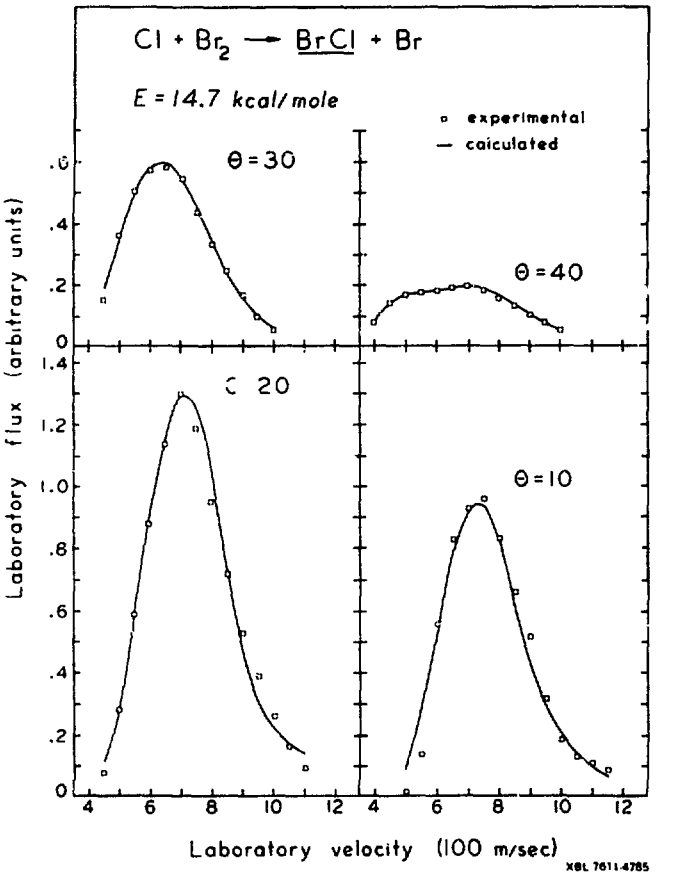
Cl + Br2 → BrCl + Br
E = 14.7 kcal/mole
experimental
calculated
Θ=30
Θ=40
Θ=20
Θ=10
Laboratory flux (arbitrary units)
Laboratory velocity (100 m/sec)
XBL 7611-4785

FIG. 6

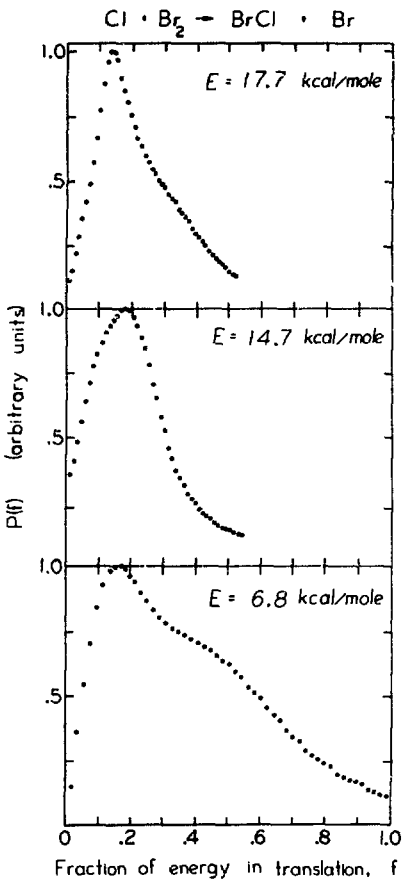
Cl + Br2 → BrCl + Br
E = 17.7 kcal/mole
E = 14.7 kcal/mole
E = 6.8 kcal/mole
P(f) (arbitrary units)
1.0
.5
0
.2
.4
.6
.8
1.0
Fraction of energy in translation, f
XBL 7611 4383

Fig. 7

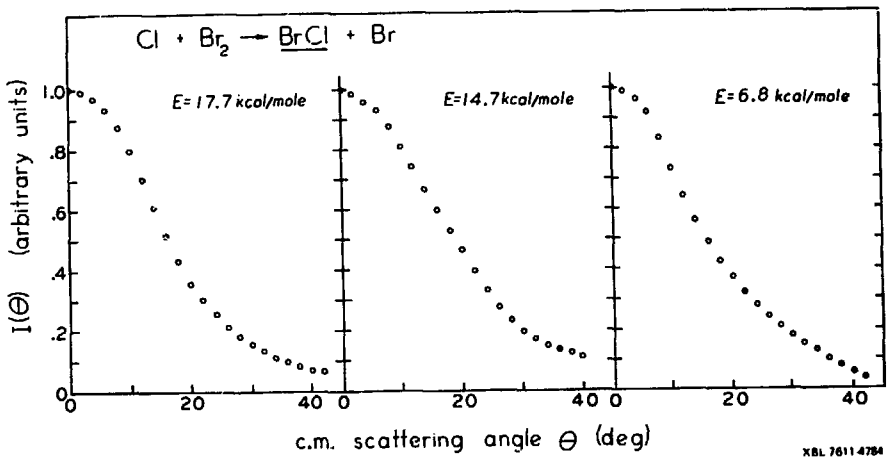
Cl + Br2 → BrCl + Br
E= 17.7 kcal/mole
E=14.7kcal/mole
E= 6.8 kcal/mole
I(Θ) (arbitrary units)
1.0
.8
.6
.4
.2
0
0
20
40
c.m. scattering angle Θ (deg)
XBL 7611-4784

Fig. 8

V. COMPUTER PROGRAMS FOR REACTIVE SCATTERING DATA ANALYSIS

A. Introduction

In crossed molecular beam experiments like those described in chapters III and IV, one normally measures two product distributions: an angular distribution, product intensity as a function of scattering angle, proportional to number density per unit angle; and a series of time-of-flight (TOF) distributions, product intensity as a function of product flight time, at selected scattering angles, proportional to number density per unit time per unit angle. These two distributions, represented by $\frac{dN_{LAB}(\Theta)}{d\Theta}$ and $\left.\frac{d^2N_{LAB}(\Theta, t)}{d\Theta dt}\right|_{\Theta_i}$, are not the desired representation of the results of a crossed molecular beam experiment.

In order to infer dynamical information from the experimental results one needs to construct the doubly differential cross-section in the center-of-mass (c.m) system, $\frac{d^2I_{c.m.}(\theta, u)}{d\theta du}$, where θ, u are the product scattering angle and velocity in the center-of-mass system. $\frac{d^2I_{c.m.}(\theta, u)}{d\theta du}$ has the dimensions of product flux (particles/cm^2-sec) per unit angle per unit velocity. This quantity, which for simplicity will be written $I_{c.m.}(\theta, u)$, is related to a similarly dimensioned quantity in the laboratory coordinate system, $I_{LAB}(\Theta, v) = \frac{d^2I_{LAB}(\Theta, v)}{d\Theta dv}$, by:

$$I_{LAB}(\Theta, v) = \frac{v^2}{u^2} I_{c.m.}(\theta, u), \qquad (1)$$

where Θ, and v are the laboratory scattering angle and velocity. The laboratory angle and velocity, Θ and v, are related to a c.m. angle and velocity, θ and u, by a simple coordinate transformation, given graphically by a so-called Newton diagram as shown in Figure 1. This

transformation is obviously dependent on the initial velocities of the two reactant beams and the angle of intersection between the two velocity vectors. Even for an experiment employing spatially well defined nozzle beams with narrow velocity distributions, a considerable range of reagent velocities and intersection angles are probable, hence the laboratory to center-of-mass transformation is not unique. Equation (1) should thus be written:

$$\bar{I}_{LAB}(\Theta, v) = \sum_i f_i(v_1, v_2, \gamma) \frac{v^2}{u_i^2} I_{c.m.}(\theta_i, u_i), \qquad (2)$$

where $f_i(v_1, v_2, \gamma)$, the weighting factor for the $i^{\underline{th}}$ Newton diagram, is a function of the reactant beam velocities, v_1, v_2, and intersection angle, γ, and the bar in $\bar{I}_{LAB}(\Theta, v)$ indicates that this is an averaged (over beam velocity and intersection angle) quantity. The functional form of f_i is dependent on the nature of the reaction which has been studied, but is generally

$$f_i = (v_1^2 + v_2^2)^{1/2} \cdot f(v_1) \cdot f(v_2) \cdot f(\gamma), \qquad (3)$$

where the $f(v_1)$ and $f(v_2)$ are the velocity distribution functions of the two reactant beams and $f(\gamma)$ is the distribution function for intersection angle, γ, and $(v_1^2 + v_2^2)^{1/2}$ is of course the relative velocity of the two reactants ($\gamma = 90°$). The recovery of $I_{c.m.}(\theta, u)$ from $\bar{I}_{LAB}(\Theta, v)$ is thus non-trival.

The construction of $I_{c.m.}(\theta, u)$ from the measured product angular distribution and TOF spectra thus separates into two parts: first, the construction of $\bar{I}_{LAB}(\Theta, v)$ from these distributions; and second, the solution of equation (2).

The first of these two parts is relatively straightforward. The several TOF distributions are normalized to one another so that:

$$\sum_t \left.\frac{d^2N_{LAB}(\theta,\ t)}{d\theta dt}\right|_{\theta_i} = \left.\frac{dN_{LAB}(\theta)}{d\theta}\right|_{\theta_i}, \tag{4}$$

i.e. so that the time integrated TOF spectra reproduce the angular distribution. This normalization yields the $\frac{d^2N_{LAB}(\theta,\ t)}{d\theta dt}$, which is related to $\bar{I}_{LAB}(\theta,\ v)$ by:

$$\bar{I}_{LAB}(\theta,\ v) = \frac{d^2I_{LAB}(\theta,\ v)}{d\theta dv} \cdot k \cdot v = \frac{d^2N_{LAB}(\theta,\ t)}{d\theta dt}, \tag{5}$$

where k is some proportionality constant. Since the measured data are not in absolute units, the factor k is set equal to 1.

Fitting programs, like program ANCON described later, which solve equation (2), generally require as input $\bar{I}_{LAB}(\theta,\ v)$ for several equally spaced values of v, while $\bar{I}_{LAB}(\theta,\ v)$ as obtained above consists of an array of intensities at unequally spaced velocities, corresponding to equally spaced values of the flight time, t. These fitting programs also require "smooth" input data for $\bar{I}_{LAB}(\theta,\ v)$ for efficient operation, while the measured data generally include substantial statistical fluctuations. Thus smoothing and interpolation of the data is needed to obtain $\bar{I}_{LAB}(\theta,\ v)$ in a usable form.

B. Program Flux

Although quite simple data smoothing and interpolation techniques are generally sufficient to obtain $\bar{I}_{LAB}(\theta,\ v)$, the volume of the data

handled necessitates the use of computer analysis. For this reason program FLUX has been written. FLUX has as its principal output the values of $\bar{I}_{LAB}(\theta, v)$ for $\theta = \theta_i$ and for $v = VO, VO + DV, VO + 2DV, \ldots, VO + (NV-1)DV$. These data are presented in the printed output as well as on punched cards in the proper format for input to the fitting program RECON. These data are derived from the input data, consisting of the observed TOF spectrum at angle $\theta = \theta_i$, an array of intensities (proportional to number density), N(n), versus channel number, n, as directly obtained from the output of a multichannel scaler which is used to record the TOF distribution. For this TOF spectrum

$$\left.\frac{d^2N_{LAB}(\theta, t)}{d\theta dt}\right|_{\theta_i} = \left. N(n)\right|_{\theta_i}, \qquad (6)$$

where $t = (n-.5)\cdot w$, for $n = n_1, n_2, \ldots n_f$ and w is the time of width of the scaler channels.

FLUX normalizes the data using equation (4) and calculates the spectrum of velocities, v, $v = l/t = l/(n-.5)\cdot w$, where l is the flight path length. FLUX then calculates the $\bar{I}(\theta, v)$ data from the input data $N(n)/_{\theta_i}$ using equation (5) and equation (6). FLUX first smoothes the $\bar{I}(\theta, v)$ data by averaging over a variable number of successive points, and then deconvolutes the smoothed $\bar{I}(\theta, v)$ data to remove any instrumental broadening inherent in the TOF apparatus.

From these deconvoluted $\bar{I}(\theta, v)$ data the values of $\bar{I}(\theta, v)$ for $v = VO, VO + DV, VO + 2DV, \ldots VO + (NV-1)DV$ are determined by interpolation. For any such value of v which is outside the range of

velocities spanned by the input data $\bar{I}(\theta, v)$ is set equal to zero. These interpolated $\bar{I}(\theta, v)$ data are renormalized so that:

$$\sum_{v} I(\theta)\cdot v \Big|_{\theta_i} = \sum_{t} \frac{d^2N_{LAB}(\theta, t)}{d\theta dt} \Big|_{\theta_i} = \frac{dN_{LAB}(\theta)}{d\theta} \Big|_{\theta_i} \qquad (7)$$

i.e., so that the interpolated $\bar{I}(\theta, v)$ data reproduce the measured angular distribution.

Also provided in the program are options for plotting the "measured" flux data, $\bar{I}(\theta, v)$, and the deconvoluted flux data together, and for plotting the "measured" flux data and the interpolated data, $\bar{I}(\theta, v)$, $v = V\theta$, $V0 + DV$, ... together. Time of flight data for different lab angles and even different experiments can be handled in one program execution by simply stacking the data for different TOF spectra.

A listing and sample output of program FLUX and a table defining the input variables follows.

Program FLeX Input Variables

Variable	Description
TITLE	heading for all printer and plotter output.
MASS	Mass of detected particle. MASS = 0.0 stops program execution.
THETA	Angle at which this TOF spectrum has been taken, reactant beams at 270° and 360°.
NORM	Normalization factor determined from the angular distribution. Ensures that the TOF spectra integrated over time have the same relative magnitudes as the angular distribution data. $\sum_t \left.\frac{d^2N_{LAB}(\Theta, t)}{d\Theta dt}\right\|_{\Theta_i} \cdot \text{WIDTH} = \text{NORM} \cdot 10^5$, where WIDTH is as given below.
DC	Magnitude of the constant background to be subtracted from the data in each channel.
ICONT	Number of different TOF spectra taken at angle THETA. Allows combining data taken in different scans.
OFFSET	The time, in units of multiscaler channel width, by which the multiscaler zero of time lags behind the true zero of time. The value of this parameter is determined by calibration of the TOF apparatus. This parameter corrects the $\frac{d^2N_{LAB}(\Theta, t')}{d\Theta dt'}$ data, where t' is the observed flight time, to give the $\frac{d^2N_{LAB}(\Theta, t)}{d\Theta dt}$ where t is the true flight time. t = t' + OFFSET·WIDTH, where WIDTH is as given below.
EION, LION	Ion energy, in electron volts, and ion flight path, in centimeters. Needed to correct product flight times for the time required for the ions to traverse the length, LION, of the detector.

Program FLUX Input Variables (Cont'd)

Variable	Description
DIST	TOF flight path length in centimeters.
DL	Ionizer length in centimeters.
WIDTH	Time width, in microseconds, of the multiscaler channel.
BCHAN, ECHAN	Number of the first and last multiscaler channels for which data are to be input.
ACHAN	Number of channels (always odd) over which the data is averaged for smoothing.
VO	First velocity, in units of 10^4 cm/sec, for which punched output for RECON is desired.
DV	Velocity interval, in units of 10^4 cm/sec, for which punched output for RECON is desired. If DV = 0.0 no data is output on punched cards.
NV	Number of velocities for which punched output for RECON is desired.
NPL1, NPL2	Plotter option. If NPL1 = 0 and NPL2 = 0 no plots are generated. If NPL1 $\neq$ 0 measured flux data (points) and deconvoluted flux data (line) are plotted. If NPL2 $\neq$ 0 the interpolated flux for input to RECON (line and the measured flux (points) are plotted.
SIGNAL (I), I = BCHAN, ECHAN	Observed TOF intensity in channel I.

```
      PROGRAM FLUX (INPUT,OUTPUT,PUNCH,TAPE5=INPUT,TAPE6=OUTPUT,TAPE7=PU
     1NCH,TAPE98=101,PLOT,TAPE99=PLOT)
      DIMENSION VEL(255),FLUXE(255),FLUXS(255),FLUXC(255),LABINT(255),PE
     1(255),X(9),W(9),XLAB(3),YLAB(3),TITLE(5),VP(255),SIGNAL(255),VT(25
     15),PZ(255)
      REAL NORM,LABINT,LION,MASS,LAST,L
      INTEGER BCHAN,ECHAN,ACHAN
C     DEFINE LABELS FOR PLOTS
      XLAB(1)=10H      VELOC
      XLAB(2)=10HITY (1000
      XLAB(3)=10H CM/SEC)
      YLAB(1)=10H      FLUX
      YLAB(2)=10HARBITRARY
      YLAB(3)=10HUNITS
      CALL GAUSS(X,W)
C     INPUT DATA
   10 READ(5,100) TITLE
      READ(5,110) MASS
      IF(MASS .EQ. 0.0) GO TO 1111
  100 FORMAT(6A10)
  110 FORMAT(5F10.3)
      WRITE(6,200) TITLE
  200 FORMAT(1H1,6A10)
      READ(5,101) THETA,NORM,DC,ICONT
  101 FORMAT(3F10.3,I5)
      READ(5,110) OFFSET,EION,LION,DIST,DL
      READ(5-120) WIDTH,BCHAN,ECHAN,ACHAN
  120 FORMAT(F10.3,3I5)
      READ(5,111) V0,DV,NV,NPL1,NPL2
  111 FORMAT(2F10.3,3I5)
C     CORRECT FLIGHT TIMES FOR ION TRANSIT TIME
      CHT=LION/SQRT(EION/MASS)*.7199/WIDTH
      ICHT=INT(OFFSET-CHT+SIGN(.5,OFFSET-CHT))
      BCHAN=BCHAN+ICHT
      ECHAN=ECHAN+ICHT
      NCHAN=ECHAN-BCHAN+1
      VF=DIST*100./((BCHAN-.5)*WIDTH)
      VI=DIST*100./((ECHAN-.5)*WIDTH)
      DO 11 I=1,NCHAN
    1 LABINT(I)=0.0
      SUM=0.
C     READ INTENSITIES FOR ICONT NUMBER OF TOF SPECTRA
      DO 22 J=1,ICONT
      READ(5,999) (SIGNAL(I), I=1,NCHAN)
      DO 20 I=1,NCHAN
      IF(SIGNAL(I) .LT. 0.0) SIGNAL(I)=(SIGNAL(I-1) + SIGNAL(I+1))/2.
      LABINT(I)=LABINT(I)+SIGNAL(I)
      SUM=SUM+ SIGNAL(I)
   20 CONTINUE
   22 CONTINUE
  999 FORMAT(8F10.3)
      SUM=SUM-DC*NCHAN
      SKIP=SUM/NORM/100000.*WIDTH
C     CALCULATE VELOCITIES, SUBTRACT CONSTANT BACKGROUND FROM THE DATA,
C     AND CALCULATE THE FLUX FROM THE NUMBER DENSITY
      DO 23 I=1,NCHAN
      VEL(I)=DIST*100./((I-1.5+BCHAN)*WIDTH)
      LABINT(I)=LABINT(I)-DC
      FLUXE(I)=LABINT(I)/VEL(I)/SKIP
      FLUXC(I)=FLUXE(I)
      FLUXS(I)=FLUXE(I)
```

```
   23 CONTINUE
C      AVERAGE DATA OVER THE SELECTED NUMBER OF CHANNELS
       INC=ACHAN/2
       IED=NCHAN-ACHAN
       DO 30 I=1,IED
       RUN=0.
       DO 35 J=1,ACHAN
       RUN=RUN + FLUXE(I+J-1)
   35 CONTINUE
       FLUXS(I+INC)=RUN/FLOAT(ACHAN)
       FLUXC(I+INC)=FLUXS(I+INC)
   30 CONTINUE
C      DECONVOLUTION OF FLUX DATA
       ERR=100.
       IT=1
   40 IT=IT+1
       LAST=ERR
       ERR=0.
       DO 45 I=3,NCHAN-2
       SUM 45=0.
       DO 50 J=1,9
       SUM 50=0.
       T=WIDTH*(X(J)/2.-1.5+I+BCHAN)
       DO 55 K=1,9
       Y=0.0
       L=DIST+DL*X(K)/2.
       V=L/T*100.
       IF(V .GT. VF .OR. V .LT. VI) GO TO 55
       Y=YNTERP(VEL,FLUXC,V,NCHAN,3)
   55 SUM 50= SUM 50 + Y*W(K)/2.
   50 SUM45=SUM45+SUM50*W(J)/2.
       FLUXC(I)=SUM45
       ERR=ERR+(FLUXC(I)-FLUXS(I))**2
       IF(FLUXC(I).LT. 0.0) FLUXC(I)=FLUXS(I)
       FLUXC(I)=FLUXC(I)*FLUXS(I)/FLUXC(I)
   45 CONTINUE
       ERR=SQRT(NCHAN*ERR)/SUM
       IF(((LAST-ERR)/LAST .GT. .05) .AND. (IT .LT. 5)) GO TO 40
       IF(NPL1 .EQ. 0) GO TO 209
       CALL PLOT(1,1,2,NCHAN,VEL,FLUXE,XLAB,YLAB,TITLE)
       CALL PLOT(1,2,1,NCHAN,VEL,FLUXC,XLAB,YLAB,TITLE)
       CALL CONEXT
  209 WRITE(6,210)
  210 FORMAT(1HO*   MASS       ANGLE        NORM    BACKGROUND*)
       WRITE(6,211) MASS,THETA,NORM,OC
  211 FORMAT(3F10.3,2X,F10.3)
       WRITE(6,220)
  220 FORMAT(1HO*ZERO CHANNEL OFFSET   NET OFFSET   FLIGHT PATH   IONIZE
      1R LENGTH*)
       WRITE(6,230) OFFSET,ICHT,DIST,DL
  230 FORMAT(2X,F10.3,11X,I5,7X,F10.3,6X,F10.3)
       WRITE(6,240)
  240 FORMAT(1HO*CHANNEL WIDTH   FIRST CHANNEL   LAST CHANNEL   NO. CHAN
      1. AVERAGED*)
       WRITE(6,250) WIDTH,BCHAN=ICHT,ECHAN=ICHT,ACHAN
  250 FORMAT(F10.3,9X,I5,10X,I5,14X,I5)
       WRITE(6,260)
  260 FORMAT(1HO*CHANNEL      VELOCITY          LAB NO. DENSITY     LAB FLU
      1X     SMOOTHED LAB FLUX    DECONVOLUTED LAB FLUX*)
       DO 70 I=1,NCHAN
   70 WRITE(6,270) I+BCHAN-1,VEL(I),LABINT(I),FLUXE(I),FLUXS(I),FLUXC(I)
  270 FORMAT(15,9X,F5.2,10X,F10.2,7X,F10.2,6X,F10.2,14X,F10.2)
```

```
      IF(DV .EQ. 0.) GO TO 10
      WRITE(6,320) V0,DV
  320 FORMAT(1H0* INPUT FOR RECON    V0 = *,F5.2,*  DV = *,F4.2)
      WRITE(6,330)
  330 FORMAT(1H0*   VELOCITY          FLUX         RENORM. FLUX*)
      ISTART=0
      ISTOP=NV
C     CALCULATE EVENLY SPACED VELOCITIES AS REQUESTED
      DO 90 I=1,NV
      PE(I)=0.0
      VT(I)=V0+FLOAT(I-1)*DV
      V=VT(I)
      IF(ISTART .NE. 0) GO TO 91
      IF(V .LT. VI) GO TO 90
      ISTART=I
   91 IF((ISTOP .NE. NV) GO TO 90
      IF(V .GT. VF) ISTOP=I-1
   90 CONTINUE
      SUP=0.0
C     CALCULATE THE FLUX AT THESE EQUALLY SPACED VELOCITIES
      DO 80 J=ISTART,ISTOP
      I=J-ISTART+1
      VP(I)=VT(J)
      PE(J)=YNTERP(VEL,FLUXC,VT(J),NCHAN,3)
      IF(PE(J)) 79,81,81
   79 PE(J)=0.
   81 PZ(I)=PE(J)
   80 SUP=SUP+PE(J)/VT(J)
      SKIP=DV*SUP*DIST/NORM/1000.
      WRITE(6,300) (VT(J),PE(J),PE(J)/SKIP, J=1,NV)
  300 FORMAT(4X,F5.2,7X,F10.2,8X,F10.2)
      WRITE(7,290) THETA-270.
  290 FORMAT(5X,F6.1)
      WRITE(7,310) (PE(I)/SKIP,I=1,NV)
  310 FORMAT(8F10.2)
      IF(NPL2 .EQ. 0) GO TO 10
      NV=ISTOP-ISTART+1
      CALL PLOT(1.1.2,NCHAN,VEL,FLUXE,XLAB,YLAB,TITLE)
      CALL PLOT(1,2.1,NV,VP,PZ,XLAB,YLAB,TITLE)
      CALL CCNEXT
      GO TO 10
 1111 IF((NPL1 .EQ. 3) .AND. (NPL2 .EQ. 3)) STOP
      CALL CCEND
      STOP
      END
      SUBROUTINE GAUSS(X,W)
      DIMENSION X(9),W(9)
      X(5)=0.0
      X(6)=.32425
      X(7)=.61337
      X(8)=.83603
      X(9)=.96816
      W(5)=.33024
      W(6)=.31235
      W(7)=.26061
      W(8)=.18065
      W(9)=.08126
      DO 1 I=1,4
      J=10-I
      X(I)=-X(J)
      W(I)=W(J)
    1 CONTINUE
```

```
      RETURN
      END
      FUNCTION YNTERP(XA,YA,X,L,N)
C     ROUTINE FOR INTERPOLATION OF THE FLUX
      DIMENSION XA(1),YA(1),ZA(21)
      COMMON/YNTCOM/IFD
      DATA SG1/0.0/
      IF(SG1 .NE. 0.0) GO TO 12
      SG1=1.0
      IFD=0
   12 SG2=0
      IU=L+1
      IF(L .LT. 2) GO TO 43
      NIN=N
      IF(N .LT. 1 .OR. N .GT. 20) GO TO 40
      NP1=N+1
      IF(NP1-L) 14,48,43
   14 IF(XA(L)-XA(1)) 16,43,18
   16 SG2=1.0
      IL=IU
      IU=0
      GO TO 20
   18 IL=0
   20 IA=(IU+IL)/2
      IF(IABS(IU-IL) .LT. 3) GO TO 26
      IF(X-XA(IA)) 22,46,24
   22 IU=IA
      GO TO 20
   24 IL=IA
      GO TO 20
   26 IF(X .EQ. XA(IA)) GO TO 46
      IFD=IA
      IA=IA-NP1/2
      IF(MOD(NIN,2) .EQ. 0) GO TO 30
      IF(X .GT. XA(IFD)) GO TO 28
      IF(SG2 .NE. 0.0) IA=IA+1
      GO TO 30
   28 IF(SG2 .EQ. 0.0) IA=IA+1
   30 IF(IA .LT. 1) IA=1
      IF(L-NIN .LT. IA) IA=L-NIN
   32 JA=IA
      DO 34 J=1,NP1
      ZA(J)=YA(JA)
   34 JA=JA+1
      IB=IA
      DO 38 I=1,NIN
      T1=X-XA(IB)
      DO 36 J=I,NIN
      JA=J+IA
      T2=XA(JA)-XA(IB)
   36 ZA(J+1)=ZA(I)+T1*(ZA(J+1)-ZA(I))/T2
   38 IB=IB+1
      YNTERP=ZA(NIN+1)
      RETURN
   40 WRITE(6,42)
   42 FORMAT(1HJ,* ERROR RETURN FROM YNTERP, N IS OUT OF RANGE.*)
   43 IFD=1
      YNTERP=YA(1)
      RETURN
   46 YNTERP=YA(IA)
      IFD=IA
      RETURN
```

```
48 IA=1
   IFD=1
   GO TO 32
   END
   SUBROUTINE PLOT(IOSV,NCONT,NCURVE,NP,X,Y,XLAB,YLAB,TITLE)
   COMMON /CCPOOL/ XMIN,XMAX,YMIN,YMAX,CCXMIN,CCXMAX,CCYMIN,
  1 CCYMAX
   COMMON /CCFACT/ FACTOR
   DIMENSION X(1),Y(1),ROUND(4)
   DATA NROUND /4/
   DATA (ROUND(I),I=1,4) / 1.,2.,2.5,5. /
   FACTOR=100.
   CCXMIN=1.$CCXMAX=8.$CCYMIN=1.$CCYMAX=10.5
   IF(NCONT.EQ.2) GO TO 10
   CALL LINEUP (X,NP,ROUND,NROUND,10.,XMIN,XMAX)
   CALL LINEUP(Y,NP,ROUND,NROUND,10.,YMIN,YMAX)
   CALL CCGRID(1,1,1,6HNOLBLS,1,10,1)
   CALL CCLBL(10,1)
   CALL CCLTR(1.5,10.7,0.1,TITLE,60)
   CALL CCLTR(3.5,.1,0,1,XLAB,30)
   CALL CCLTR(.1.5,.1,1,YLAB,30)
10 CONTINUE
   IF(NCURVE.EQ.2) GO TO 20
   CALL CCPLOT(X,Y,NP)
   GO TO 30
20 CALL CCPLOT (X,Y,NP,6HNOJOIN,65,1)
30 RETURN
   END
```

71174-34 ARCL PRODUCT

MASS	ANGLE	NORM	BACKGROUND
816.000	280.000	.940	0

ZERO CHANNEL OFFSET	NET OFFSET	FLIGHT PATH	IONIZER LENGTH
.650	-1	17.360	2.500

CHANNEL WIDTH	FIRST CHANNEL	LAST CHANNEL	NO. CHAN. AVERAGED
15.333	14	24	3

CHANNEL	VELOCITY	RAW AC. DENSITY	LAB FLUX	SMOOTHED LAB FLUX	DECONVOLUTED LAB FLUX
9	19.17	140.00	4.21	4.21	4.21
10	12.14	1208.00	40.62	38.65	38.65
11	10.98	2126.00	73.73	68.06	68.06
12	13.03	2370.00	90.02	89.97	89.97
13	9.23	2571.00	106.15	98.96	98.96
14	6.54	2324.00	103.63	94.72	94.72
15	7.95	1593.00	76.38	82.60	82.60
16	7.44	1383.00	69.78	69.44	69.44
17	5.49	951.00	52.16	56.48	56.48
18	6.59	827.00	47.51	45.38	45.38
19	6.23	597.00	36.48	32.91	32.91
20	5.91	229.00	14.75	19.33	19.33
21	1.61	100.00	6.77	7.17	7.17
22	5.30	0	0	0	0
23	4.13	0	0	0	0

INPUT FOR REGIN VO = 4.50 DV = .50

VELOCITY	FLUX	RETURN, FLUX
4.50	0	0
4.09	0	0
4.53	3.31	3.07
6.00	23.96	23.54
6.50	42.99	43.37
7.00	96.70	97.91
7.50	97.27	96.71
8.00	83.82	85.62
8.50	96.09	96.11
9.00	99.43	101.57
9.50	98.07	100.17
10.00	90.51	92.48
10.50	89.32	91.74
11.00	87.04	89.13
11.50	55.46	56.65
12.00	42.98	43.90
12.50	30.43	31.08
13.00	17.99	18.37
13.50	5.84	5.97
14.00	0	0

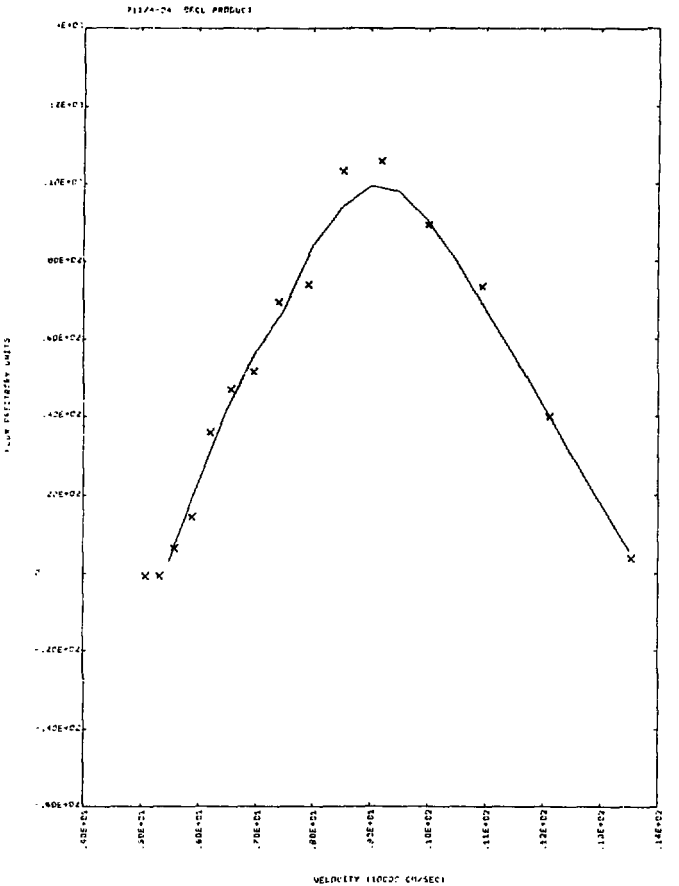
VELOCITY (LOG CM/SEC)

C. Program Recon

One commonly used method for determining $I_{c.m.}(\theta, u)$ once $\bar{I}_{LAB}(\theta, v)$ has been constructed consists of assuming some functional form for $I_{c.m.}(\theta, u)$ and then varying the parameters of this functionality until $I_{c.m.}(\theta, u)$ reproduces $\bar{I}_{LAB}(\theta, v)$ by means of equation (2).[1,2] This method usually describes $I_{c.m.}(\theta, u)$ by a truncated degenerate expansion:

$$I_{c.m.}(\theta, u) = \sum_{i=1}^{m} \sum_{j=1}^{n} a_{ij} T_i(\theta) U_j(u) \qquad (8)$$

where the T and U functions may for instance be polynomials of degree i-1 or j-1. The a_{ij} are then the parameters to be determined. Since the number of data points is usually much greater than the number (typically 20 to 40) of a_{ij}, these parameters are overdetermined and least squares techniques are used to determine them.

Problems can arise using such algebraic techniques for solving for $I_{c.m.}(\theta, u)$. More flexibility than is provided by degenerate expansions of typical size may be needed to accurately determine $I_{c.m.}(\theta, u)$, especially if the data are highly structured. This technique also becomes difficult to use if the data do not admit separability of $I_{c.m.}(\theta, u)$ into independent θ and u dependences. Also, the actual $I_{c.m.}(\theta, u)$ determined by these techniques may be sensitive to the choice of the expansion functions.

An alternative procedure which avoids these problems is to use iterative techniques to determine $I_{c.m.}(\theta, u)$. Instead of generating a functional representation of $I_{c.m.}(\theta, u)$, the measured $\bar{I}_{LAB}(\theta, v)$

data can be used to generate iterative successive approximations to $I_{c.m.}(\theta, u)$ using equation (2). If one assumes that $I_{c.m.}(\theta, u)$ is related to a "monochromatic," i.e. unaveraged, $I_{LAB}(\theta, v)$ by a single "canonical" Newton diagram:

$$I_{LAB}(\theta, v) = \frac{v^2}{u^2} I_{c.m.}(\theta, u), \tag{9}$$

equation (2) becomes:

$$\bar{I}_{LAB}(\theta, v) = \sum_i f_i \frac{v^2}{v_i} I_{LAB}(\theta_i, v_i). \tag{10}$$

This "canonical" Newton diagram is the most probable Newton diagram, that is, the Newton diagram which maximizes f_i.

One can then use various methods to provide an initial guess and successive approximations for $I_{LAB}(\theta, v)$ using the $\bar{I}_{LAB}(\theta, v)$ data. One such method, developed by Siska,[3] uses a ratio method to generate successive approximations for $I_{LAB}(\theta, v)$, using the experimental data, $\bar{I}^{EXPT}_{LAB}(\theta, v)$, to give the initial guess:

$$I^{(0)}_{LAB} = \bar{I}^{EXPT}_{LAB} \tag{11}$$

$$I^{(n+1)}_{LAB} = I^{(n)}_{LAB} \cdot (\bar{I}^{EXPT}_{LAB}/\bar{I}^{(n)}_{LAB}). \tag{12}$$

This method assumes that the ratio of $\bar{I}^{EXPT}_{LAB}$ to $\bar{I}^{(n)}_{LAB}$ is representative of the error in I_{LAB}. The iteration is repeated until this error in I_{LAB} is minimized, that is, until $\bar{I}^{EXPT}_{LAB}/\bar{I}^{(n)}_{LAB} \simeq 1$. When this best fit $I_{LAB}(\theta, v)$ distribution is obtained $I_{c.m.}(\theta, u)$ is generated by means of equation (9).

This technique allows $I_{c.m.}(\theta, u)$ to be obtained without any

assumption about the functional form of the center-of-mass distribution. The unlimited frequency spectrum of the iterative solution allows accurate fitting of highly structured data. Since the only symmetry present in $I_{c.m.}$ is that which is present in the experimental data, no additional symmetry is imposed on $I_{c.m.}(\theta, u)$, as can be the case with algebraic techniques using expansion functions which have their own symmetry.

As discussed in chapter III, for many reactions one wishes to account for the energy dependence of the reactive cross section in the recovery of $I_{c.m.}(\theta, u)$. If the cross section increases with increasing energy, as is usually the case, this energy dependence has the effect of increasing the importance of the larger (i.e. higher relative velocity) Newton diagrams. If the cross section energy dependence has a negative slope the smaller Newton diagrams will be emphasized. In either case the solution of equation (10) must account for the energy dependence, hence equation (10) should really be written:

$$\bar{I}_{LAB}(\Theta, v) = \sum_i f_I(v_1, v_2, \gamma) f_E(v_1^2 + v_2^2)\, I_{LAB}(\Theta_i, v_i). \quad (13)$$

In this case the Newton diagram which maximizes $f_I \cdot f_E$ is used as the "canonical" Newton diagram of equation (9). The functional form for f_E is of course determined by the observed energy dependence of the reactive cross section.

Program RECON has been written to solve equation (13) for $I_{LAB}(\Theta, v)$ using the ratio method just described. RECON draws heavily from the program DORS written by Siska.[4] However, it contains several modifications and additional features which were found to be necessary in

dealing with data sets such as those for the $F_2 + XI \rightarrow XIF + F$ reactions and the $Cl + Br_2 \rightarrow ClBr + Cl$ reaction.

The input for RECON consists of the experimental differential cross section data, $\bar{I}_{LAB}(\theta, v)$, for up to 10 values of θ and up to thirty values of the velocity, v, v = VO, VO + DV, VO + 2DV, ..., VO + (NV-1)DV. Input data describing the velocity distributions in each of the reactant beams, the nominal intersection angle between the beams, and the distribution of intersection angles about this nominal value are required to establish $f_1(v_1, v_2, \gamma)$ for use in solving equation (13). Also required as input are data on the cross section energy dependence to establish the f_E weighting of equation (13).

The energy dependence data can be input in the form of a table of values of the relative magnitude of the reaction cross section versus energy. Alternatively the cross section energy dependence can be described functionally by selecting values for up to four input parameters, EPEAK, EZERO, POW1, POW2, which determine the functional behavior. This functional weighting and the weighting using a table of values of the magnitude of the reactive cross section can be used simultaneously. The functional form used in the cross section energy weighting is specified in subroutine CNEWT. In the listing of RECON which follows, the functional form has been chosen to describe a cross section which has zero magnitude at energy EZERO, rises rapidly from EZERO then gradually tapers off to a maximum at energy EPEAK, and which has a constant value for energies above EPEAK:

WATE = 1.0 for E > EPEAK

$$WATE = 1.0 \cdot \left(\frac{EPEAK - E}{EPEAK - EZERO}\right)^{POW2} \quad \text{for } EZERO < E \leq EPEAK$$

$$WATE = 0.0 \quad \text{for } E \leq EZERO$$

The factor f_E of equation (13) is given by WATE·EFAC(E) where EFAC(E) is the cross section energy weighting as determined from the tabular input data on the cross section energy dependence. When no functional energy weighting is used WATE = 1.0; when no tabular data on the cross section energy dependence is used EFAC(E) = 1.0 for all energies E.

The weighting, $f_i(v_1, v_2, \gamma)\cdot f_E(v_1^2 + v_2^2)$, used in equation (13) is given by $f_E\cdot(v_1^2 + v_2^2)^{1/2}\cdot f(v_1)\cdot f(v_2)\cdot f(\gamma)$ when energy weighting of the cross section is included. $f(v_1)$ and $f(v_2)$ are the velocity distribution functions of the reactant beams and $f(\gamma)$ is the intersection angle distribution. These distributions are calculated from input parameters describing the velocity and intersection angle distributions. The "canonical" Newton diagram of equation (9) is taken as that which maximizes $f_E\cdot(v_1^2 + v_2^2)^{1/2}\cdot f(v_1)\cdot f(v_2)\ f(\gamma)$. When no cross section energy dependence is used $f_E = 1.0$ and the f_i weighting in equation (13) is given by $f_i = (v_1^2 + v_2^2)^{S/2}\cdot f(v_1)\cdot f(v_2)\cdot f(\gamma)$, where S is specified by a data statement in subroutine MPND. S = 1 or 2 usually. In the case of no energy weighting the "canonical" Newton diagram is taken as that which maximizes this f_i.

When a large range of Newton diagrams makes a significant contribution in equation (13) the $I_{LAB}(\theta, v)$ distribution will be considerably sharper than the $\bar{I}_{LAB}(\theta, v)$ data. If for such a data set $\bar{I}_{LAB}(\theta, v)$ has been measured for only three or four values of θ, an iterative technique

like the ratio method will sometimes not be effective in recovering $I_{LAB}(\theta, v)$, since the grid of angles θ may be too coarse to allow a sufficiently narrow, $I_{LAB}(\theta, v)$ to be recovered. This is never a problem in v-space, as the data are always available in as fine a grid as necessary from the measured TOF spectra.

In such a case the quality of the fit obtained with RECON can be improved by establishing more data points, i.e. $\bar{I}_{LAB}(\theta, v)$, for additional values of θ. RECON has a provision for this. Using linear bivariate interpolation $\bar{I}_{LAB}(\theta, v)$ for selected values of θ is obtained from the measured $\bar{I}_{LAB}(\theta, v)$ data. For example, if $\bar{I}_{LAB}$ has been measured for $\theta = 10°$, $20°$, and $30°$, RECON can calculate $\bar{I}_{LAB}$ at any θ, $10° < \theta < 30°$. These interpolated data give greater flexibility to the $I_{LAB}(\theta, v)$ distribution than provided by the limited number of values of θ which occur in the measured data. In the example given, if only three values of θ are represented $\langle I_{LAB}(\theta, v)\rangle_v = \bar{I}_{LAB}(\theta, v)$ will be of necessity triangular. The addition of data for only two other values of θ, allows a much greater range of profiles for $\langle I_{LAB}(\theta, v)\rangle_v$. This feature must of course be used with great care, and can only be used when the angular distribution and measured velocity distributions indicate that linear interpolation is reasonable.

At times one may wish to determine $I_{c.m.}(\theta, u)$ for some product species for which $\bar{I}_{LAB}(\theta, v)$ are complicated by ionizer fragmentation of some other species. This is the case for the IF product of $F_2 + I_2 \rightarrow I + IF + F$ for which the $\bar{I}_{LAB}(\theta, v)$ data are complicated by ionizer fragmentation of the I_2F product of the reaction $F_2 + I_2 \rightarrow$

$I_2F + F$. In this case, it is necessary to subtract from the $\bar{I}_{LAB}(\Theta, v)$ data for the IF product, the contribution due to I_2F, i.e. it is necessary to subtract some fraction of $\bar{I}'_{LAB}(\Theta, v)$, the distribution for I_2F, for each Θ, v point. This fraction to be subtracted is determined from the measured I_2F^+/IF^+ fragmentation ratio of I_2F. Program RECON allows both $\bar{I}_{LAB}(\Theta, v)$ and $\bar{I}'_{LAB}(\Theta, v)$ data sets to be input and then corrects $\bar{I}_{LAB}(\Theta, v)$ by subtraction of $\bar{I}'_{LAB}(\Theta, v)$:

$$\bar{I}_{LAB}(\Theta_i, v_j)_{CORRECTED} = \bar{I}_{LAB}(\Theta_i, v_j) - k \cdot \bar{I}'_{LAB}(\Theta_i, v_j) \qquad (14)$$

for the complete range of i and j, where k is the fragmentation ratio.

As output RECON of course reproduces the input data. It prints out the beam velocities, V1 and V2, intersection angle, GAMMA, and the $f(v_1)$, $f(v_2)$, $f(\gamma)$ weighting factors, as well as F(V1, V2, G), the $f_E \cdot f_i$ weighting for each Newton diagram used in equation (13). THC, the center-of-mass angle ($\Theta_{c.m.}$ of Fig. 1), and EREL, the collision energy in kcal/mole, are also given for each Newton diagram used in equation (13).

The principal output of course consists of the $\bar{I}^{(n)}_{LAB}(\Theta, v)$ and $I^{(n)}_{LAB}(\Theta, v)$ for each iteration n. These data are headed FOLD and UNFOLD in the output. $\bar{I}^{EXPT}_{LAB}(\Theta, v)$ is also given under the heading EXPT. A fitting error defined as:

$$100 \cdot \sqrt{N \cdot \sum_{\Theta,v} (\bar{I}^{EXPT}_{LAB}(\Theta, v) - \bar{I}^{(n)}_{LAB}(\Theta, v))^2} \Big/ \sum_{\Theta,v} \bar{I}^{EXPT}_{LAB}(\Theta, v), \qquad (15)$$

where N is the number of data points is also given for each iteration n. RECON also computes and outputs the lab angular distributions,

$\sum_v \bar{I}_{LAB}(\theta, v)\cdot v$, for the experimental data and for $\bar{I}^{(n)}_{LAB}$, for each iteration n.

After a specified number of iterations RECON then computes the center-of-mass velocity distribution, $\sum_\theta I_{c.m.}(\theta, u)$, and angular distribution, $\sum_u I_{c.m.}(\theta, u)$, for the $I_{c.m.}(\theta, u)$ which has been recovered in the fitting procedure. These distributions are headed P(U) and P(TH) in the output. The program determines the finest possible grid of velocities and angles which can be accommodated using 20 values of u and θ.

$I_{c.m.}(\theta, u)$ itself is given as a contour plot generated by the line printer, superimposed on the canonical Newton diagram, using characters 0, 1, 2, ..., 9, A, B, ... K to indicate contour values 0-20. A contour corresponding to an integral value is drawn between successive characters. For example, the I = 4 contour occurs at the boundary between the 3's and 4's. The contour map is positioned on the output so that the axes of the paper correspond to the reactant beam directions when $\gamma = 90°$. The relative orientation of the beam velocities, i.e. which axis of the paper corresponds to which beam, is chosen so as to give maximum resolution in the plotted contour map. At least one beam velocity, given by a chain of arrows, is always plotted, along with the position of the center of mass ($) in order to indicate this orientation.

A description of the input variables, a program listing, and sample output of program RECON follow.

Program RECON Input Variables

Variable	Description
IL	Heading for all output.
ITMAX	Number of iterations desired, n $\leq$ 9.
IESCALE, NE	Control variables for energy weighting the cross section. If IESCALE $\neq$ 0 the program reads in NE ($\leq$ 20) values of the collision energy and the relative magnitude of the reactive cross section, $\sigma(E)$, at that energy. This allows use of the experimentally determined cross section energy dependence which is only available in tabular form. IESCALE = 0 eliminates this feature.
EPEAK, EZERO, POW1, POW2	Parameters available for use in a functional representation of the energy dependence of the cross section. Such a functional representation of $\sigma(E)$ can be used in place of tabular data or in conjunction with tabular data. The meaning of these parameters is determined by the functional form of $\sigma(E)$, chosen by the user, in subroutine CNEWT. EPEAK$\leq$0 gives no energy weighting of the cross section in this form.
E(IE), SIGMA(IE), IE=1, NE	Arrays giving the collision energy, E(IE), and magnitude of the cross section at that energy, SIGMA(IE). E in kcal/mole, SIGMA in any units.
NVB(1), NVB(2)	Number of velocities in each beam to be used in solving equation (13). NVB must be odd for a nozzle beam; even (or 1) for a velocity selected beam.
NGAM	Number of intersection angles to be used in solving equation (13). NVB(1) · NVB(2) · NGAM = total number of Newton diagram transformations, which must be less than 400. The actual number of Newton diagrams used by the program is somewhat less than this, as very low probability Newton diagrams (less than .05·"probability" of the most probable Newton diagram) are not used.

Program RECON Input Variables (Cont'd)

Variable	Description
GB(1), GB(2)	Masses, in a. m. u., of the reactant particles.
GAMMA	Nominal value of the beam intersection angle in degrees.
HWIDB	Half width, in degrees, of the interaction angle distribution.
VPAR(I, J), I = 1, 5, J = 1, 2	Parameters describing the velocity distributions of the two reactant beams. I is the parameter index, J is the beam index. VPAR(5, J) indicate type of beam velocity distribution. VPAR(5, J)<0 indicates a supersonic nozzle beam. Then VPAR(1, J) is α_o, VPAR(2, J) is γ, and VPAR(3, J) = M, where α_o, γ, and M are the most probable velocity in the nozzle, the ratio of specific heats, and the beam Mach number, respectively. VPAR(4, J) is not used. VPAR(5, J) = 0 indicates a velocity selected beam. VPAR(1, J) is then the selected velocity, VPAR(2, J) is β and VPAR(3, J) is γ, where β, γ are the mechanical velocity selector parameters as defined by Hostettler and Bernstein.[5] VPAR(4, J) is again not used. VPAR(5, J)>0 assumes a distribution fitted to the UDIST function of Entemann.[6]
NTHL	Number of lab angles for which $\bar{I}_{LAB}(\theta, v)$ data are to be analyzed. NTHL$\leq$10.
NV	Number of velocities for which $I_{LAB}(\theta, v)$ data are to be analyzed. NV$\leq$30.
DV	Spacing, in units of 10^4 cm/sec, between velocities in the $\bar{I}_{LAB}(\theta, v)$ data.
VO	Smallest velocity, in units of 10^4 cm/sec, for which $\bar{I}_{LAB}(\theta, v)$ data are to be input. VO must be the same for all angles.
VS	Lab velocity below which data are not analyzed. VS = VO usually.
VSP	Lab velocity below which data are not to be contour plotted. VSP$\geq$VO. Usually VSP = VO.

Program RECON Input Variables (Cont'd)

Variable	Description
THL(ITHL) ITHL = 1, NTHL	Array of lab angles, θ. THL(1)<THL(2)<....<THL(NTHL).
INORM	Control variable. If INORM ≠ 0 the current THL(ITHL) is used to normalize the angular distribution ($\bar{I}_{CALC}(\theta) = {}_v\bar{I}_{CALC}(\theta, v)\cdot v$) calculated by RECON to the "experimental" angular distribution ($\bar{I}_{LAB}(\theta) = {}_v\bar{I}_{LAB}(\theta, v)\cdot v$)), $\bar{I}_{CALC}(\theta) = \bar{I}_{LAB}(\theta) = 1.0$ for θ = THL(ITHL).
ISIGN	Control variable. ISIGN = 0 means that laboratory data $\bar{I}_{LAB}(\theta, v)$ have been obtained for the current angle THL(ITHL), and that these data will be read in to RECON. ISIGN ≠ 0 implies that $\bar{I}_{LAB}(\theta, v)$ data are not available for the THL(ITHL) and will thus not be read in. The program will "calculate" the $\bar{I}_{LAB}(\theta, v)$ data at this THL(ITHL) by interpolation of the $\bar{I}_{LAB}(\theta, v)$ data at THL(ITHL-1) and THL(ITHL+1). This allows generation of more data than was actually obtained, and sometimes expedites the accurate recovery of $I_{LAB}(\theta, v)$ when the grid of lab data is "coarse."
TSCAL(ITHL) ITHL = 1, NTHL	If ISIGN = 0, TSCAL(ITHL) is not used. If ISIGN ≠ 0, TSCAL(ITHL) is the normalization factor for θ = THL(ITHL), determined from the angular distribution. It is equal to NORM·DIST where NORM, DIST are as given in the description of the input variables for program FLUX. It ensures that for the $\bar{I}_{LAB}(\theta, v)$ data interpolated $\sum_v \bar{I}_{LAB}(\theta, v)\cdot v\big\|_{\theta = THL(ITHL)} = \sum_t \left.\frac{d^2N_{LAB}(\theta, t)}{d\theta dt}\right\|_{\theta = THL(ITHL)} = \left.\frac{dN_{LAB}(\theta)}{d\theta}\right\|_{\theta = THL(ITHL)} = NORM$ The value of TSCAL(ITHL) used must be consistent with the values for NORM used in program FLUX to obtain $\bar{I}_{LAB}(\theta, v)$ at θ = THL(ITHL-1) and θ = THL(ITHL+1).

Program RECON Input Variables (Cont'd)

Variable	Description
PE(IV, ITHL) IV = 1, NV ITHL = 1, NTHL	The lab data $\bar{I}_{LAB}(\theta, v)$. These data are read in only if ISIGN = 0 for the current value of ITHL
SUBFAC	The factor k of equation (14). If SUBFAC = 0.0 this feature is not used.
PSUB(IV, ITH)	The array of $\bar{I}_{LAB}(\theta, v)$ which is to be subtracted from $\bar{I}_{LAB}(\theta, v)$ as in equation (14). Not input if SUBFAC = 0.0
ICONT	Control variable. ICONT = 0 stops program execution. ICONT ≠ 0 indicates another data set is to be input and program returns to input routine.

```
      PROGRAM RECOIL(INPUT,OUTPUT,TAPE5=INPUT,TAPE6=OUTPUT)
      COMMON/FSCAL/FSCALE,NF,S,SIGMA
      COMMON/PLIMITS/ATH,ATL,DELT,THMIN,UMIN
      COMMON/CONST/PI,PI2,C,RMP,EMC2,HBARC2
      COMMON/PDF/VL,THL,DV,DVP,VPS,THL,IVS,VS,VSP
      COMMON/PROTON/VV1,VV2,CKMP,CYMP,CJSYMP,SINTVMP
      COMMON/VSCALE/VVX,VY
      DIMENSION P(3),U(3),PP(3),PPP(3),V(3),VP(3),VPP(3)
      DIMENSION PSIG(10)
      DIMENSION CX(4),CY(4),GA(2),GB(2),VPAR(5,2),FSCALE(4,10),CX(4,10),CY(4,10),
     1CJSTV(-10:10),SINTV(-10:10),ITH(-10:10),IL(4),SUMEF(10),SQAEF(10)
      DIMENSION ENG(10),PCMP(30,10),PMOM(10),ECMIN(10),TSCALE(10)
      DIMENSION P(3,10),PP(3,10),PPP(3,10),V(3,10),VL(3),VP(3,10),THL(10),VX(30,10)
     1,VY(30,10),WEIGHT(30,10)
      LOGICAL ULO,UHI,ILO,IHI
  999 CONTINUE
C
C  READ AND WRITE THE INPUT PARAMETERS.
C
      READ(5,1010) IL
      READ(5,1023) ITMAX
      READ(5,1033) ISCALE,NF,(PARAK,I=2,5),PIW1,PIW2
      IF(ISCALE.EQ.0) GO TO 8
      READ(5,1035) (S(IF),IF=1,NF)
      READ(5,1036) (SIGMA(IF),IF=1,NF)
    8 READ(5,1001) NVP(1),DV1(2),VMAX,GB(1),GB(2),GAMMA,WIDB
      READ(5,1002) (VPAR(I,1),I=1,5)
      READ(5,1002) (VPAR(I,2),I=1,5)
      READ(5,1003) ATHL,NV,DV,VO,VS,VSP
      NORM=1
      ISHIFT=0
      DO 2 JAY=1,NTHL
      ITHL=JAY-ISHIFT
      NVS(JAY)=0
      READ(5,1004) THL(ITHL),ITH(ITHL),ISIGN,ISCALE(JAY)
      SIG(JAY)=THL(ITHL)
      IF(ISIGN .NE. 0) NORM=JAY
      IF(ISIGN) 13,14,13
   13 ISHIFT=ISHIFT+1
      NVS(JAY)=1
      GO TO 2
   14 DO 1 IV=1,NV
    1 VL(IV,ITHL)=FLOAT(IV-1)*DV+VO
      READ(5,1005) (PP(IV,ITHL),IV=1,NV)
    2 LSHIFT(JAY)=ISHIFT
 9000 WRITE(6,1019) IL
      WRITE(6,1006)
      WRITE(6,1007) GB(1),GB(2)
      T1=(VPAR(1,1)/1.28485)**2*GB(1)
      T2=(VPAR(1,2)/1.28485)**2*GB(2)
      WRITE(6,1008) T1,T2
      WRITE(6,1009) VPAR(2,1),VPAR(2,2)
      WRITE(6,1010) VPAR(3,1),VPAR(3,2)
      IF(VPAR(5,1)) 110,111,112
  110 IF(VPAR(5,2)) 113,114,112
  111 IF(VPAR(5,2)) 115,116,112
  113 WRITE(6,1011)
      GO TO 112
  114 WRITE(6,1012)
```

```
      GO TO 112
  115 WRITE(6,1013)
      GO TO 112
  116 WRITE(6,1014)
  112 WRITE(6,1015) NVB(1),NVB(2)
      WRITE(6,1016) NTHL,NV,DV,VO,VS,VSP
      WRITE(6,1017) ITMAX
 1000 FORMAT(8A10)
 1001 FORMAT(3I5,5X,6F10.4)
 1002 FORMAT(8F10.4)
 1003 FORMAT(2I5,4F10.3)
 1004 FORMAT(5X,F6.1,2I5,F10.2)
 1005 FORMAT(8F10.2)
 1006 FORMAT(1HO,30X,21HBEAM INPUT PARAMETERS/1HO,44X,7HPRIMARY,8X,9HSEC
     1ONDARY)
 1007 FORMAT(1HO,9X,6HMASS,32X,F6.2,11X,F6.2)
 1008 FORMAT(1H ,9X,11HTEMPERATURE,25X,F6.1,11X,F6.1)
 1009 FORMAT(1H ,9X,5HGAMMA,33X,F4.2,13X,F4.2)
 1010 FORMAT(1H ,9X,11HMACH NUMBER,26X,F5.2,12X,F5.2)
 1011 FORMAT(1H ,9X,17HDISTRIBUTION TYPE,19X,6HNOZZLE,11X,6HNOZZLE)
 1012 FORMAT(1H ,9X,17HDISTRIBUTION TYPE,19X,6HNOZZLE,10X,7HVEL SEL)
 1013 FORMAT(1H ,9X,17HDISTRIBUTION TYPE,18X,7HVEL SEL,11X,6HNOZZLE)
 1014 FORMAT(1H ,9X,17HDISTRIBUTION TYPE,18X,7HVEL SEL,10X,7HVEL SEL)
 1015 FORMAT(1H ,9X,23HNO. VELOCITIES AVERAGED,17X,I2,15X,I2)
 1016 FORMAT(1HO,* NUMBER OF LAB ANGLES **,I3/1HO,* NUMBER OF VELOCITIES
     1 AT EACH ANGLE **,I3/1HO,* VELOCITY INCREMENT **,F5.2/1HO,* FIRST
     1VELOCITY **,F5.2/1HO,* ANALYSIS CUTOFF VELOCITY **,F5.2/1HO,* CONT
     1OUR PLOT CUTOFF VELOCITY **,F5.2)
 1017 FORMAT(1HO,* NUMBER OF ITERATIONS REQUESTED IS*,I7)
 1018 FORMAT(1H1,8A10)
 1023 FORMAT(I5,5X,5F10.2,I5)
C
C   CALCULATE NEWTON DIAGRAMS AND PARAMETERS.
C
      CALL CNEWT
      CXMP=CX(MP)
      CYMP=CY(MP)
      COSTVMP=COSTV(MP)
      SINTVMP=SINTV(MP)
      IVS=(VS-VO)/DV+1.1
 9100 IT=0
C
C   CALCULATE BY INTERPOLATION INTENSITY DATA FOR THE REQUESTED ANGLES
C
      MTHL=NTHL
      NTHL=NTHL-ISHIFT
      DO 150 ITHL=1,MTHL
      DO 150 IV=1,NV
  150 PI(IV,ITHL)=PE(IV,ITHL)
      DO 120 JAY=1,NTHL
      IF(MOVE(JAY)) 121,122,121
  122 LBL=LSHIFT(JAY)
      DO 124 IDA=1,NV
  124 PTEMP(IDA,JAY)=PE(IDA,JAY-LBL)
      GO TO 120
  121 SUMPT=0.0
      DO 123 IDI=1,NV
      VV=FLOAT(IDA-1)*DV+V
      TL=ANG(JAY)
      CALL INTXT(VV,TL,PZ)
      PTEMP(IDA,JAY)=PZ
  123 SUMPT=SUMPT+PZ/VV
```

```
      SKIP=DV*SUMPT/TSCALE(JAY)/1000.
      SUMPE(JAY)=SUMPT/SKIP
      DO 125 IDA=1,NV
  125 PTEMP(IDA,JAY)=PTEMP(IDA,JAY)/SKIP
  120 CONTINUE
      NTHL=NTHL
C
C     READ ARRAY OF BACKGROUND INTENSITIES TO BE SUBTRACTED
C
      READ(5,1000) SUBFAC
      IF(SUBFAC .EQ. 0.0) GO TO 5
      DO 6666 ITHL=1,NTHL
      READ(5,1005) (PSUB(IV),IV=1,NV)
      DO 6000 IV=1,NV
      PE(IV,ITHL)=PE(IV,ITHL)-PSUB(IV)*SUBFAC
 6000 CONTINUE
 6666 CONTINUE
    5 NPTS=0
      SUM=0.0

C   CALCULATE VELOCITY COMPONENTS
C   CALCULATE ANGULAR DISTRIBUTION BY SUMMATION OVER VL
C   WEIGHT DATA ACCORDING TO STASTICAL UNCERTAINTY

      DO 4 ITHL=1,NTHL
      MOVIT=MOVE(ITHL)
      SUMPE=0.0
      SUMPEF=0.0
      THL(ITHL)=ANG(ITHL)
      T=THL(ITHL)*0.0174533
      CT=COS(T)
      ST=SIN(T)
      DO 3 IV=IVS,NV
      VL(IV,ITHL)=FLOAT(IV-1)*DV+VO
      VX(IV,ITHL)=VL(IV,ITHL)*CT
      VY(IV,ITHL)=VL(IV,ITHL)*ST
      PE(IV,ITHL)=PTEMP(IV,ITHL)
      IF(PE(IV,ITHL) .LE. 0.0) PE(IV,ITHL)=0.0001
      P(IV,ITHL)=PE(IV,ITHL)
      WEIGHT(IV,ITHL)=SQRT(PE(IV,ITHL)*VL(IV,ITHL))
      IF(MOVIT) 3,6,3
    6 NPTS=NPTS+1
      SUMPEF=SUMPEF+PE(IV,ITHL)/VL(IV,ITHL)
      SUMPE=SUMPE+PE(IV,ITHL)*WEIGHT(IV,ITHL)
    3 CONTINUE
      IF(MOVIT) 4,7,4
    7 SUMEE(ITHL)=SUMPEF
      SUM=SUM+SUMPE
    4 CONTINUE
      DIVFAC=SUMEE(NORM)
C
C   ESTABLISH LIMITS FOR EXTRAPOLATION AND CONTOUR MAP
C
      ITLO=0
      ITHI=0
      IF(THL(NTHL).LE. THC) ITHI=1
      IF(THL(1) .GE. THC) ITLO=1
      IDOIT=1
 7777 CALL ALIMIT(IDOIT,ITHI,ITLO)
      IDOIT=0
      ERR=0.0
      DO 25 ITHL=1,NTHL
```

```
      MOVIT=MOVE(ITHL)
      SUMPF=0.0
      DO 20 IV=IVS,NV
      F=0.0
C
C  VELOCITY AVEARGING LOOP.
C
C
C       IJK      MP
C  L48 --> CM --> L48 TRANSFORMATION.
C
      DO 15 IJK=1,NGRID
      IF(IT3(IJK) .NE. 0) GO TO 15
      UXL=VX(IV,ITHL)-CX(IJK)
      UYL=VY(IV,ITHL)-CY(IJK)
      UX=UXL*COSTV(IJK)-UYL*SINTV(IJK)
      UY=UXL*SINTV(IJK)+UYL*COSTV(IJK)
      VXI=UX*COSTVMP+UY*SINTVMP+CXMP
      VYI=-UX*SINTVMP+UY*COSTVMP+CYMP
      VI=SQRT(VXI*VXI+VYI*VYI)
      TI=ATAN2(VYI,VXI)/0.3174533
      CALL INTEXT(VI,TI,PI)
      F=F+FABG(IJK)*(VL(IV,ITHL)/VI)**2*PI
   15 CONTINUE
      PE(IV,ITHL)=F
      SUMPF=SUMPF+F/VL(IV,ITHL)
      IF(MOVIT) 20,22,20
   22 ERR=ERR+((PE(IV,ITHL) -F)*WEIGHT(IV,ITHL))**2
   20 CONTINUE
   23 SUMPF(ITHL)=SUMPF
   24 CONTINUE
      ERR=100.0*SQRT(NPTS*ERR)/SUM
      WRITE(6,1318) IT,ERR
 1318 FORMAT(1H0,*ITERATION NUMBER =*,I2,* ERROR =*,F7.2)
C
C  CORRECT LAST GUESS BY RATIO METHOD.
C
      DO 250 ITHL=1,NTH
      DO 250 IV=1,NV
      IF(PE(IV,ITHL) .LT. 1.0E-30) GO TO 250
      P(IV,ITHL)=P(IV,ITHL)*PE(IV,ITHL)/PE(IV,ITHL)
  250 CONTINUE
C
C   OUTPUT RESULTS.
C
 5000 NPG=NTHL/3
      IF(3*NPG .LT. NTHL) NPG=NPG+1
      DO 60 IP=1,NPG
      NT1=3*(IP-1)+1
      NT2=MIN(NT1+2,NTHL)
      WRITE(6,1030)  (THL(ITHL),ITHL=NT1,NT2)
      WRITE(6,1031)
      DO 55 IV=IVS,NV
   55 WRITE(6,1032) (VL(IV,ITHL),PE(IV,ITHL),PE(IV,ITHL),P(IV,ITHL),ITHL
     1=NT1,NT2)
   60 CONTINUE
      WRITE(6,1029) NPTS
 1029 FORMAT(1HJ1I,* DATA POINTS*)
 1030 FORMAT(1HOLAB ANGLE,3(15X,F5.1,18X))
 1031 FORMAT(1H0,3(3X3HV,L7X6HEXPT6X4HFOLD6X4HUNFOLD4X))
 1032 FORMAT(3(3X,F5.2,2F10.2,2X,F10.2,3X))
      WRITE(6,1033)
```

```
      DO 65 ITHL=1,NTHL
   63 WRITE(6,1036) THL(ITHL),SUMF(ITHL)/DIVFAC,SUMEF(ITHL)/SUMEF(NORM
     1)
   65 CONTINUE
 1035 FORMAT(1H0,1HX,9X,4HF(X),10X,'ANGULAR DISTRIBUTION',6X,'THETA',8X,'EXPT',8X
     1,'CALC')
 1036 FORMAT(1H ,1X,F10.1,2X,F10.3,2X,F10.3)
 1027 ITH=ITH+1
      IF(IT .LT. ITMAX) GO TO 7777
C
C  COMPUTE AVERAGE CM ANGULAR AND VELOCITY DISTRIBUTIONS.
C
      WRITE(6,1034)
 1034 FORMAT(2H0UNNORMALIZED CM CROSS SECTION)
      DO 70 ITHL=1,NTHL
      DO 70 IV=1VS,NV
   70 P(IV,ITHL)=P(IV,ITHL)*((VX(IV,ITHL)-CXMP)**2+(VY(IV,ITHL)-CYMP)**2
     1)/VL(IV,ITHL)**2
      CALL CMSS
      IVS=(VSP-V0)/DV+1.1
      IF(ESCALE .EQ. 0) GO TO 1050
      WRITE(6,1039)
      WRITE(6,1100)
      DO 120 IE=1,NE
      WRITE(6,1113) E(IE),SIGMA(IE)
 1200 CONTINUE
 1090 FORMAT(1H0,*  CROSS SECTION AS A FUNCTION OF COLLISION ENERGY*)
 1100 FORMAT(1H ,*   ENERGY      SIGMA*)
 1110 FORMAT(2F10.2)
 1050 IF(EPEAK .EQ. 0.) GO TO 1062
      WRITE(6,1213) EPEAK
 1210 FORMAT(1H0,* EPEAK = *,F10.2)
      WRITE(6,1220) ZERO
 1220 FORMAT(1H0,* ZERO = *,F10.2)
      WRITE(6,1230) POW1,POW2
 1230 FORMAT(1H0,* POW1 = *,F5.1,* POW2 = *,F5.1)
C
C  CONTOUR PLOT OF CROSS SECTION.
C
 1062 WRITE(6,1060)
 1060 FORMAT(1H0)
      CALL CONTOUR
      WRITE(6,1070)
 1070 FORMAT(1H0)
      READ(5,1081) ICONT
      IF(ICONT .NE. 0) GO TO 999
      STOP
      END
      SUBROUTINE CONT
C
C   CALCULATES NEWTON DIAGRAMS AND THEIR WEIGHTS
C
      COMMON/ESCALE/IESCALE,NE,E,SIGMA
      COMMON/NEWTON/NVR,NGAM,GB,GAMMA,HHIOB,VPAR,FABG,CX,CY,COSTV,SINTV,
     1ITO,NGRID,MP,THC,EPEAK,ZERO,POW1,POW2
      COMMON/PICTURE/V1,V2,CXMP,CYMP,COSTVMP,SINTVMP
      DIMENSION E(20),SIGMA(20)
      DIMENSION FABG(400),CX(400),CY(400),COSTV(400),SINTV(400),ITO(400)
      DIMENSION VB(20,2),FB(20,3),GAM(5),FG(5),VPEL(400)
      DIMENSION NVR(2),VPAR(5,2),AJ(2),AL(2),GB(2)
      GL=GB(1)
      G2=GB(2)
```

```
      G=G1*G2
      GFAC=G1*G2*.00119S/G
      NH=NGAM/2+1
      ENH=NH
      DO 1 K=1,NGAM
      GAMA(K)=GAMMA+FLOAT(K-NH)*HWIDB/ENH
      FG(K)=1.
    1 IF(HWIDB.NE.0.) FG(K)=1.-ABS(GAM(K)-GAMMA)/HWIDB
      DO 30 L=1,2
      NV1=NVR(L)
      IF(VPAR(5,L)) 20,15,10
   10 ENH=AMAX0(NV1/2,1)
      DO 12 I=1,NV1
      VR(I,L)=VPAR(1,L)*FLOAT(I)/ENH
   12 FR(I,L)=UPIST(VR(I,L),VPAR(I,L))
      GO TO 30
   15 GMB=VPAR(3,L)-VPAR(2,L)
      DV=1.-VPAR(3,L)
      AO(1)=(1.+VPAR(3,L))/GMB
      A1(1)=-(1.+VPAR(2,L))/GMB
      AO(2)=-DV/GMB
      A1(2)=(1.-VPAR(2,L))/GMB
      DV=2./(DV*FLOAT(NV1+1))
      NH=1./DV+1.
      DV=DV/AO(1)
      DO 17 I=1,NV1
      R=1.+FLOAT(I-NH)*DV
      VR(I,L)=VPAR(1,L)+R
      II=1
      IF(R.GT.1.) II=2
   17 FR(I,L)=AO(II)+A1(II)*R
      GO TO 30
   20 AL1=VPAR(1,L)/SQRT(1.+(VPAR(2,L)-1.)/2.*VPAR(3,L)**2)
      VF=SQRT(VPAR(2,L)/2.)*VPAR(3,L)
      VPK=(VF+SQRT(VF**2+4.))/2.
      ENORM=EXP((VPK-VF)**2)/VPK**2
      DV=3.33022/FLOAT(NV1+1)
      NH=NV1/2+1
      DO 22 I=1,NV1
      R=VPK+FLOAT(I-NH)*DV
      VR(I,L)=AL1*R
   22 FR(I,L)=ENORM*R**2*EXP(-(VF-R)**2)
   30 CONTINUE
      EMP=0.
      NV1=NVR(1)
      NV2=NVR(2)
      IJK=0
      DO 4 K=1,NGAM
      GMK=GAM(K)*.0174533
      CG=COS(GMK)
      SG=SIN(GMK)
      DO 4 I=1,NV1
      V1=VR(I,1)
      DO 4 J=1,NV2
      V2=VR(J,2)
      IJK=IJK+1
      VREL(IJK)=(V1**2+V2**2-2.*V1*V2*CG)
      V=SQRT(VREL(IJK))
      ECOLL=VREL(IJK)*GFAC
C
C     ENERGY WEIGHTING OF CROSS SECTION - CHANGE TO SELECT THE FUNCTIONAL
C     FORM YOU DESIRE
```

```
      WATE=1.0
      IF(EPEAK) 9999,9999,9994
 9994 EASY = (EPEAK-ECOLL)
      IF(EASY) 9999,9999,9993
 9993 IF(ECOLL-EZERO) 9997,9997,9998
 9997 WATE=0.0
      GO TO 9999
 9998 WATE=1.0-(EASY/(EPEAK-EZERO))**POW)
 9999 FABG(IJK)=V*FB(I,1)*FB(J,2)*FG(K)*EFAC(ECOLL)*WATE
 9996 CX(IJK)=(G1*V1+G2*V2*CG)/G
      CY(IJK)=G2*V2*SG/G
      COSTV(IJK)=(V1-V2*CG)/V
      SINTV(IJK)=V2/V*SG
      IF(FMP.GT.FABG(IJK)) GO TO 4
      FMP=FABG(IJK)
      MP=IJK
      IMP=I
      JMP=J
    4 CONTINUE
      NGRID=NV1*NV2*NGAM
      IJK=0
      V1=VB(IMP,1)
      V2=VB(JMP,2)
      IF(ISCALE) 7500,6000,7500
 6000 IF(EPEAK) 7500,7000,7500
 7000 CALL MPND(VB,FB,IMP,JMP,V1,V2)
      MP=NGRID+1
      CX(MP)=G1*V1/G
      CY(MP)=G2*V2/G
      COSTV(MP)=V1/V
      SINTV(MP)=V2/V
 7500 V=SQRT(V1**2+V2**2)
      NH=0
      SUM=0.
      FMP=0.05*FMP
      DO 65 IJK=1,NGRID
      ITO(IJK)=1
      IF(FABG(IJK).LE.FMP) GO TO 65
      ITO(IJK)=0
      NH=NH+1
      SUM=SUM+FABG(IJK)
   65 CONTINUE
      DO 67 IJK=1,NGRID
      IF(ITO(IJK).NE.0) GO TO 67
      FABG(IJK)=FABG(IJK)/SUM
   67 CONTINUE
      WRITE(6,1000)
      IJK=0
      DO 8 K=1,NGAM
      DO 8 I=1,NV1
      DO 8 J=1,NV2
      IJK=IJK+1
      IF(ITO(IJK).NE.0) GO TO 8
      THC=ATAN(CY(IJK)/CX(IJK))/.0174533
      EREL=GFAC*VREL(IJK)
      WRITE(6,1001) VB(I,1),FB(I,1),VB(J,2),FB(J,2),GAM(K),FG(K),FABG(IJ
     1K),THC,EREL
    8 CONTINUE
      THC=ATAN(CY(MP)/CX(MP))/.0174533
      EREL=GFAC*V*V
      WRITE(6,1002) V1,V2,THC,EREL,NH
 1000 FORMAT(1H0,6X,2HV1,7X,5HF(V1),6X,2HV2,7X,5HF(V2),4X,5HGAMMA,6X,4HF(G),3X,10HF(V1
```

```
     1,V2,G)4X3HTHC6X4HEREFL)
 1001 FORMAT(6F10.2,F10.4,2F10.2)
 1002 FORMAT(F10.2,10X,F10.2,40X,2F10.2,*  (CANONICAL)*
     1/1H09X15,*  NEWTON DIAGRAMS*)
      RETURN
      END
      FUNCTION EFAC(ECOLL)
C
C     DETERMINES ENERGY WEIGHTING OF CROSS SECTION FROM TABLE OF
C     EXPERIMENTAL VALUES
C
      COMMON/ESCALE/IESCALE,NE,E,SIGMA
      DIMENSION E(20),SIGMA(20)
      IF(IESCALE .NE. 0) GO TO 2
      EFAC=1.0
      RETURN
    2 DO 10 IE=1,NE
      IF(E(IE) .GT. ECOLL) GO TO 20
   10 CONTINUE
   20 IE1=IE
      IF(IE1.EQ. 1) GO TO 30
      IE0=IE-1
                 EFAC=(SIG*A(IE1)-SIGMA(IE0))/(E(IE1)-E(IE0))*(ECOLL-E(IE0))
     1 + SIGMA(IE0)
      GO TO 40
   30 EFAC=0.0
   40 RETURN
      END
      FUNCTION UDIST(U,PAR)
C  PARAMETRIC FORM FOR VELOCITY DISTRIBUTIONS
C
      DIMENSION PAR(1)
      R=U/PAR(1)
      IF(R.GT.1.) GO TO 20
      A=PAR(2)
      B=PAR(3)
   10 ALR=ALOG(R)
      UDIST=EXP(A*(ALR+(1.-EXP(B*ALR))/B))
      RETURN
   20 A=PAR(4)
      B=PAR(5)
      GO TO 10
      END
C
      SUBROUTINE MPND(V8,FB,I,J,V1,V2)
C  FINDS CANONICAL NEWTON DIAGRAM
C  V1,V2 ARE FOUND WHICH MAXIMIZE V8**S*N1*N2
C
      DIMENSION V8(20,2),FB(20,2)
      DIMENSION A(2),B(2),C(2),V(2),DV(2),F(2),D(2,2)
      REAL N
      DATA S/1./
      IF(I.EQ.1.OR.J.EQ.1) GO TO 6
      DO 1 L=1,2
      M=I
      IF(L.EQ.2) M=J
      H=V8(M+1,L)-V8(M,L)
      A(L)=(FB(M+1,L)-2.*FB(M,L)+FB(M-1,L))/(2.*H**2)
      B(L)=(FB(M+1,L)-FB(M,L))/H-A(L)*(2.*V8(M,L)+H)
      C(L)=FB(M,L)-V8(M,L)*(A(L)*V8(M,L)+B(L))
    1 V(L)=V8(M,L)
    2 V0=V(1)**2+V(2)**2
```

```
      DO 3 L=1,2
      S=S(L)+V(L)*(S(L)+V(L)*3(L))
      D2M=2.*S(L)
      D1M=S(L)+D2M*V(L)
      P=D2M/P
      S(L)=V(L)+V*P/S
      D(L,L)=1.+(2.*V(L)**2+V*P*(P*V(L)-2.*S(L))/S
      M=3-L
    3 D(L,M)=2.*V(K)*P/S
      DO 5 L=1,2
      M=3-L
      DV(L)=(F(1)*D(2,M)+(2)*D(1,M))/(D(1,L)*D(2,M)-D(2,L)*D(1,M))
    5 V(L)=V(L)-DV(L)
      IF(ABS(DV(2)).GT.1.E-3*V(1).OR.ABS(DV(2)).GT.1.E-3*V(2)) GO TO 2
      V1=V(1)
      V2=V(2)
      RETURN
    6 V1=VP(1,1)
      V2=VP(J,2)
      RETURN
      END
      SUBROUTINE ALIMIT(IDOIT,ITHI,ITH))
C
C     FINDS LIMITS FOR EXTRAPOLATION  IN SUBROUTINE INTEXT
C     DETERMINES RANGE OF C.M. VELOCITIES AND ANGLES WHICH CORRESPONDS TO
C     THE RANGE OF EXPERIMENTAL DATA
C
      COMMON/APPAY/PP,P
      COMMON/LIMITS/DITH,DTL,DTU,DIT,THMIN,UMIN
      COMMON/JOU/VL,THL,PV,PV,VC,NTHL,IVS,VS,VSP
      COMMON/PICTUR/V1,V2,CXMP,CYMP,COSTVMP,SINTVMP
      COMMON/SOLVL/VX,VY
      DIMENSION P(3),10),P(30,10),VX(30,10),VY(30,10),VL(30,10),THL(10)
      DO 10 K=1,2
      J=1+(K-1)*(NTHL-1)
      J1=J+1-2*(K-1)
      DITH=THL(J1)-THL(J)
      IC(UNT=)
      SUMDIT=0.0
      DO 6 IV=IVS,VV
      DENOM=P(IV,J1)+P(IV,J)
      IF(DENOM .LE. 0.0) GO TO 6
      DT=ABS(P(IV,J)-P(IV,J1)/DENOM)
      SUMDIT=SUMDIT+DT
      IC(UNT=IC(UNT+1
    6 CONTINUE
      IF(IC(UNT .EQ. 0) WRITE(6,8889)
 8889 FORMAT(1H0,*ERROR IN LIMITING ANGLES &OUTINE*)
      DT=SUMDIT/IC(UNT
      IF(K-2) 7,8,8
    7 DTL=DT
      GO TO 10
    8 DTH=DT
   10 CONTINUE
      IF(IDOIT) 200,300,200
  200 IF(ITHI) 11,11,12
   12 DO 14 K=1,2
      I=IVS+(K-1)*(NV-IVS)
      UXL=VX(I,NTHL)-CXMP
      UYL=VY(I,NTHL)-CYMP
      UX=UXL*COSTVMP-UYL*SINTVMP
      UY=UXL*SINTVMP+UYL*COSTVMP
```

```
      TH=ATAN2(UY,UX)
      U2=(UX*UX+UY*UY)
      US=SQRT(U2)
      IF(K-1) 15,15,14
   15 THMIN=TH
      GO TO 13
   14 THMAX=TH
   13 CONTINUE
      DIT=(THMAX-THMIN)/20.
      GO TO 20
    1 IF(ITL0) 16,16,17
   17 DO 18 K=1,2
      I=IVS+(K-1)*(NV-IVS)
      UXL=VX(I,J)-CXMP
      UYL=VY(I,J)-CYMP
      UX=UXL*COSTVMP-UYL*SINTVMP
      UY=UXL*SINTVMP+UYL*COSTVMP
      U2=UX*UX+UY*UY
      TH=ATAN2(UY,UX)
      US=SQRT(U2)
      IF(K-1) 19,19,21
   19 THMAX=TH
      GO TO 18
   21 THMIN=TH
   18 CONTINUE
      DIT=(6.28319-THMIN+THMAX)/20.
      GO TO 20
   16 THMIN=-3.14159
      UMIN=0.0
      DIT=0.31+159
      GO TO 40
   20 J=ITHI*NTHL+ITL
      UMIN=1000.
      DO 30 I=IVS,NV
      U=SQRT((VX(I,J)-CXMP)**2+(VY(I,J)-CYMP)**2)
      IF(U-UMIN) 33,30,30
   33 UMIN=U
   30 CONTINUE
   40 UMAX=0.0
      DO 25 K=1,2
      I=IVS+(K-1)*(NV-IVS)
      DO 23 L=1,2
      J=L+(L-1)*(NTHL-1)
      U=SQRT((VX(I,J)-CXMP)**2+(VY(I,J)-CYMP)**2)
      IF(U-UMAX) 23,23,29
   29 UMAX=U
   23 CONTINUE
   25 CONTINUE
      DIU=(UMAX-UMIN)/20.
  300 RETURN
      END
      SUBROUTINE INTEXT(VI,TI,PI)
      COMMON/ARRAY/PS,P
      COMMON/LIMITS/DTH,DTL,DIU,DIT,THMIN,UMIN
      COMMON/CON/VL,THL,NV,IVS,VC,NTHL,IVS,VS,VSP
C  INTERPOLATION=EXTRAPOLATION SUBTILE
C
      DIMENSION THL(10),VL(30,10),P(30,10),PS(30,10)
      LOGICAL JL,JHI,IL,IHI
      I=(VI-VL)/DV+1.
      DO 5 K=1,NTHL
      J=K-1
```

```
      IF(TI-THL(K)) 6,6,5
    5 CONTINUE
      J=NTHL
    6 JLO=J-1
      IHI=I.GE.NV
      JLO=J.LT.1
      JHI=J.GE.NTHL
      I=MIN0(NV-1,MAXO(1,I))
      J=MIN0(NTHL-1,MAXO(1,J))
      IE=I
      JE=J
      II=I+1
      JI=J+1
C LINEAR BIVARIATE INTERPOLATION
      QV=(VI-VL(I,J))/DV
      QT=(TI-THL(J))/(THL(JI)-THL(J))
      QUID=QV
      QUAD=QT
      IF(JLO) GO TO 30
      IF(JHI) GO TO 35
      IF(ILO) GO TO 20
      IF(IHI) GO TO 25
      PI=P(I,J)+QV*(P(II,J)-P(I,J))
      P2=P(I,JI)+QV*(P(II,JI)-P(I,JI))
      PI=PI+QT*(P2-PI)
      RETURN
C EXTRAPOLATION ENSURES THAT INTENSITIES ARE LINEAR
C  OR ZERO, AND DECREASE AS V**2 NEAR V=0
   10 IF(JLO.OR.JHI) PI=AMIN1(PL,PI)
      PI=AMAX1(0.,PI)
      RETURN
   20 PL=P(I,J)*(VI/VL(I,J))**2
      P2=P(I,JI)*(VI/VL(I,JI))**2
      PI=PL+QT*(P2-PL)
      GO TO 10
   25 IF(QT.GT..5) GO TO 27
   26 PI=P(I,J)+(1.-QV)*(P(I,J)-P(II,J))+QT*(P(II,JI)-P(II,J))
      GO TO 10
   27 PI=P(II,JI)+(1.-QV)*(P(I,JI)-P(II,JI))+(1.-QT)*(P(II,J)-P(II,JI))
      GO TO 10
   30 PI=P(I,J)+QV*(P(II,J)-P(I,J))
      PL=PI*(1.-(THL(J)-TI)/DTL)
      IF(ILO) GO TO 20
      IF(IHI) GO TO 25
      IF(QV.GT..5) GO TO 26
      PI=PI+QT*(P(I,JI)-P(I,J))
      GO TO 10
   35 PL=P(I,JI)+QV*(P(II,JI)-P(I,JI))
      PL=PI*(1.-(TI-THL(JI))/DTH)
      IF(ILO) GO TO 20
      IF(IHI) GO TO 25
      IF(QV.GT..5) GO TO 27
      PI=PI+(1.-QT)*(P(I,J)-P(I,JI))
      GO TO 10
      END
      SUBROUTINE CONTOUR
C
C  PRINTER PLOT FOR CROSS SECTION.
C
C
      COMMON/ARRAY/PE,P
      COMMON/PICTURE/V1,V2,CVMP,CVMP,COSTVMP,SINTVMP
```

```
      COMMON/BOD/VL,THL,NV,EV,VC,NTHL,IVS,VS,VSP
      COMMON/RESOLVE/VX,VY
      DIMENSION P(30,10),VX(30,10),VY(30,10),VL(30,10),THL(10),PE(30,10
      DIMENSION CHAR(21),PST(12)
C
      DATA CHAR/1H0,1H1,1H2,1H3,1H4,1H5,1H6,1H7,1H8,1H9,1HA,1HB,1HC,1HD,
     1 1HE,1HF,1HG,1HH,1HI,1HJ,1HK/,BLANK/1H /,TWO/1H*/,CM/1HS/,ONE/1H=/
      ASSIGN 200
      PMAX=0.0
      VXMAX=0.
      VXMIN=0.0
      VYMAX=0.
      VYMIN=0.0
      IF(VL-V2) 13,13,12
   12 VYMAX=V2
      GO TO 19
   13 VXMAX=VL
   19 DO 10 J=1,NTHL
      DO 10 I=IVS,NV
      IF(PMAX-P(I,J)) 1,2,2
    1 PMAX=P(I,J)
    2 IF(VXMAX-VX(I,J)) 3,4,4
    3 VXMAX=VX(I,J)
    4 IF(VXMIN-VX(I,J)) 5,6,6
    5 VXMIN=VX(I,J)
    6 IF(VYMAX-VY(I,J)) 7,8,8
    7 VYMAX=VY(I,J)
    8 IF(VYMIN-VY(I,J)) 10,10,9
    9 VYMIN=VY(I,J)
   10 CONTINUE
      AN=20./PMAX
      DO 11 J=1,NTHL
      DO 11 I=IVS,NV
   11 P(I,J)=AN*P(I,J)
      VXMIN=AMIN1(0.0,VXMIN)
      VYMIN=AMIN1(0.0,VYMIN)
      VXMAX=AMAX1(VXMAX,CXMP)
      VYMAX=AMAX1(VYMAX,CYMP)
      VXMAX=VXMAX+.1
      VYMAX=VYMAX+.1
      VXMIN=VXMIN-.1
      VYMIN=VYMIN-.1
      DVX=VXMAX-VXMIN
      DVY=VYMAX-VYMIN
C
C   DETERMINE WHICH ORIENTATION IF PRINTER PLOT GIVES GREATEST RESOLUTION
C
      IF(DVX-DVY) 22,21,21
   22 DVX=DVX/119.
      SCALE=DVX*10.
      WRITE(6,150) SCALE
      DVY=DVX/.6
      I=VYMAX/DVY
      VYMAX=I*DVY
      I=VXMIN/DVX
      VXMIN=I*DVX
      KMAX=(VYMAX-VYMIN)/DVY+1.1
      GO TO 16
   21 DVY=DVY/119.
      SCALE=DVY*10.
      WRITE(6,150) SCALE
      DVX=DVY/.6
```

```
      I=VYMAX/DVY
      VYMAX=I*DVY
      I=VXMIN/DVX
      VXMIN=I*DVX
      KMAX=(VXMAX-VXMIN)/DVX+1.1
   14 DY=.5*DVY
      DX=.5*DVX
      IF(DVX .GT. DVY) GO TO 50
      DO 30 K=1,KMAX
      VYI=VYMAX-FLOAT(K-1)*DVY
      DO 20 L=1,120
      VXI=VXMIN+FLOAT(L-1)*DVX
      IF(ABS(VYI) .LT. DY .AND. VXI .LT. V1 .AND. VXI .GE. 0. .AND. VXMA
     1X .GE. V1) GO TO 17
      IF(ABS(VXI) .LT. DX .AND. VYI .LT. V2 .AND. VYI .GE. 0. .AND. VYMA
     1X .GE. V2) GO TO 16
      IF(ABS(CXMP-VXI) .LT. DX .AND. ABS(CYMP-VYI) .LT. DY) GO TO 18
      VI=SQRT(VXI*VXI+VYI*VYI)
      IF(VI .LT. VSP .OR. VI .GT. VL(NV,1)) GO TO 15
      TI=ATAN2(VYI,VXI)/.0174533
      IF(TI .LT. THL(1) .OR. TI .GT. THL(NTHL)) GO TO 15
      CALL INTEXT(VI,TI,PI)
      IP=PI
      PRT(L)=CHAR(IP+1)
      GO TO 20
   15 PRT(L)=BLANK
      GO TO 20
   16 PRT(L)=TWO
      GO TO 20
   17 PRT(L)=ONE
      GO TO 20
   18 PRT(L)=CM
   20 CONTINUE
      WRITE(6,133) (PRT(L),L=1,120)
   30 CONTINUE
      GO TO 330
   50 DO 80 K=1,KMAX
      VXI=VXMAX-FLOAT(K-1)*DVX
      DO 70 L=1,120
      VYI=VYMIN+FLOAT(L-1)*DVY
      IF(ABS(VYI) .LT. DY .AND. VXI .LT. V1 .AND. VXI .GE. 0. .AND. VXMA
     1X .GE. V1) GO TO 67
      IF(ABS(VXI) .LT. DX .AND. VYI .LT. V2 .AND. VYI .GE. 0. .AND. VYMA
     1X .GE. V2) GO TO 66
      IF(ABS(CXMP-VXI) .LT. DX .AND. ABS(CYMP-VYI) .LT. DY) GO TO 68
      VI=SQRT(VXI*VXI+VYI*VYI)
      IF(VI .LT. VSP .OR. VI .GT. VL(NV,1)) GO TO 65
      TI=ATAN2(VYI,VXI)/.0174533
      IF(TI .LT. THL(1) .OR. TI .GT. THL(NTHL)) GO TO 65
      CALL INTEXT(VI,TI,PI)
      IP=PI
      PRT(L)=CHAR(IP+1)
      GO TO 70
   65 PRT(L)=BLANK
      GO TO 70
   67 PRT(L)=TWO
      GO TO 70
   66 PRT(L)=ONE
      GO TO 70
   68 PRT(L)=CM
   70 CONTINUE
      WRITE(6,100) (PRT(L),L=1,120)
```

```
   80 CONTINUE
  300 WRITE(6,101) VXMIN,VXMAX,DVX,VYMIN,VYMAX,DVY,PMAX
      RETURN
  100 FORMAT(120A1)
  101 FORMAT(1H0,5X5HVXMIN,5X5HVXMAX7X3HDVX5X5HVYMIN5X5HVYMAX7X3HDVY6X4HPM
     1AX/8F10.3)
  150 FORMAT(1H ,13H  ONE INCH = ,F8.2,15H X 10000 CM/SEC/1H0)
  200 FORMAT(1H1,* DIFFERENTIAL CROSS SECTION*)
      END
C
C
      SUBROUTINE CMCS
C
C   CALCULATES C.M. VELOCITY AVERAGED ANGULAR DISTRIBUTION  AND ANGLE
C   AVERAGED VELOCITY DISTRIBUTION ONLY FOR RANGE OF C.M. VELOCITY AND
C   ANGLE SPACE EXPLORED BY EXPERIMENTAL DATA
C
      COMMON/ARRAY/PE,P
      COMMON/LIMITS/OTH,OTL,DIU,DIT,THMIN,UMIN
      COMMON/DDD/VL,THL,NV,DV,VO,NTHL,IVS,VS,VSP
      COMMON/PICTURE/V1,V2,CXMP,CYMP,COSTVMP,SINTVMP
      COMMON/RESOLVE/VX,VY
      DIMENSION PU(20),PT(20),P(30,10),PE(30,10),THL(10),VX(30,10),VY(30
     1,10),VL(30,10)
C
      DO 21 IU=1,20
      PT(IU)=0.
   21 PU(IU)=0.
      TH=THMIN-DIT
      DO 30 IT=1,20
      TH=TH+DIT
      S=SIN(TH)
      C=COS(TH)
      U=UMIN-DIU
      DO 29 IU=1,20
      U=U+DIU
      UX=U*C
      UY=U*S
      VXI=UX*COSTVMP+UY*SINTVMP+CXMP
      VYI=-UX*SINTVMP+UY*COSTVMP+CYMP
      VI=SQRT(VXI**2+VYI**2)
      IF(VI .LT. VS .OR. VI .GT. VL(NV,1)) GO TO 29
      TI=ATAN2(VYI,VXI)/.017+5329
      IF(TI .LT. THL(1) .OR. TI .GT. THL(NTHL)) GO TO 29
      CALL INTERT(VI,TI,PI)
      PT(IT)=PT(IT)+PI
      PU(IU)=PU(IU)+PI
   29 CONTINUE
   30 CONTINUE
      PTM=1.0
      PUM=1.0
      DO 50 IU=1,20
      IF(PTM-PT(IU)) 35,40,40
   35 PTM=PT(IU)
   40 IF(PUM-PU(IU)) 45,50,50
   45 PUM=PU(IU)
   50 CONTINUE
      U=UMIN-DIU
      TH=THMIN-DIT
      WRITE(6,100)
C
      DO 60 IU=1,20
```

```
      U=U+DIU
      TH=TH+DIT
      PTN=PT(IU)/PTM
      PUN=PU(IU)/PUM
      WRITE(6,101) U,PU(IU),PUN,TH/0.0174533,PT(IU),PTN
   60 CONTINUE
  100 FORMAT(1H0,14X,*VELOCITY DISTRIBUTION*,21X,*ANGULAR DISTRIBUTION*/
     1 19X1HU8X4HPU)5X4HPUN8X2HTH7X5HPT(TH)6X4HNORM)
  101 FORMAT(2(10X,F10.3,2X,F10.2,F10.3))
      RETURN
      END
```

CL + HR2 - 10PERCENT CL2/AR - 350A

BEAM INPUT PARAMETERS

	PRIMARY	SECONDARY
MASS	35.00	160.00
TEMPERATURE	1481.8	342.6
GAMMA	1.67	1.40
MACH NUMBER	4.29	9.43
DISTRIBUTION TYPE	NOZZLE	NOZZLE
NO. VELOCITIES AVERAGED	5	3

NUMBER OF LAB ANGLES = 4

NUMBER OF VELOCITIES AT EACH ANGLE = 14

VELOCITY INCREMENT = .50

FIRST VELOCITY = 3.00

ANALYSIS CUTOFF VELOCITY = 3.00

CONTOUR PLOT CUTOFF VELOCITY = 3.00

NUMBER OF ITERATIONS REQUESTED IS 5

V1	F(V1)	V2	F(V2)	GAMMA	F(G)	F(V1,V2,G)	THC	EREL
9.53	.27	3.48	1.00	89.00	.50	.0085	58.32	3.49
9.53	.27	3.84	.49	89.00	.50	.0063	60.73	3.58
11.26	.72	3.12	.49	89.00	.50	.0131	51.09	4.64
11.26	.72	3.48	1.00	89.00	.50	.0266	54.02	4.72
11.26	.72	3.84	.49	89.00	.50	.0133	56.80	4.80
12.99	1.00	3.12	.49	89.00	.50	.0207	47.08	4.88
12.99	1.00	3.48	1.00	89.00	.50	.0422	50.13	4.15
12.99	1.00	3.84	.49	89.00	.50	.0210	52.83	4.24
14.73	.72	3.12	.49	89.00	.50	.0169	43.56	7.72
14.73	.72	3.48	1.00	89.00	.50	.0343	46.64	7.83
14.73	.72	3.84	.49	89.00	.50	.0171	49.40	7.88
16.46	.27	3.12	.49	89.00	.50	.0071	40.44	9.57
16.46	.27	3.48	1.00	89.00	.50	.0145	43.51	9.64
16.46	.27	3.84	.49	89.00	.50	.0072	46.29	9.73
9.53	.27	3.12	.49	90.00	1.00	.0083	56.22	3.45
9.53	.27	3.48	1.00	90.00	1.00	.0171	59.06	3.53
9.53	.27	3.84	.49	90.00	1.00	.0086	61.50	3.62
11.26	.72	3.12	.49	90.00	1.00	.0262	51.67	4.68
11.26	.72	3.48	1.00	90.00	1.00	.0535	54.68	4.77
11.26	.72	3.84	.49	90.00	1.00	.0267	57.30	4.86
12.99	1.00	3.12	.49	90.00	1.00	.0416	47.62	6.13
12.99	1.00	3.48	1.00	90.00	1.00	.0848	50.73	6.21
12.99	1.00	3.84	.49	90.00	1.00	.0423	53.47	6.30
14.73	.72	3.12	.49	90.00	1.00	.0339	44.04	7.78
14.73	.72	3.48	1.00	90.00	1.00	.0689	47.18	7.86
14.73	.72	3.84	.49	90.00	1.00	.0343	49.99	7.95
16.46	.27	3.12	.49	90.00	1.00	.0143	40.87	9.63
16.46	.27	3.48	1.00	90.00	1.00	.0291	43.99	9.71
16.46	.27	3.84	.49	90.00	1.00	.0145	46.82	9.80
9.53	.27	3.48	1.00	91.00	.50	.0086	59.80	3.57
9.53	.27	3.84	.49	91.00	.50	.0043	62.27	3.66
11.26	.72	3.12	.49	91.00	.50	.0132	52.28	4.73
11.26	.72	3.48	1.00	91.00	.50	.0269	55.35	4.81
11.26	.72	3.84	.49	91.00	.50	.0134	58.01	4.91

12.99	1.00	3.12	.49	91.00	.50	.0209	48.17	6.18		
12.99	1.00	3.46	1.00	91.00	.50	.0426	51.33	6.26		
12.99	1.00	3.84	.49	91.00	.50	.0212	54.12	6.36		
14.73	.72	3.12	.49	91.00	.50	.0170	44.52	7.83		
14.73	.72	3.48	1.00	91.00	.50	.0346	47.72	7.92		
14.73	.72	3.84	.49	91.00	.50	.0172	50.57	8.02		
16.46	.27	3.12	.49	91.00	.50	.0072	41.29	9.69		
16.46	.27	3.48	1.00	91.00	.50	.0146	44.48	9.78		
16.46	.27	3.84	.49	91.00	.50	.0073	47.36	9.88		
13.40		3.48					49.89	6.58	(CANONICAL).	

43 NEWTON DIAGRAMS

ITERATION NUMBER = 0 ERROR = 59.32

LAB ANGLE		10.0			20.0				30.0		
VEL	EXPT	FOLD	UNFOLD	VEL	EXPT	FOLD	UNFOLD	VEL	EXPT	FOLD	UNFOLD
3.00	.00	2.87	.00	3.00	.00	9.30	.00	3.00	.00	24.03	.00
3.50	.39	27.51	.09	3.50	.30	72.51	.33	3.50	35.36	129.94	9.82
4.00	.00	121.55	.00	4.00	231.96	258.11	208.46	4.00	390.35	395.26	428.93
4.50	160.23	292.87	87.66	4.50	548.37	539.44	557.44	4.50	756.64	623.31	913.66
5.00	356.27	508.74	249.50	5.00	847.10	830.07	864.48	5.00	1032.58	854.00	1248.50
5.50	526.86	718.85	386.15	5.50	1040.78	1064.79	1017.31	5.50	1057.52	995.01	1123.98
6.00	690.43	893.31	533.63	6.00	1126.84	1204.20	1053.14	6.00	926.78	1020.47	841.69
6.50	775.69	1016.19	592.11	6.50	1362.50	1247.22	905.14	6.50	748.95	956.66	580.34
7.00	777.46	1078.30	560.56	7.00	890.09	1204.16	657.94	7.00	570.89	843.60	386.34
7.50	716.43	1068.11	480.54	7.50	649.84	1090.06	387.40	7.50	393.35	709.26	218.15
8.00	550.28	996.23	303.95	8.00	437.27	923.47	207.73	8.00	252.03	586.58	112.11
8.50	378.15	875.22	163.38	8.50	250.22	725.02	86.36	8.50	132.69	427.33	41.20
9.00	240.19	716.82	86.55	9.00	112.01	532.32	23.57	9.00	45.16	302.65	8.74
9.50	149.33	544.55	40.95	9.50	.00	359.16	.00	9.50	.00	194.26	.00

LAB ANGLE		40.0								
VEL	EXPT	FOLD	UNFOLD	VEL	EXPT	FOLD	UNFOLD	VEL	EXPT	FOLD	UNFOLD
3.00	.00	35.55	.00								
3.50	140.08	143.13	137.09								
4.00	404.81	307.69	532.58								
4.50	522.27	440.41	619.35								
5.00	529.95	497.92	564.04								
5.50	479.57	493.76	468.63								
6.00	423.22	454.33	388.92								
6.50	395.36	416.97	302.85								
7.00	282.63	376.40	212.22								
7.50	239.87	330.69	133.19								
8.00	147.69	276.07	79.01								
8.50	97.72	222.03	43.01								
9.00	58.57	173.21	20.15								
9.50	.00	124.59	.00								

56 DATA POINTS

LAB ANGULAR DISTRIBUTION

THETA	EXPT	CALC
10.0	.667	.827
20.0	1.000	1.000
30.0	.942	.845
40.0	.567	.474

ITERATION NUMBER = 1 ERROR = 23.41

LAB ANGLE 10.0 20.0 30.0

VEL	EXPT	FOLD	UNFOLD	VEL	EXPT	FOLD	UNFOLD	VEL	EXPT	FOLD	UNFOLD
3.30	.90	2.43	.90	3.30	.00	6.15	.00	3.00	.00	20.01	.00
3.53	.00	24.57	.00	3.50	.00	66.07	.00	3.50	35.36	134.18	2.54
4.00	.00	111.26	.00	4.00	231.96	265.19	182.34	4.00	393.35	411.12	407.26
4.53	160.23	271.96	51.65	4.50	548.37	586.51	521.19	4.50	754.64	746.30	923.85
5.00	356.27	473.77	187.02	5.00	847.10	914.40	800.85	5.00	1032.58	1012.46	1273.31
5.50	526.86	659.02	308.71	5.50	1040.78	1139.58	929.11	5.50	1057.52	1125.49	1056.08
6.00	690.43	797.14	462.19	6.00	1126.14	1216.40	974.99	6.00	926.78	1060.34	735.47
6.50	775.69	876.73	523.87	6.50	1062.50	1174.59	818.76	6.50	748.95	894.49	490.96
7.00	777.46	890.72	469.28	7.00	890.39	1050.49	557.48	7.00	579.89	706.20	312.31
7.53	716.43	829.42	415.38	7.50	669.84	867.18	290.31	7.50	393.35	529.98	161.91
8.00	550.29	715.53	233.76	8.00	431.27	650.37	139.53	8.00	252.03	378.49	75.65
8.50	378.15	572.22	107.97	8.50	250.22	442.53	48.83	8.50	132.69	242.99	22.50
9.00	246.19	415.72	50.37	9.00	112.01	272.56	9.69	9.00	45.16	145.17	2.10
9.50	149.33	273.44	22.61	9.50	.00	150.88	.00	9.50	.00	75.86	.00

LAB ANGLE 40.0

VEL	EXPT	FOLD	UNFOLD	VEL	EXPT	FOLD	UNFOLD	VEL	EXPT	FOLD	UNFOLD
3.00	.00	35.22	.00								
3.50	140.08	1[illegible].08	117.04								
4.00	434.81	362.88	563.08								
4.50	822.27	531.64	608.43								
5.00	529.95	549.75	543.73								
5.50	479.57	486.82	481.65								
6.00	420.22	428.31	381.67								
6.50	355.36	384.49	279.91								
7.00	282.63	331.52	180.92								
7.50	204.87	270.12	103.48								
8.00	147.69	221.07	58.03								
8.50	97.72	170.72	29.87								
9.00	58.57	93.44	12.63								
9.50	.00	58.59	.00								

56 DATA POINTS

LAB ANGULAR DISTRIBUTION

THETA	EXPT	CALC
10.0	.867	.729
20.0	1.000	1.000
30.0	.942	.909
40.0	.867	.817

ITERATION NUMBER = 2 ERROR = 9.91

LAB ANGLE 10.0 20.0 30.0

VEL	EXPT	FOLD	UNFOLD	VEL	EXPT	FOLD	UNFOLD	VEL	EXPT	FOLD	UNFOLD
3.30	.33	2.39	.33	3.30	.00	4.85	.00	3.00	.00	16.85	.00
3.50	.00	21.53	.00	3.50	.00	58.23	.00	3.50	35.36	129.41	1.71
4.00	.00	98.62	.00	4.00	231.96	248.41	173.27	4.00	390.35	405.86	391.89
4.53	160.23	242.85	34.08	4.50	548.37	566.29	506.49	4.50	754.64	749.45	930.25
5.00	356.27	423.50	157.84	5.00	847.10	887.06	764.78	5.00	1032.58	1016.50	1293.45
5.50	526.86	595.83	277.64	5.50	1040.78	1098.09	887.08	5.50	1057.52	1139.01	1097.05
6.00	690.43	706.94	451.39	6.00	1126.14	1134.52	967.79	6.00	926.78	1003.04	879.74
6.50	775.69	781.41	520.03	6.50	1062.50	1072.27	811.30	6.50	748.95	807.49	459.35
7.00	777.46	794.70	479.66	7.00	890.39	942.30	526.59	7.00	579.89	612.04	291.32
7.53	716.43	730.45	407.12	7.50	669.84	756.17	249.49	7.50	393.35	442.89	143.80
8.00	550.29	614.83	209.21	8.00	437.27	540.35	112.91	8.00	252.03	299.06	63.75
8.50	378.15	475.38	85.89	8.50	250.22	341.84	35.74	8.50	132.69	183.32	16.28

9.00	246.19	328.39	37.57	9.00	112.01	192.62	5.63	9.00	45.16	101.84	.93
9.50	149.51	197.35	17.14	9.50	.00	96.88	.00	9.50	.00	48.50	.00

LAB ANGLE 40.0

VEL	EXPT	FOLD	UNFOLD	VEL	EXPT	FOLD	UNFOLD	VEL	EXPT	FOLD	UNFOLD
3.00	.00	31.69	.00								
3.50	143.04	183.30	100.40								
4.00	434.81	401.33	568.39								
4.50	522.2-	545.96	582.35								
5.00	529.95	540.90	533.22								
5.50	478.57	465.68	475.42								
6.00	423.22	424.86	377.41								
6.50	355.36	385.94	257.73								
7.00	282.63	321.11	159.24								
7.50	239.87	245.14	88.59								
8.00	147.69	169.78	50.48								
8.50	97.72	111.13	26.27								
9.00	58.57	73.36	13.56								
9.50	.00	41.92	.00								

50 DATA POINTS

LAB ANGULAR DISTRIBUTION

THETA	EXPT	CALC
13.0	.667	.699
20.0	1.000	1.000
30.0	.942	.937
40.0	.567	.535

ITERATION NUMBER = 3 ERROR = 6.61

LAB ANGLE 10.0 20.0 30.0

VEL	EXPT	FOLD	UNFOLD	VEL	EXPT	FOLD	UNFOLD	VEL	EXPT	FOLD	UNFOLD
3.00	.00	1.94	.00	3.00	.00	4.39	.00	3.00	.00	14.95	.00
3.50	.00	22.15	.00	3.50	.00	36.36	.00	3.50	35.36	118.82	.21
4.00	.00	92.97	.00	4.00	231.96	239.81	166.69	4.00	393.35	398.10	384.27
4.50	160.23	229.30	23.81	4.50	548.37	553.39	501.90	4.50	734.66	745.89	741.16
5.00	358.27	399.23	143.85	5.00	847.13	874.43	740.88	5.00	1032.58	1016.53	1313.88
5.50	526.86	551.28	265.34	5.50	1040.78	1065.37	866.61	5.50	1057.52	1099.97	928.19
6.00	690.43	671.01	464.46	6.00	1126.14	1096.71	993.76	6.00	926.78	970.67	649.01
6.50	725.69	756.88	532.95	6.50	1062.50	1036.83	831.39	6.50	748.95	762.25	447.40
7.00	777.46	780.50	476.74	7.00	890.09	935.74	511.84	7.00	570.89	569.80	291.88
7.50	716.43	719.67	407.66	7.50	649.84	728.87	222.43	7.50	389.55	409.91	137.99
8.00	553.28	593.77	193.89	8.00	437.27	505.46	97.68	8.00	252.03	273.78	58.69
8.50	378.15	450.15	72.15	8.50	250.22	304.43	29.38	8.50	132.69	163.35	13.23
9.00	246.19	301.36	30.73	9.00	112.31	161.78	3.93	9.00	45.16	87.44	.48
9.50	149.33	171.01	14.96	9.50	.00	77.01	.00	9.50	.00	39.40	.00

LAB ANGLE 40.0

VEL	EXPT	FOLD	UNFOLD	VEL	EXPT	FOLD	UNFOLD	VEL	EXPT	FOLD	UNFOLD
3.00	.00	28.08	.00								
3.50	140.08	156.96	89.84								
4.00	434.81	397.45	578.92								
4.50	522.27	534.94	588.26								
5.00	529.95	522.35	539.94								
5.50	479.57	459.51	496.18								
6.00	420.22	437.85	362.21								
6.50	355.36	389.65	234.05								
7.00	282.63	336.41	146.89								

7.50	209.87	220.88	84.18
8.00	147.69	147.63	53.53
8.	97.72	95.72	26.81
9.	58.57	62.68	13.19
9.50	.00	36.01	.00

56 DATA POINTS

LAB ANGULAR DISTRIBUTION

THETA	EXPT	CALC
10.0	.667	.692
20.0	1.000	1.000
30.0	.742	.941
40.0	.567	.559

ITERATION NUMBER = 4 ERROR = 6.18

LAB ANGLE		10.0			20.0			30.0		
VEL	EXPT	FOLD	UNFOLD	VEL	EXPT	FOLD	UNFOLD	VEL	EXPT	FOLD	UNFOLD
3.00	.00	1.88	.00	3.00	.00	4.21	.00	3.00	.00	13.91	.00
3.50	.00	19.93	.00	3.50	.00	54.69	.00	3.50	35.36	115.61	.07
4.00	.33	90.23	.00	4.00	231.96	236.34	181.[illegible]	4.00	390.35	396.53	378.28
4.50	160.23	222.67	17.13	4.50	568.37	550.30	500.14	4.50	754.64	749.27	947.91
5.00	356.27	386.24	129.92	5.00	847.10	870.88	720.65	5.00	1032.58	1023.60	1325.40
5.50	926.86	933.35	262.11	5.50	1040.78	1053.38	856.20	5.50	1057.52	1099.38	931.32
6.00	690.43	658.26	487.16	6.00	1126.14	1080.02	1036.20	6.00	926.78	850.99	632.48
6.50	775.69	751.23	543.08	6.50	1062.50	1037.30	855.96	6.50	748.95	735.51	455.57
7.00	777.46	795.43	405.57	7.00	890.09	922.54	493.84	7.00	570.89	550.58	302.84
7.50	716.43	723.45	403.70	7.50	645.86	730.27	197.94	7.50	393.35	400.75	135.44
8.00	550.28	589.49	180.99	8.00	437.27	492.32	86.76	8.00	252.03	268.59	55.07
8.50	378.15	438.50	64.22	8.50	250.22	283.77	25.90	8.50	132.69	157.74	11.13
9.00	246.19	286.42	26.41	9.00	112.01	144.07	3.03	9.00	45.16	82.32	.26
9.50	149.33	155.77	14.34	9.50	.00	66.37	.00	9.50	.00	36.09	.00

LAB ANGLE		40.0								
VEL	EXPT	FOLD	UNFOLD	VEL	EXPT	FOLD	UNFOLD	VEL	EXPT	FOLD	UNFOLD
3.00	.00	.33	.00							
3.50	140.38	1 .22	82.56							
4.00	404.81	40.97	575.85							
4.50	522.27	538.55	551.08							
5.00	529.95	520.22	553.34							
5.50	479.57	469.66	506.65							
6.00	420.22	454.37	334.99							
6.50	355.36	353.36	218.35							
7.00	282.63	283.95	146.20							
7.50	209.87	199.35	88.62							
8.00	147.69	135.52	55.34							
8.50	97.72	91.66	26.59							
9.00	58.57	62.33	9.90							
9.50	.00	37.25	.00							

56 DATA POINTS

LAB ANGULAR DISTRIBUTION

THETA	EXPT	CALC
10.0	.667	.693
20.0	1.000	1.000
30.0	.742	.941
40.0	.567	.564

UNFOLDED CM CROSS SECTION

VELOCITY DISTRIBUTION			ANGULAR DISTRIBUTION		
U	P(U)	NORM	TH	P(TH)	NORM
.665	0	0	-82.004	0	0
.985	119.15	.074	-75.490	0	0
1.304	308.71	.192	-68.976	1.60	.000
1.623	574.95	.358	-62.462	2.14	.001
1.943	934.01	.581	-55.948	2.62	.001
2.262	1230.86	.766	-49.434	3.39	.001
2.582	1478.66	.920	-42.920	54.36	.016
2.901	1529.85	.952	-36.406	152.87	.046
3.221	1516.68	.944	-29.892	326.97	.099
3.540	1526.47	.950	-23.378	652.32	.197
3.860	1606.39	1.000	-16.864	1115.98	.337
4.179	1588.62	.989	-10.350	1951.60	.589
4.499	1429.95	.890	-3.837	3234.57	.977
4.818	1301.55	.810	2.677	3312.19	1.000
5.138	899.89	.560	9.191	2607.55	.787
5.457	725.93	.452	15.705	1875.17	.566
5.777	595.36	.371	22.219	1300.98	.393
6.096	509.22	.317	28.733	896.47	.271
6.416	220.41	.137	35.247	548.60	.166
6.735	146.91	.091	41.761	204.68	.062

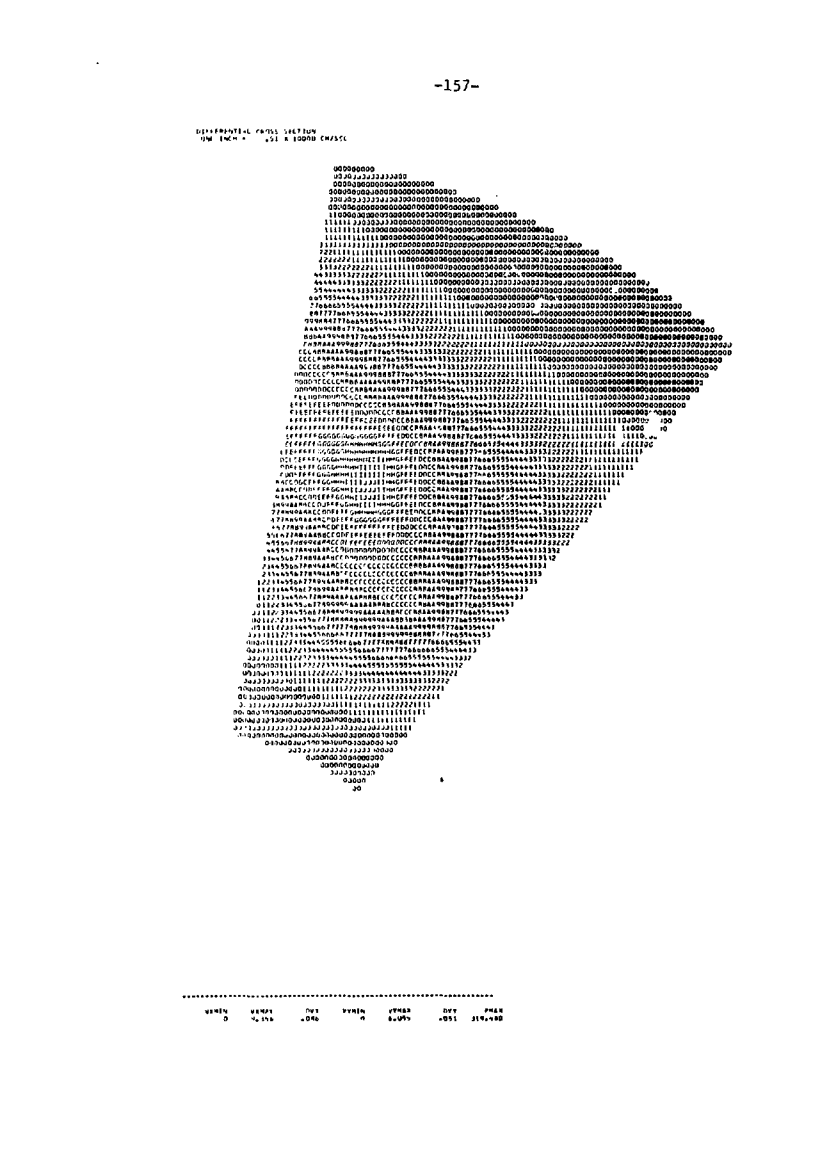

D. Program Kelvin

Information on the velocity distributions of the two reactant beams is required to carry out the iterative deconvolution of $\bar{I}_{LAB}(\theta, v)$ to obtain $I_{c.m.}(\theta, u)$. In order to reduce the requisite amount of data to be input to program RECON, the velocity distribution of a nozzle beam is characterized parametrically by γ, M, and α_o, the ratio of specific heats, the beam Mach number, and the most probable velocity in the nozzle source. As can be seen from equation (6) of chapter II, these parameters uniquely define a nozzle beam velocity distribution. These parameters are obtained by fitting γ, M, and α_o to the observed time-of-flight spectrum of each reactant beam, measured as explained in chapter II. This fitting procedure is carried out by program KELVIN.

The input for KELVIN consists mainly of an array, N(n), of intensities (proportional to number density), versus channel number, n, as directly obtained from the output of a multichannel scaler which is used to record the TOF distribution. Since the flight time t is given by $t = (n-.5)\cdot w$, where w is the time width of the scaler channel, the input data are implicitly a function of time.

Values for γ, which is assumed well known, and for M, which is an initial guess, are input, while an initial guess for α_o is generated by the program itself. These parameters are used to calculate a TOF spectrum averaged over the finite bandpass function of the TOF apparatus. This calculated distribution is compared with the observed TOF spectrum and corrections to α_o and M are generated. This procedure is iterated until the agreement between calculated and observed spectra is optimized.

KELVIN will perform rudimentary smoothing of the input data by averaging over a variable number of successive channels. However, this usually proves unnecessary due to the high quality of the TOF spectra commonly obtained. Provision is also made for subtracting from the input data any constant, i.e. flight time independent, background which may be present.

The major output of course are the optimized values of α_o and M, MOST PROBABLE VELOCITY and MACH NUMBER in the output. The program also prints out the input data, N(n), headed RAW DATA or OBSERVED, as well as the input data minus the constant background, headed NORMALIZED, and the input data smoothed over a number of successive channels, headed SMOOTHED. The best fit calculated TOF data, headed CALCULATED, and the best fit TOF data with all instrumental averaging removed, headed DECONVOLUTED, are also output. This last TOF distribution is of course the physically significant one.

Also given as output is the source "temperature". For a nozzle beam of a pure gas this is the actual physically measurable nozzle temperature. For a "seeded" beam it is the temperature at which the nozzle would have to be operated to give this velocity distribution if the beam were a pure one consisting solely of the species whose TOF spectrum was input.

Several different TOF spectra can be fit in a single run of the program by simply stacking data for different spectra.

A description of the input variables, a listing, and a sample output of KELVIN follow.

Program KELVIN Input Variables

Variable	Description
TITLE	Heading for all output.
MASS	Mass of particle, in a. m. u., whose TOF spectrum this is. MASS = 0.0 stops program execution.
TEMP	Estimated source "temperature" as explained in program description. This is for user reference only, it is not used for computation.
GAM	The ratio of specific heats, γ.
CHAN	The multiscaler channel width, in microseconds.
LMID	The TOF flight path length, in centimeters.
DL	The ionizer length, in centimeters.
BCHAN, ECHAN	The number of the first and last multiscaler channels for which TOF data are to be input.
ACHAN	The number of channels (always odd) over which the input data are to be averaged for smoothing.
EION, LION	The ion energy, in electron volts, and ion flight length in centimeters. Needed to correct flight times for the time required for the ions to traverse the length, LION, of the detector.
OFFSET	The time, in units of multiscaler channel width, by which the multiscaler zero of time lags behind the true zero of time. The value of this parameter is determined by calibration of the TOF apparatus. This parameter corrects the N(n) = N(t') input data, where t' is the observed flight time, to give the N(t) data, where t is the true flight time. $t = t' +$ OFFSET·CHAN.
DC	Magnitude of the constant (i.e. flight time invariant) background which is to be subtracted from the TOF data.
HZ	The rotational speed of the TOF wheel in cycles per second.

Program KELVIN Input Variables (Cont'd)

Variable	Description
DIA	The TOF wheel diameter in centimeters.
SHUTTER	The slot width of the TOF wheel in millimeters.
DETECT	The diameter of the detector aperture in millimeters.
EXPT(I), I = BCHAN, ECHAN	The observed TOF intensity in channel I, N(n).

```
      PROGRAM KELVIN(INPUT,OUTPUT,TAPE5=INPUT,TAPE6=OUTPUT)
      COMMON/PAR/CHAN,LMID,DL,R,S,GAM,BCHAN,ECHAN,NCHAN
      COMMON/WHEEL/SHUTTER,DETECT
      DIMENSION EXPT(255),EXPTI(255),EXPTN(255),SIGCAL(255),
     CSIGCA1(255),SIGCA2(255),SIGCA3(255),SIGCA4(255),TITLE(20),WMACH(10
     C),WALPHA(10),SIGDEC(255),WEIGHT(255)
      REAL MASS,MACH,LMID,L,LION,MID
      INTEGER BCHAN,ECHAN,ACHAN,BC,EC
      CALL GAUSS
C
C     INPUT DATA
C
 1003 READ(5,102) TITLE
  102 FORMAT(20A4)
C
C     ZERO OUT THE ARRAYS
C
      CALL ZERO(EXPT,EXPTI,EXPTN)
      READ(5,100) MASS,TEMP,GAM,CHAN,LMID,DL,BCHAN,ECHAN,ACHAN
  100 FORMAT(6F10.5,3I4)
      IF(MASS .EQ. 0.0) STOP
      BC=BCHAN
      EC=ECHAN
  130 READ(5,100) EION,LION,OFFSET,DC
C
C     CORRECT FLIGHT TIMES FOR THE ION TRANSIT TIME
C
      CHT=LION/SQRT(EION/MASS)*.7198/CHAN
      ICHT=INT(OFFSET-CHT+SIGN(.5,(OFFSET-CHT)))
      BCHAN=BCHAN+ICHT
      ECHAN=ECHAN+ICHT
      NCHAN=ECHAN-BCHAN+1
  150 READ(5,103) MACH
  103 FORMAT(F10.3,I5)
      READ(5,100)HZ,DIA,SHUTTER,DETECT
      READ(5,101) (EXPTI(I), I=BCHAN,ECHAN)
  101 FORMAT(8F10.1)
  140 WRITE(6,204) TITLE
  204 FORMAT(1HI,20A4)
C
C     OUTPUT DATA
C
      WRITE(6,200) MASS,TEMP,GAM
  200 FORMAT(*0   MASS =*,F7.3,*; TEMP =*,F7.1,*; GAMMA =*,F4.2)
      WRITE(6,201) CHAN,BC,EC,LMID,DL
  201 FORMAT(*    CHANNEL WIDTH =*,F4.1,* MICROSECONDS; BEGINNING CHANNEL
     1 =*,I3,*, ENDING CHANNEL =*,I3,*; FLIGHT LENGTH =*,F5.2,* CM; IONI
     1ZER LENGTH =*,F5.2,* CM.*)
      WRITE(6,104) EION,LION,CHT,OFFSET
  104 FORMAT(3X,*ION ENERGY=  *,F4.1,2X,*EV; ION PATH LENGTH=  *,F4.1,*
     1 CM;  ION FLIGHT TIME OFFSET= *,F3.1,* CHANNEL(S); ZERO CHANNEL OF
     2FSET = *,F4.1,* CHANNEL(S)*)
      WRITE(6,211)HZ,DIA,SHUTTER,DETECT
  211 FORMAT(*    WHEEL FREQ. =*,F4.0,* HZ; WHEEL DIAMETER =*,F4.1,* CM;
     1SLOT WIDTH = *,F4.2,* MM; DETECTOR APERTURE =*,F4.2,* MM*)
      WRITE(6,202) MACH
  202 FORMAT(*    TRIAL MACH NUMBER =*,F4.1)
      IFIT=10
      SHUTTER=SHUTTER/(31.4159*DIA*HZ)/(CHAN*1.0E-06)
      DETECT=DETECT/(31.4159*DIA*HZ)/(CHAN*1.0E-06)
      IF(DETECT .LT. SHUTTER) GO TO 210
```

```
      SAVER=DETECT
      DETECT=SHUTTER
      SHUTTER=SAVER
C
C     SUBTRACT CONSTANT BACKGROUND FROM THE DATA
C
  210 DO 1004 I=BCHAN,ECHAN
      EXPTN(I)=EXPT(I)-DC
      EXPT(I)=EXPTN(I)
      WEIGHT(I)=SQRT(EXPT(I))
 1004 CONTINUE
C
C     AVERAGE DATA OVER THE SELECTED NUMBER OF CHANNELS
C
      INC=ACHAN/2
      IED=ECHAN-ACHAN
      DO 1006 I=BCHAN,IED
      RUN=0.0
      DO 1007 J=1,ACHAN
      RUN=RUN+EXPTN(I+J-1)
 1007 CONTINUE
      EXPT(I+INC)=RUN/FLOAT(ACHAN)
 1006 CONTINUE
      WRITE(6,214)
  214 FORMAT(1H0,6X,*CHANNEL*,3X,*RAW DATA*,3X,*NORMALIZED*,3X,*SMOOTHED
     1*)
      DO 1008 I=BCHAN,ECHAN
      WRITE(6,215) I,EXPTI(I),EXPTN(I),EXPT(I)
 1008 CONTINUE
  215 FORMAT(1H ,9X,I3,3X,F10.2,2X,F10.2,2X,F10.2)
C
C     GENERATE ESTIMATE OF ALPHA
C
      CALL BIG(EXPT,MAX2)
      V=LMID/(CHAN*MAX2*.01)
      T=1.195*MASS*V**2/(17.5-7.5*GAM)
      ALPHA=12848.5*SQRT(T/MASS)
C
C     FITTING ROUTINE
C
      CALL VELO(MACH,ALPHA,SIGCAL)
      CALL FIT(SIGCAL,EXPT)
 1012 DO 1000 JCYC=1,IFIT
      DALPHA=.10*ALPHA
      DMACH=0.1*MACH
      CALL VELO(MACH,ALPHA+DALPHA,SIGCA1)
      CALL FIT(SIGCA1,EXPT)
      CALL VELO(MACH,ALPHA-DALPHA,SIGCA2)
      CALL FIT(SIGCA2,EXPT)
      CALL VELO(MACH+DMACH,ALPHA,SIGCA3)
      CALL FIT(SIGCA3,EXPT)
      CALL VELO(MACH-DMACH,ALPHA,SIGCA4)
      CALL FIT(SIGCA4,EXPT)
      GA=0.
      GM=0.
      AAA=0.
      AMM=0.
      AAM=0.
      SUM=0.
      SUM2=0.
      SUM4=0.
      SUMY=0.
```

```
      SUMYY=0.
      SMTRM=0.0
      DO 1001 I=BCHAN,ECHAN
      DFDA=(SIGCA1(I)-SIGCA2(I))/(2.*DALPHA)
      DFDM=(SIGCA3(I)-SIGCA4(I))/(2.*DMACH)
      DFDAA=(SIGCA1(I)+SIGCA2(I)-2.*SIGCAL(I))/(DALPHA*DALPHA)
      DFDMM=(SIGCA3(I)+SIGCA4(I)-2.*SIGCAL(I))/(DMACH*DMACH)
      WE=WEIGHT(I)
      TERM=EXPT(I)-SIGCAL(I)
       GA=GA+TERM*DFDA*WE
       GM=GM+TERM*DFDM*WE
      AAA=AAA+DFDA*DFDA*WE
      AMM=AMM+DFDM*DFDM*WE
      AAM=AAM+DFDA*DFDM*WE
      SUM2=SUM2+TERM*DFDAA*WE
      SUM4=SUM4+TERM*DFDMM*WE
      SUMY=SUMY+SIGCAL(I)*WE
      SUMYY=SUMYY+SIGCAL(I)*SIGCAL(I)*WE
      SMTRM=SMTRM+TERM*WE
 1001 SUM=SUM+TERM*TERM*WE*WE
      SIGMA=SQRT((SUM-SMTRM*SMTRM/NCHAN)/(NCHAN-1))/SUMY
      DENOM=AAA*AMM-AAM*AAM
C
C     ADJUST PARAMETERS AS NECESSARY
C
      DALPHA=(GA*AMM-GM*AAM)/DENOM
      DMACH=(GM*AAA-GA*AAM)/DENOM
      IF(ABS(DMACH) .GT. 2.0) DMACH=SIGN(2.0,DMACH)
      WALPHA(JCYC)=ALPHA
      WMACH(JCYC)=MACH
      ALPHA=ALPHA+DALPHA
      MACH=MACH+DMACH
      CALL VELO(MACH,ALPHA,SIGCAL)
      CALL FIT(SIGCAL,EXPT)
C
C     STOP FITTING IF PARAMETERS OPTIMIZED
C
      IF((ABS(DMACH) .LE. 0.02) .AND. (ABS(DALPHA) .LE. (0.01*ALPHA)))
     1 GO TO 1002
 1000 CONTINUE
C
C     CALCULATE THE DECONVOLUTED TOF DISTRIBUTION
C
1002  R=SQRT(1.+(GAM-1.0)/2.*MACH*MACH)
      S=MACH*SQRT(GAM/2.)/R
      DT=ALPHA*CHAN*1.0E-06
      DO 1009 I=BCHAN,ECHAN
      T=(I-0.5)*DT
      V=LMIO/T
      SIGDEC(I)=V**3/T*EXP(-R*R*(V-S)**2)
1009  CONTINUE
      CALL BIG(SIGDEC,MAX3)
      CALL BIG(SIGCAL,MAX1)
      SCALE=SIGCAL(MAX1)/SIGDEC(MAX3)
      DO 1010 I=BCHAN,ECHAN
      SIGDEC(I)=SIGDEC(I)*SCALE
 1010 CONTINUE
C
C     DETERMINE THE PEAK VELOCITY
C
      PPK=0.
      CHP=MAX3-2.5
```

```
      DO 1200 I=1,40
      V=LMID/((CHP+.1*I)*DT)
      P=V**3/T*EXP(-R*R*(V-S)**2)
      IF(P .LT. PPK) GO TO 1200
      PPK=P
      ICPK=I
 1200 CONTINUE
      CPK=(CHP+.1*ICPK)
      VPK=LMID/(CPK*DT)*ALPHA
      TEMP=(ALPHA/12848.5)**2*MASS
      WRITE(6,205)
C
C     OUTPUT DATA
C
      DO 1005 I=BCHAN,ECHAN
 1005 WRITE(6,206) I,EXPT(I),SIGCAL(I),SIGDEC(I)
  205 FORMAT(1H0,6X,*CHANNEL*,4X,*OBSERVED*,6X,*CALCULATED*,4X,*DECONVOLUTED*)
     1UTED*)
  206 FORMAT(5X,I6,3(5X,F10.2))
      WRITE(6,207)
      WRITE(6,208) (WMACH(I), I=1,JCYC-1)
      WRITE(6,219) (WALPHA(I),I=1,JCYC-1)
      WRITE(6,213) JCYC,MACH
  213 FORMAT(1H0,I4,* ITERATIONS WERE NEEDED, THE FINAL MACH NUMBER =*,F
     15.2)
      WRITE(6,217) TEMP, ALPHA
  217 FORMAT(1H0,*   CORRECTED TEMPERATURE= *,F7.1,*  MOST PROBABLE VELO
     1CITY= *,F9.2)
      WRITE(6,216) SIGMA
  216 FORMAT(*0   STANDARD DEVIATION = *,E10.3)
      WRITE(6,209) VPK,CPK
  209 FORMAT(*0   PEAK VELOCITY = *,F9.2,* CM/SEC, AT CHANNEL *,F5.1)
  207 FORMAT(*0 INTERMEDIATE MACH NUMBERS/ / INTERMEDIATE ALPHAS*)
  208 FORMAT(1H ,10X,5(7X,F5.2))
  219 FORMAT(1H ,10X,5(3X,F9.2))
      GO TO 1003
      END
      SUBROUTINE VELO(MACH,ALPHA,SIGCAL)
C
C     CALCULATES THE TOF SPECTRA AVERAGED OVER IONIZER LENGTH AND SHUTTER
C     FUNCTION
C
      COMMON/PAR/CHAN,LMID,DL,R,S,GAM,BCHAN,ECHAN,NCHAN
      COMMON/WHEEL/SHUTTER,DETECT
      COMMON/WE/X(9),W(9)
      DIMENSION SIGCAL(255)
      REAL MASS,MACH,LMID,L
      INTEGER BCHAN,ECHAN
      R=SQRT(1.+(GAM-1.)/2.*MACH*MACH)
      S=MACH*SQRT(GAM/2.)/R
      DT=ALPHA*CHAN*1.0E-06
      IB=BCHAN-1
      IE=ECHAN-1
      RAD=DETECT/2.
      TOGO=SHUTTER+DETECT
      DO 2 I=IB,IE
      SUM20=0.0
      DO 3 M=1,9
      THYME=M*TOGO/10.
      THYMEP=TOGO-THYME
      WAIT=1.0
      IF(THYME .LT. DETECT) WAIT=(ACOS((RAD-THYME)/RAD)+(THYME-RAD)/RAD*
```

```
     1SIN(ACOS((RAD-THYME)/RAD)))/3.14159
      IF(THYMEP .LT. DETECT) WAIT=(ACOS((RAD-THYMEP)/RAD)+(THYMEP-RAD)/R
     1AD*SIN(ACOS((RAD-THYMEP)/RAD)))/3.14159
      DO 3 J=1,9
      T=DT*(I+THYME-TOGO/2. + J/10.)
      SUM10=0.0
      DO 4 K=1,9
      L=LMID+DL*X(K)/2.
      V=L/T
      P=V**3/T*EXP(-R*R*(V-S)**2)
    4 SUM10=SUM10+P*W(K)/2.
    3 SUM20=SUM20+SUM10*WAIT
      SIGCAL(I+1)=SUM20
    2 CONTINUE
      RETURN
      END
      SUBROUTINE FIT(SIGCAL,EXPT)
C
C     SCALES THE CALCULATED AND OBSERVED TOF SPECTRA
C
      COMMON/PAR/CHAN,LMID,DL,R,S,GAM,BCHAN,ECHAN,NCHAN
      INTEGER BCHAN,ECHAN
      DIMENSION SIGCAL(255),EXPT(255)
      CALL BIG(SIGCAL,NMAX1)
      CALL BIG(EXPT,NMAX2)
      SCALE=EXPT(NMAX2)/SIGCAL(NMAX1)
      DO 40 I=BCHAN,ECHAN
      SIGCAL(I)=SIGCAL(I)*SCALE
   40 CONTINUE
      RETURN
      END
      SUBROUTINE BIG(SIGCAL,MAX)
C
C     FINDS THE MAXIMUM IN A TOF SPECTRUM
C
      COMMON/PAR/CHAN,LMID,DL,R,S,GAM,BCHAN,ECHAN,NCHAN
      INTEGER BCHAN,ECHAN
      DIMENSION SIGCAL(255)
      MAX=0
      SIGMAX=0.0
      DO 1 I=BCHAN,ECHAN
      IF (SIGCAL(I) .LT. SIGMAX) GO TO 1
      SIGMAX=SIGCAL(I)
      MAX=I
    1 CONTINUE
      IF(MAX .EQ. 0) WRITE (6,255)
  255 FORMAT(*0  NO MAXIMUM FOUND*)
      RETURN
      END
      SUBROUTINE GAUSS
      COMMON/WE/X(9),W(9)
      X(5)=0.0
      X(6)=.32425
      X(7)=.61337
      X(8)=.83603
      X(9)=.96816
      W(5)=.33024
      W(6)=.31235
      W(7)=.26061
      W(8)=.18065
      W(9)=.08126
      DO 1 I=1,4
```

```
      J=10-I
      X(I)=-X(J)
      W(I)=W(J)
    1 CONTINUE
      RETURN
      END
      SUBROUTINE ZERO(EXPT,EXPTI,EXPTN)
      DIMENSION EXPT(255),EXPTI(255),EXPTN(255)
      DO 1 I=1,255
      EXPT(I)=0.0
      EXPTI(I)=0.0
    1 EXPTN(I)=0.0
      RETURN
      END
```

77-05 BROMINE MOLECULE TOF

MASS =160.000; TEMP = 350.0; GAMMA =1.40
CHANNEL WIDTH =10.0 MICROSECONDS; BEGINNING CHANNEL = 40, ENDING CHANNEL = 58; FLIGHT LENGTH =17.30 CM; IONIZER LENGTH = 2.50 CM,
ION ENERGY= 75.0 EV; ION PATH LENGTH= 24.0 CM, ION FLIGHT TIME OFFSET= 2.5 CHANNEL(S), ZERO CHANNEL OFFSET = 3.9 CHANNEL(S)
WHEEL FREQ. =400. HZ; WHEEL DIAMETER =17.8 CM; SLOT WIDTH = 3.00 MM; DETECTOR APERTURE =3.00 MM
TRIAL MACH NUMBER = 6.0

CHANNEL	RAW DATA	NORMALIZED	SMOOTHED
41	596.00	596.00	596.00
42	882.00	882.00	882.00
43	1253.00	1253.00	1253.00
44	1704.00	1704.00	1704.00
45	2087.00	2087.00	2087.00
46	2499.00	2499.00	2499.00
47	2722.00	2722.00	2722.00
48	2913.00	2913.00	2913.00
49	2884.00	2884.00	2884.00
50	2916.00	2916.00	2916.00
51	2556.00	2556.00	2556.00
52	2253.00	2253.00	2253.00
53	2005.00	2005.00	2005.00
54	1659.00	1659.00	1659.00
55	1380.00	1380.00	1380.00
56	1148.00	1148.00	1148.00
57	909.00	909.00	909.00
58	682.00	682.00	682.00
59	534.00	534.00	534.00

CHANNEL	OBSERVED	CALCULATED	DECONVOLUTED
41	596.00	550.31	300.34
42	882.00	873.76	570.61
43	1253.00	1267.96	953.27
44	1704.00	1699.46	1422.08
45	2087.00	2122.59	1920.01
46	2499.00	2488.99	2373.90
47	2722.00	2757.66	2715.70
48	2913.00	2902.55	2900.69
49	2884.00	2916.00	2916.00
50	2916.00	2807.86	2778.44
51	2556.00	2601.16	2524.92
52	2253.00	2326.17	2200.49
53	2005.00	2014.47	1848.17
54	1659.00	1694.26	1502.44
55	1380.00	1367.61	1186.76
56	1148.00	1109.45	913.97
57	909.00	867.99	688.39
58	682.00	665.92	508.46
59	534.00	501.99	369.20

INTERMEDIATE MACH NUMBERS/ / INTERMEDIATE ALPHAS

6.00	8.00	9.28	9.12	9.27
9.18				
18368.07	.9624.36	18955.30	19227.49	19139.34
19170.21				

7 ITERATIONS WERE NEEDED, THE FINAL MACH NUMBER = 9.19

CORRECTED TEMPERATURE= 355.9 MOST PROBABLE VELOCITY= 19163.27

STANDARD DEVIATION = .128E-02

PEAK VELOCITY = 35670.10 CM/SEC, AT CHANNEL 48.5

E. References

1. K. T. Gillen, A. M. Rulis, and R. B. Bernstein, J. Chem. Phys., 54, 2831 (1971).

2. P. E. Siska, Ph.D. Thesis, Harvard University, 1969.

3. P. E. Siska, J. Chem. Phys., 59, 6052 (1973).

4. P. E. Siska, private communication.

5. H. U. Hostettler and R. B. Bernstein, Rev. Sci. Instr., 31, 872 (1960).

6. E. A. Entemann, Ph.D. Thesis, Harvard University, 1967.

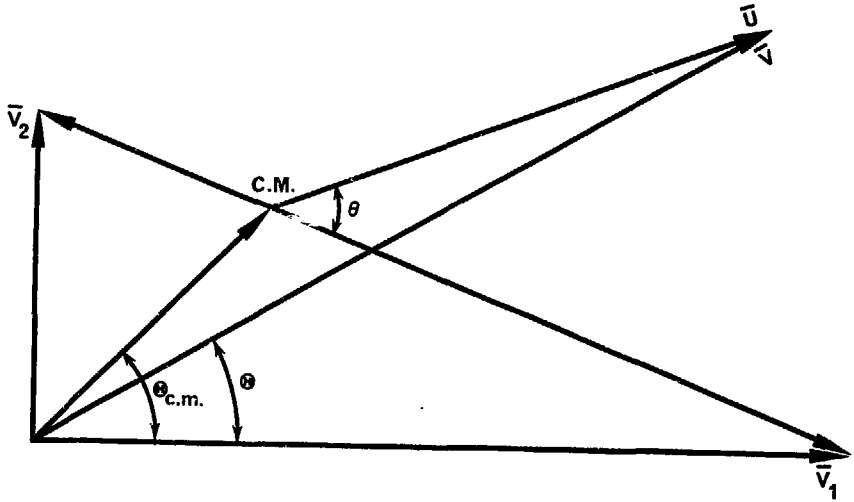

Figure 1. Newton diagram giving laboratory to center-of-mass coordinate transformation.